DISS. ETH NO. 17684

Coherent and Incoherent Light Scattering in the Resonance Fluorescence of a Single Molecule

A dissertation submitted to

ETH ZURICH

for the degree of

Doctor of Sciences

presented by

GERT WRIGGE

Dipl. Phys.
Albert Ludwigs Universität, Freiburg

born 24th May 1974

citizen of Germany

accepted on the recommendation of

Prof. Vahid Sandoghdar, examiner
Prof. Atac Imamoglu, co-examiner

2008

Contents

Summary

In this dissertation the interaction of a single dye molecule in a solid matrix with a freely propagating laser beam is studied. The combination of cryogenic single molecule spectroscopy and strongly focusing with solid immersion optics leads to a system in which a single molecule can extinguish an ongoing laser beam by more than 10 %.

DBATT (dibenzanthanthrene) molecules in alcane matrices have been shown to behave as quantum mechanical two-level systems at liquid helium temperatures. Furthermore, they can easily be introduced in various optical system geometries. In this work a high refractive index hemisphere was used to focus the excitation light to less than 400 nm diameter at the sample interface. Such a setup enables the systematic study of a single solid state quantum system with strongly focused light.

A detailed experimental analysis of the resonance fluorescence of a single DBATT molecule is presented. The interference between the excitation light and coherently scattered radiation can be influenced by changing amplitude and phase of the involved fields using polarization optics. This method enables an absolute measurement of the coherent scattering from a two-level system and its dependence on the excitation light power. Furthermore, the splitting of the incoherent resonance fluorescence spectrum into the so-called Mollow triplet could be observed at strong driving fields. The agreement of both measurements with theory is excellent.

In addition, due to its interferometric origin, extinction provides a detection method that surpasses fluorescence excitation concerning signal-to-noise ratio, particularly in the limit of weak emitters or low excitation. This is demonstrated by single molecule spectroscopy with ultralow illumination of just 600 aW. A careful comparison between the two detection methods is given.

f

Zusammenfassung

In dieser Arbeit wird die Wechselwirkung zwischen einem einzelnen Farbstoffmolekül und einem frei propagierenden Laserstrahl untersucht. Die Kombination von kryogener Einzelmolekülspektroskopie und starker Fokussierung mit Hilfe von Solid Immersion Technologie ermöglicht es, dass ein einzelnes Molekül einen freien Laserstrahl um mehr als 10 % abschwächen kann.

DBATT (Dibenzanthanthren) Moleküle können sich bei kryogenen Temperaturen wie nahezu ideale quantenmechanische Zweiniveau-Systeme verhalten. Ausserdem sind sie relativ einfach in verschiedene optische Geometrien implementierbar. In dieser Arbeit wurde mit Hilfe einer hochbrechenden hemisphärischen Solid Immersion Linse ein Anregungsfokus von unter 400 nm in der Probe erreicht. Dieser Aufbau eignet sich für eine systematische Untersuchung der Extinktion eines stark fokussierten Lichtfeldes durch ein einzelnes Festkörper Quantensystems.

In der Arbeit wird eine detailierte Untersuchung der Resonanzfluoreszenz eines einzelnen DBATT Moleküls präsentiert. Die Interferenz zwischen Anregungslicht und elastisch gestreuter Strahlung kann durch Manipulation der Amplitude und Phase der beteiligten Lichtfelder beeinflusst werden. Diese Methode erlaubt eine absolute Bestimmung der elastischen Streurate eines Zweiniveau-Systems und ihre Abhängigkeit von der Anregungsleistung. Zudem konnte die Aufspaltung des Spektrums der inelastischen Resonanzfluoreszenz in das sogenannte Mollow-Triplett bei starker Anregung beobachtet werden. Beide Messungen zeigen exzellente Übereinstimmung mit theoretischen Ergebnissen.

Aufgrund ihres interferometrischen Ursprungs bietet Extinktion eine Detektionsmethode, die übliche Fluoreszenzanregung in punkto Signal zu Rausch Verhältnis überbieten kann, insbesondere wenn mit schwachen Emittern oder im Limit der schwachen Anregung arbeitet. Dies wird anhand eines Versuches verdeutlicht, bei dem Einzelmolekülspektroskopie mit nur 600 aW Anregungsleistung möglich ist. Hierbei wird ein genauer Vergleich der beiden Detektionsmethoden gegeben.

Introduction

Absorption spectroscopy and its description by the Beer-Lambert law is a well established technique in the laboratory. However, the extension of this idea towards detecting light extinction by single quantum systems had been a challenge at the limit of technological feasibility. In 1987, Wineland, Itano and Bergquist succeeded in detecting a single trapped Mercury ion in a transmission measurement with the help of trapping potential modulation [1]. In fact, the field of single molecule spectroscopy launched in 1989 with the first optical detection of a fluorescent dye in an extinction experiment. Here, Moerner and Kador employed a combination of two modulation techniques to discriminate the weak signal of a single pentacene molecule from a large laser noise background [2].

After 1990, when Orrit and Bernard adapted the technique of fluorescence excitation spectroscopy to single molecule detection [3], extinction measurements on single molecules had not been pursued much [4]. In fluorescence excitation, the laser light is blocked from the detector with the help of high quality optical long-pass filters, and only the Stokes shifted fluorescence of the molecule is detected. Due to its superior signal to noise ratio, fluorescence excitation quickly became a standard method to detect single molecules, both at cryogenic and later at room temperature [5, 6]. Today many fields profit from the spectral selectivity and spatial resolution offered by single molecule fluorescence detection. One example is the study of biological dynamics [7] and structures [8]. Furthermore, fluorescence excitation enabled many fundamental experiments in the field of quantum optics, which had been dominated by the study of atomic beams or isolated ions, to be carried out in the solid state [9, 10].

However, fluorescence excitation sacrifices information about the coherent interaction of light with a molecule, since it blocks the molecule's resonance fluorescence. There has been a considerable interest in having access to resonant processes, which is fueled particularly by proposals for controlled interaction between a single photons and single emitters [11, 12, 13]. If the aim is to achieve this in the solid state and without the use of high-finesse cavities, extinction measurements come into play again, and highly efficient interaction between light and the emitter is needed. Quantum dot spectroscopy relies on extinction to get direct access to the excitonic transitions [14, 15] and for optical readout of spin states [16], which initiated experimental progress towards efficient interaction in this field [17, 18].

In this thesis I will present a new experimental method to realize efficient coupling of radiation to a single dye molecule under cryogenic conditions and in a single-pass configuration. By focusing the excitation light to an area comparable to the molecule's extinction cross section, we were able to directly detect a single dye molecule in transmission with around 10 % interaction efficiency, a very high signal-to-noise ratio, and to study its resonance fluorescence over 9 order of magnitude of excitation intensity.

Chapter 1 introduces the basics and terminology of cryogenic single molecule spectroscopy. Furthermore, essential theoretical results in light-matter interaction and resonance fluorescence will be summarized.

Chapter 2 gives an overview of extinction spectroscopy of a single two-level system, with and without loss channels. This will lay the foundation to interpret and analyze the experimental results.

In chapter 3 I will explain the experimental setup which combines high resolution solid immersion microscopy with cryogenic single molecule spectroscopy. In addition, the used laser source, detectors and sample are characterized.

The experimental results are summarized in chapters 4-7. First, the performance of the solid immersion lens setup is tested, and the efficiency of interaction, as well as methods for characterization and manipulation of the extinction signal are introduced. In chapter 5 I compare single molecule detection via extinction to conventional fluorescence excitation, with a focus on ultrasensitive detection in the low excitation limit. I will show that under certain conditions extinction detection provides the better signal-to-noise ratio. An extensive study of the resonance fluorescence from a single molecule is summarized in chapter 6. We observed both the coherent and incoherent emission, and studied its dependence on excitation intensity. We were able to extract the absolute number of coherently scattered photons from the total detector signal, and observe the Mollow fluorescence triplet in the incoherent emission. Lastly, chapter 7 introduces an experiment where near-field excitation of a single molecule lead to strong extinction signals. In fact, this experiment was performed prior to the far-field measurements discussed in this thesis but is included to provide a more complete overview of our efforts in achieving an efficient coupling between light and matter.

1 Theoretical Background

1.1 Photophysics of impurity molecules in solids

A good review of spectroscopic features, photochemical processes and the terms used in this chapter is given in [19]. A typical fluorescent dye molecule exhibits a level structure with optical transitions in the visible range of the spectrum as shown in Fig. 1.1. The host matrix also has optically accessible transitions, however, these are usually chosen to lie in the UV spectrum. Furthermore, due to the small distance between matrix molecules, the states are bundled in band structures.

In contrast, the states of the sparsely distributed impurity molecules are isolated and localized. In the ground state all electrons are paired, the total spin is zero and the system correnspondingly is in a singlet state, labeled as $|S_0\rangle$ in Fig. 1.1. The system can undergo optical transitions into higher electronic states, which have to remain singlets due to spin selection rules. Shown is just the first excited state $|S_1\rangle$. For typical dye molecules the spacing between the first two electronic states lies in the visible spectrum, i.e. roughly 2 eV.

1.1.1 Vibronic transitions

A dye molecule has a complex internal structure and is inserted into the lattice of a host crystal. As a result, the vibrational degrees of freedom of both the dye molecule or the host matrix lead to a manifold of additional levels, with an energy spacing from the purely electronic states that are characteristic for the dye/matrix system. Optical transitions can lead to population of these states, resulting in a complex structure of the absorption and emission spectrum.

Zero phonon line and Phonon wing

A prominent feature in the absorption and emission spectrum of impurity dye molecules is the so-called zero phonon line (ZPL). This is a rearrangement-free optical transition that does not involve any vibrations and therefore has a well defined energy, with a narrow, sometimes lifetime limited line. However, the host crystal can support a quasi-continuum of lattice phonons which have energies in the range of 10-100 cm^{-1} [19]. Due to electron-phonon coupling, optical transitions are often accompanied with the generation or destruction of phonons in the matrix, and such transitions lead to the appearance of a broad phonon wing (PW) in the spectrum [20]. Figure 1.2 shows an example of ZPL and PW.

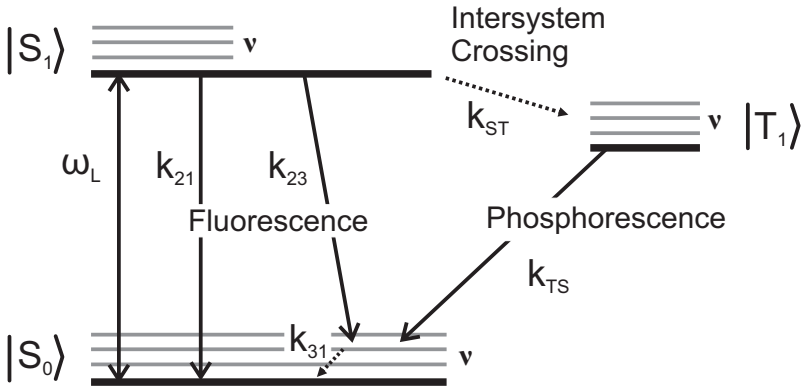

Figure 1.1: Simplified levelscheme of a typical dye molecule.

The ratio of the power emitted into the ZPL to the total emission into ZPL and corresponding PW is called Debye-Waller factor α_{DW}. For typical dye molecules in organic host crystals this factor is $\alpha_{\mathrm{DW}} \approx 0.1$ [21], but can reach values of up to 0.7 in weakly interacting host/matrix systems [22]. Matrix phonons are not thermally excited at superfluid Helium temperatures. However, at $T \gtrsim 2$ K, phonon modes become populated and are the main cause of dephasing in single molecule spectra [23, 24]. The Debye-Waller factor is consequently temperature dependent, and will decrease for higher temperatures.

Intramolecular vibrations

The intramolecular vibrations of a dye molecule, such as streching, bending and torsional modes, have energies that depend on the internal structure of the compound. Rigid polyaromatic hydrocarbon (PAH) molecules have vibrational energies that lie in the range of a few hundred to thousands of wavenumbers [21]. DBATT, the PAH used throughout this work, has its lowest vibrational state at an energy of roughly 250 cm^{-1} [25]. This value does not change appreciably in different host systems [26]. In Fig. 1.1 the vibrational levels of each electronic state are indicated with a parameter ν. Optical transitions from $|S_1\rangle$ with $\nu = 0$ that leave the molecule in one of the vibrational states of $|S_0\rangle$ result in several replicas of the purely electronic ZPL and associated PW in the lower energy side of an emission spectrum, called Stokes shifted fluorescence. Optical transitions are often designated with $\nu_{\mathrm{i}} - \nu_{\mathrm{f}}$, the vibrational levels of initial and final state. The purely electronic ZPL will therefore be addressed as 0-0 ZPL which distinguishes it from its vibrational replicas. 0-1 excitation on the other hand is a common designation for a transition from the electronic and vibrational ground state to the first vibrational state of $|S_1\rangle$.

Figure 1.2 shows the vibrational progression in an theoretical emission spectrum, including PWs. The vibronic transitions appear broader than the 0-0 ZPL due to the short lifetimes of the final states [27].

The probability per unit time of any transition between an initial state $|i\rangle$ and a

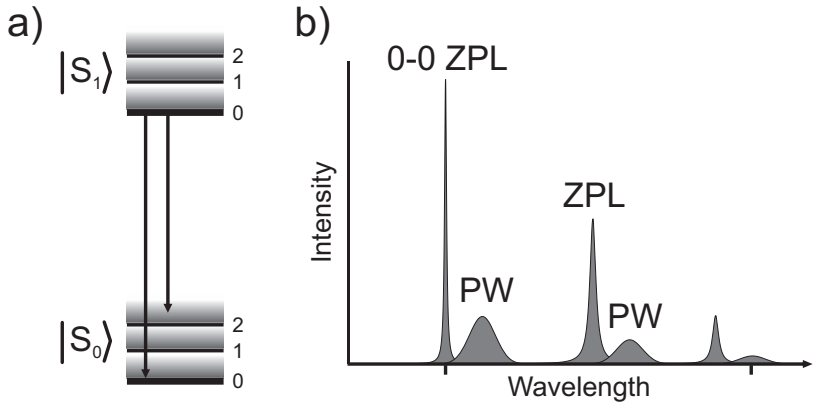

Figure 1.2: Optical transitions and fluorescence spectrum of a single molecule coupled to different vibrational degrees of freedom. Each zero phonon line (ZPL) is a transition from the vibrational ground state of $|S_1\rangle$ to a vibrational state of $|S_0\rangle$. The phonon wing (PW) is a broad feature that accompanies each ZPL due to the additional generation of matrix phonons. Not shown are pseudolocal modes that result in additional sharper features within each PW. The two transitions shown in a) correspond the two marked positions in the spectrum b).

final state $|f\rangle$ in the weak excitation limit is given by Fermi's golden rule as

$$P_{\mathrm{fi}} = \frac{2\pi}{\hbar} \left| \left\langle f \left| \hat{H}_{\mathrm{rad}} \right| i \right\rangle \right|^2 \rho(E) \ , \tag{1.1}$$

where $\rho(E)$ is the density of final states. This equation determines the relative strength of the ZPLs in a spectrum as shown in Fig. 1.2[1]. In single-molecule spectroscopy, one defines the Franck-Condon factor as the integrated strength of all vibronic lines (ZPLs from $|S_1\rangle$ to vibrational states of $|S_0\rangle$ with $\nu \neq 0$) compared to the strength of the 0-0 ZPL. The Franck-Condon factor for terrylene, a PAH often used in single molecule spectroscopy, is estimated to be $\alpha_{\mathrm{FC}} \approx 0.4$ [28].

In summary, the rich vibronic features in molecular spectra are caused by the internal structure of the dye molecule, as well as its integration in a solid matrix, and the resulting manifold of vibrational modes. The strength of the 0-0 ZPL is reduced by the product $\alpha = \alpha_{\mathrm{DW}}\alpha_{\mathrm{FC}}$ of Debye-Waller and Franck-Condon factors. Values for α_{DW} and α_{FC} are roughly 0.1 and 0.4, respectively [22], but have only been thoroughly determined in a few single molecule systems. For the experiments presented in this dissertation, it is important to work with a system that shows a strong 0-0 ZPL, because this strength determines the interaction efficiency of the molecule with a resonant laser beam as shown in chapter 2.4.

[1]The Franck-Condon principle assumes that an electronic transition happens much faster than the nuclear coordinates of the molecule can change, and the normalized wavefunction overlap integral squared in Eq. (1.1) is called the Franck-Condon factor α_{FC}.

1.1.2 Excitation spectroscopy

The most common way to study single molecules in a solid matrix is fluorescence excitation spectroscopy, introduced by Orrit and Bernard in 1990 [3]. The sample is placed in the focus of a frequency tunable narrowband laser. Behind an optical long-pass filter which rejects the excitation wavelength, the broadband Stokes shifted fluorescence of the molecule is recorded, usually as an integrated signal on a wavelength-insensitive detector. The most common techniques are 0-0 excitation (if the purely electronic 0-0 ZPL is resonantly driven), or 0-1 excitation (if the molecule is excited from $|S_0\rangle$ to the first vibrational level of $|S_1\rangle$). In a 0-0 excitation spectrum, the integrated Stokes shifted fluorescence intensity is plotted versus the laser frequency, and the resulting Lorentzian curve has a full width at half maximum (FWHM) which is called the homogeneous linewidth of the 0-0 transition. In suitable molecule-matrix systems and at low temperatures, where dephasing processes are minimized, this can become equal to the natural linewidth, which is given by the molecule's excited state lifetime. Lastly, the inhomogeneous linewidth is the FWHM of the sum of excitation spectra of an ensemble of molecules in one sample. It reflects the energy distributions of 0-0 ZPLs in the matrix, caused by different nanoenvironments of nominally identical dye molecules.

1.1.3 Triplet state

From the excited state $|S_1\rangle$ the molecule can undergo a singlet-triplet intersystem crossing (ISC), a transition into the first triplet state. This spin-forbidden process can occur with a comparably low probability by perturbations due to spin-orbit coupling. The triplet state is "dark", that means optically accessible transitions at the wavelength of the driving field are weak [29, 30]. The return to the singlet state $|S_0\rangle$ is a reverse intersystem crossing and the lifetime of the triplet state can be relatively long. Most dye molecules do not show phosphorescence when returning to the singlet state [31]. The transition of a fluorescent dye molecule into the dark triplet state and its recovery back into the fluorescent singlet states leads to an on/off behavior of the fluorescence upon resonant excitation, called blinking. The duration of the on times is governed by the rate k_{ST} from $|S_1\rangle$ to $|T_1\rangle$ and the population of the excited state $|S_1\rangle$, the duration of the off-times only by the rate k_{TS} out of the triplet. These rates can be determined from the evaluation of a fluorescence time trace [32] or by an analysis of the photon statistics of the fluorescence photon stream. The on and off periods at characteristic times leads to a bunching of photons, visible in intensity autocorrelation measurements at time scales of k_{ST}^{-1} [33].

1.1.4 DBATT in *n*-alkanes

Linear alkanes, labeled with a prefix n for normal, have been widely used as host matrices for molecular spectroscopy. In 1952 Shpol'skii found that the ensemble absorption lines of certain dye molecules in these hosts becomes extraordinarily narrow if the sample is shock frozen to liquid helium temperature. A short review of the history of the so-called Shpol'skii effect is given in [34]. This reduction of the inhomogeneous distribution is likely a result of a very weak electron-phonon

interaction between the guest molecule and host matrix. Richards and Rice [35] accordingly speak of a "dilute cold gas" of guest molecules in these systems.

Ensemble absorption spectra split in several multiplets which has been shown to be connected to molecules built into the matrix at different orientations. This was studied by polarization measurements in both shock-frozen samples and single crystals [34, 36, 37]. Bloess et al. [34] find that molecules of DBATT are built into a *n*-tetradecane matrix in two main orientations, separated by 110°. These orientations are conserved over a large length scales, which was verified with 23nm resolution for small areas (via CCD assisted localization of single molecules), up to 2mm length scale with less resolution. One explanation is that the structures seen on the sample (cracks and bright/dark regions) only form at low temperatures as mechanical stress in the film is relieved [24], and are not related to the existence of uncorrelated microcrystals that would be expected to form under shock-freezing.

The polycyclic aromatic hydrocarbon DBATT has been first studied by Boiron et al. in the matrix *n*-hexadecane in 1996 [25, 38]. Most of the findings can be adapted without much change to the matrix *n*-tetradecane as shown in e.g. [26] and characterizations in chapter 3. The lifetime was found to be 9.4±0.5 ns both at room temperature and at 77 K. Bulk absorption and emission spectra reveal a first strong vibronic band at 245 cm^{-1} from the zero phonon line. The relatively weak PW of the 0-0 ZPL exhibits a pronounced mode at 15 cm^{-1}, attributed to the libration of DBATT in the hexadecane matrix [38]. Triplet population and depopulation rates have been determined via photon bunching experiments. A biexponential behavior of the bunching curve at around 1ms is attributed to different rates into the x/y and the z-sublevel of the triplet state. The intersystem crossing rate k_{ST} is 1250 s^{-1} into the x/y- and 40 s^{-1} into the z-sublevel, and the rates k_{TS} back into the ground state $|S_0\rangle$ are 4500 s^{-1} and 750 s^{-1}, respectively. These values indicate that the triplet is depopulated faster than it is populated, avoiding the so-called triplet bottleneck. The triplet population reaches 13 % at the maximum, which makes DBATT a favorable choice for quantum optical experiments [10, 25, 39].

1.2 Light matter interaction

To introduce resonance fluorescence and its spectral properties, I will give a short overview of the semiclassical theory of light-matter interaction for a two-level system (TLS) with a ground state $|g\rangle$ and an excited state $|e\rangle$. A single molecule displays many more states and correspondingly more optical transitions and nonradiative intersystem crossing events. However, as these transitions are out of resonance, they can easily be introduced later in the set of equations derived here.

1.2.1 Two-level system field interaction

Density matrix

A TLS consists of two states $|g\rangle$ and $|e\rangle$ which are eigenstates of the unperturbed Hamiltonian. Therefore, the system can be described in these states as a basis, and

at any time it will be in a coherent superposition

$$|\psi\rangle = c_{\mathrm{g}}(t)\,|g\rangle + c_{\mathrm{e}}(t)\,|e\rangle \ , \quad |g\rangle = \begin{pmatrix} 1 \\ 0 \end{pmatrix} \ , \quad |e\rangle = \begin{pmatrix} 0 \\ 1 \end{pmatrix} \ , \quad |c_g|^2 + |c_e|^2 = 1 \ .$$

In practice, one does not need to know the exact state of the system at any time, and just studies the average outcome of many experiments. The density matrix formalism describes the knowledge one has about the average state of the system as coherent as well as incoherent superpositions of the basis states. For the TLS one writes

$$\hat{\rho} = \rho_{\mathrm{gg}}\,|g\rangle\langle g| + \rho_{\mathrm{ee}}\,|e\rangle\langle e| + \rho_{\mathrm{ge}}\,|g\rangle\langle e| + \rho_{\mathrm{eg}}\,|e\rangle\langle g| = \begin{pmatrix} \rho_{\mathrm{gg}} & \rho_{\mathrm{ge}} \\ \rho_{\mathrm{eg}} & \rho_{\mathrm{ee}} \end{pmatrix} \ ,$$

with

$$\rho_{\mathrm{gg}} = c_{\mathrm{g}}^* c_{\mathrm{g}} \ , \quad \rho_{\mathrm{ee}} = c_{\mathrm{e}}^* c_{\mathrm{e}} \ , \quad \rho_{\mathrm{ge}} = c_{\mathrm{g}}^* c_{\mathrm{e}} \ , \quad \rho_{\mathrm{eg}} = \rho_{\mathrm{ge}}^* \ , \quad \rho_{\mathrm{gg}} + \rho_{\mathrm{ee}} = 1 \ .$$

The diagonal matrix elements are called populations, the off-diagonal elements coherences. The expectation value of an operator $\hat{A}$ acting on the system can be written as the trace of the matrix product of operator and the density matrix

$$\left\langle \hat{A} \right\rangle = \mathrm{Tr}\left[\hat{\mathrm{A}}\hat{\rho}\right] \ . \tag{1.2}$$

Hamiltonian

Assume a TLS at the coordinate origin interacting with a classical monochromatic laser field $\mathbf{E}(\mathbf{r}, t)$ with angular frequency ω_{L} close to the resonance frequency ω_0 of the system. The total Hamiltonian can be written as

$$\hat{H} = \hat{H}_{\mathrm{A}} - \hat{\mathbf{d}} \cdot \mathbf{E}(\mathbf{r}_0, t) \ , \tag{1.3}$$

where $\hat{H}_{\mathrm{A}}$ is the Hamiltonian of the unperturbed system. The energy axis is offset such that $\hat{H}_{\mathrm{A}}\,|g\rangle = 0$ and $\hat{H}_{\mathrm{A}}\,|e\rangle = \hbar\omega_0\,|e\rangle$. The interaction Hamiltonian $-\hat{\mathbf{d}}\cdot\mathbf{E}(\mathbf{r}_0, t)$ contains just the dipole operator $\hat{\mathbf{d}} = -e\hat{\mathbf{r}}$ since only electric dipole transitions are studied. In the dipole approximation, the electric field is evaluated at the position $\mathbf{r}_0$ of the TLS.

We can write the Hamiltonian as a 2x2 matrix in the basis $|g\rangle$ and $|e\rangle$. The part $\hat{H}_{\mathrm{A}}$ will only contribute diagonal elements, since $|g\rangle$ and $|e\rangle$ are eigenstates. The interaction Hamiltonian will only contribute off-diagonal elements for inversion symmetric systems, because the dipole operator has odd parity, and matrix elements like $\langle g|\,\hat{d}\,|g\rangle$ vanish. Introducing $\hat{\sigma} = |g\rangle\langle e|$ as the atomic lowering operator and rewriting the laser field in negative and positive frequency parts the Hamiltonian becomes

$$\begin{aligned} E &= E^{(-)} + E^{(+)} = \frac{E_0}{2}(e^{i\omega_{\mathrm{L}}t} + e^{-i\omega_{\mathrm{L}}t}) \\ \hat{d} &= d_{\mathrm{ge}}(\hat{\sigma} + \hat{\sigma}^\dagger) \ , \quad d_{\mathrm{ge}} = \langle g|\,\hat{d}\,|e\rangle \\ \hat{H} &= \hbar\omega_0\hat{\sigma}^\dagger\hat{\sigma} + \frac{\hbar\Omega}{2}(\hat{\sigma}e^{i\omega_{\mathrm{L}}t} + \hat{\sigma}^\dagger e^{-i\omega_{\mathrm{L}}t} + \hat{\sigma}e^{-i\omega_{\mathrm{L}}t} + \hat{\sigma}^\dagger e^{i\omega_{\mathrm{L}}t}) \ . \end{aligned} \tag{1.4}$$

$\Omega = -\frac{d_{\mathrm{ge}} \cdot E_0}{\hbar}$ is the Rabi frequency which quantifies the interaction strength. Using Eq. (1.2), the expectation values of the atomic lowering and raising operators become

$$\langle \hat{\sigma} \rangle = \rho_{\mathrm{ge}} \ , \quad \left\langle \hat{\sigma}^\dagger \right\rangle = \rho_{\mathrm{eg}} \ , \quad \left\langle \hat{\sigma}^\dagger \hat{\sigma} \right\rangle = \rho_{\mathrm{ee}} \ . \tag{1.5}$$

To get rid of the explicit time dependence of the Hamiltonian, one changes into a coordinate system corotating with the frequency ω_{L} by substituting $\tilde{\sigma} = e^{-i\omega_{\mathrm{L}} t} \hat{\sigma}$. In this so-called laser frame the Hamiltonian reads

$$\tilde{H} = \hbar \Delta \hat{\sigma}^\dagger \hat{\sigma} + \frac{\hbar \Omega}{2} (\tilde{\sigma} + \tilde{\sigma}^\dagger + \tilde{\sigma} e^{-i2\omega_{\mathrm{L}} t} + \tilde{\sigma}^\dagger e^{i2\omega_{\mathrm{L}} t}) \ . \tag{1.6}$$

The rotating wave approximation (RWA) eliminates the last two terms of the above equation. One can neglect these terms because they oscillate at twice the optical frequency. The first two terms on the other hand are slowly varying with the detuning $\Delta \equiv \omega_{\mathrm{L}} - \omega_0$ due to an intrinsic time dependence of $e^{-i\omega_0 t}$ of the excited state $|e\rangle$ and hence the operator $\hat{\sigma}$.

Only the raising and lowering operators are affected by the coordinate transformation. The population operator $\hat{\sigma}^\dagger \hat{\sigma}$ remains the same, however, the energy of the excited state is shifted. In this frame the laser field is stationary, and the energy difference between the levels becomes Δ.

1.2.2 Optical Bloch equations

The Liouville equation for the density matrix $\hat{\rho}$ is given by

$$\dot{\hat{\rho}} = \frac{i}{\hbar} \left[\hat{\rho}, \hat{H} \right] \ .$$

Consequently, the equations of motion for the density matrix elements in the laser frame and RWA are

$$\begin{aligned}
\dot{\tilde{\rho}}_{\mathrm{ge}} &= -\frac{1}{2} i \Omega \left(\rho_{\mathrm{ee}} - \rho_{\mathrm{gg}} \right) - \left(i\Delta + \Gamma_2 \right) \tilde{\rho}_{\mathrm{ge}} \\
\dot{\rho}_{\mathrm{gg}} &= \frac{1}{2} i \Omega \left(\tilde{\rho}_{\mathrm{ge}} - \tilde{\rho}_{\mathrm{eg}} \right) + \Gamma_1 \rho_{\mathrm{ee}} \\
\dot{\rho}_{\mathrm{ee}} &= -\frac{1}{2} i \Omega \left(\tilde{\rho}_{\mathrm{ge}} - \tilde{\rho}_{\mathrm{eg}} \right) - \Gamma_1 \rho_{\mathrm{ee}} \ .
\end{aligned} \tag{1.7}$$

Spontaneous emission from the excited state is introduced phenomenologically with a longitudinal decay rate Γ_1, and damping of the coherence between $|\tilde{g}\rangle$ and $|\tilde{e}\rangle$, is attributed for by a transversal decay rate $\Gamma_2 = \frac{1}{2}\Gamma_1 + \Gamma_2^*$. The first contribution to Γ_2 is a direct consequence of the population decay, and in the ideal case this is the only component. Γ_2^* accounts for an additional decay of the coherence, often called collisional broadening [40], caused by processes that leave the populations unaffected but randomize the phase of the system's wavefunction. The interaction with matrix phonons [24] is the main cause of this dephasing in solid state systems. This notation originated with Bloch's treatment of nuclear magnetic resonance [41] and is common in optics [42].

Stationary states

For most purposes it is sufficient to derive the so-called stationary states for the density matrix elements, i.e. the solutions of Eq. (1.7) for the boundary condition that all time derivatives are zero. First, I introduce the the notation from [40, 42]

$$u = \frac{1}{2}(\tilde{\rho}_{ge} + \tilde{\rho}_{\mathrm{eg}}) \ , \quad v = \frac{1}{2i}(\tilde{\rho}_{\mathrm{ge}} - \tilde{\rho}_{\mathrm{eg}}) \ .$$

u and v can be reconstructed to be the components of $\left\langle \hat{d} \right\rangle$ which are in-phase and in-quadrature with the external electromagnetic field [42, 43]. The stationary states can be written in a condensed form with a Lorentzian denominator, if an effective linewidth Γ_{eff} is introduced

$$\begin{aligned} u^{\mathrm{ss}} &= \frac{\Omega\Delta}{2\left(\Delta^2 + \Gamma_{\mathrm{eff}}^2\right)} \\ v^{\mathrm{ss}} &= \frac{\Omega\Gamma_2}{2\left(\Delta^2 + \Gamma_{\mathrm{eff}}^2\right)} \\ \rho_{\mathrm{ee}}^{\mathrm{ss}} &= \frac{\Omega^2\Gamma_2}{2\Gamma_1\left(\Delta^2 + \Gamma_{\mathrm{eff}}^2\right)} \ , \end{aligned} \tag{1.8}$$

with

$$\Gamma_{\mathrm{eff}}^2 = \Gamma_2^2 + \Omega^2\frac{\Gamma_2}{\Gamma_1} \ . \tag{1.9}$$

1.3 Resonance fluorescence

Resonance fluorescence is the radiation emitted by a TLS upon near-resonant excitation at or close to the driving field's wavelength. The statistical and spectral properties of the emitted light is nontrivial, due to the nonlinear behavior of a TLS at higher excitation intensities. It displays both classical and quantum properties.

1.3.1 Saturation

The total power P_{sca} at which a TLS scatters photons (or equivalently, emits resonance fluorescence) can be calculated simply as the product of excited state population in the steady state, the longitudinal decay rate, and photon energy

$$P_{\mathrm{sca}} = \hbar\omega_0\Gamma_1\rho_{\mathrm{ee}}^{\mathrm{ss}} \ . \tag{1.10}$$

Considering Eq. (1.8) one can see that the scattered power is a Lorentzian function of detuning, with a full width at half-maximum (FWHM) of $2\Gamma_{\mathrm{eff}}$. There are several different regimes, depending on whether the Rabi frequency Ω, the longitudinal decay rate Γ_1 or the transversal decay rate Γ_2 dominates.

At low excitation intensity and in the absence of dephasing, $\Omega \ll \Gamma_1$ and $\Gamma_2 = \Gamma_1/2$, the homogeneous linewidth is given by Γ_1. The system is Fourier limited, and the linewidth is lifetime limited. For small intensity and a large dephasing, $\Gamma_2 > \Gamma_1$ and the FWHM is governed by dephasing. If the system is excited with high intensity light, $\Omega \gg \Gamma_1 = 2\Gamma_2$, the FWHM is given by $\sqrt{2}\Omega$.

The stationary excited state population at zero detuning can maximally reach 1/2, an effect which is called saturation and limits the emitted power to $\hbar\omega_0\Gamma_1/2$. The stationary solutions in Eq. (1.8) can be expressed in terms of a saturation parameter S, which is defined as [42]

$$\begin{aligned} S &= \frac{\Omega^2/(\Gamma_2\Gamma_1)}{1+\Delta^2/\Gamma_2^2} \\ u^{\rm ss} &= \frac{\Delta\Gamma_1/\Gamma_2}{2\Omega}\frac{S}{1+S}\ , \quad v^{\rm ss} = \frac{\Gamma_1}{2\Omega}\frac{S}{1+S}\ , \quad \rho_{\rm ee}^{\rm ss} = \frac{1}{2}\frac{S}{1+S}\ . \end{aligned} \tag{1.11}$$

1.3.2 Correlation functions

Correlation functions of the light emitted by a TLS give insight in the nature of resonance fluorescence. The normalized field- and intensity correlation functions (also called first and second order correlation functions) of the emitted field are defined as

$$\begin{aligned} g^{(1)}(\tau) &:= \frac{\left\langle E^{(-)}(t)E^{(+)}(t+\tau)\right\rangle}{\left\langle E^{(-)}(t)E^{(+)}(t)\right\rangle} \\ g^{(2)}(\tau) &:= \frac{\left\langle E^{(-)}(t)E^{(-)}(t+\tau)E^{(+)}(t+\tau)E^{(+)}(t)\right\rangle}{\left\langle E^{(-)}(t)E^{(+)}(t)\right\rangle^2}\ . \end{aligned} \tag{1.12}$$

Usually the fields at time t and a later time $t+\tau$ are evaluated at the position of the detector, and the retardation due to the "time of flight" between TLS and detector is neglected.

The field of a dipolar emitter can be written quantum mechanically in terms of the dipole operator via the source field expression [42]. The classical dipole field [44] is adapted, and the second time derivative of the dipole moment (classical) is exchanged with the dipole moment operator (quantum), which is allowed as long as the fluctuations of interest are at the frequency $\omega_{\rm L}$. The resulting field is

$$\mathbf{E}^{(+)}(\mathbf{r}) = \frac{-\omega_0^2 d_{\rm ge}}{4\pi\epsilon_0 c^2}\frac{[(\hat{\mathbf{r}}\cdot\hat{\epsilon})\hat{\mathbf{r}}-\hat{\epsilon}]}{|\mathbf{r}|}\hat{\sigma}\ , \tag{1.13}$$

where $\hat{\epsilon}$ is a unit vector along the orientation of the dipole moment, and $\hat{\mathbf{r}} = \mathbf{r}/|\mathbf{r}|$.

The correlation functions in Eq. (1.12) become

$$g^{(1)}(\tau) = \frac{\left\langle\hat{\sigma}^\dagger(t)\hat{\sigma}(t+\tau)\right\rangle}{\left\langle\hat{\sigma}^\dagger(t)\hat{\sigma}(t)\right\rangle}\ , \quad g^{(2)}(\tau) = \frac{\left\langle\hat{\sigma}^\dagger(t)\hat{\sigma}^\dagger(t+\tau)\hat{\sigma}(t+\tau)\hat{\sigma}(t)\right\rangle}{\left\langle\hat{\sigma}^\dagger(t)\hat{\sigma}(t)\right\rangle^2}\ . \tag{1.14}$$

An immediate result is that for a single quantum system the intensity correlation function $g^{(2)}(0) = 0$, because the product of two projection operators, $\hat{\sigma}\hat{\sigma}$ vanishes. This qualitatively means that after the detection of a photon from the system, the probability to detect a second photon is zero, a phenomenon called antibunching [45, 46, 47] and a purely nonclassical effect.

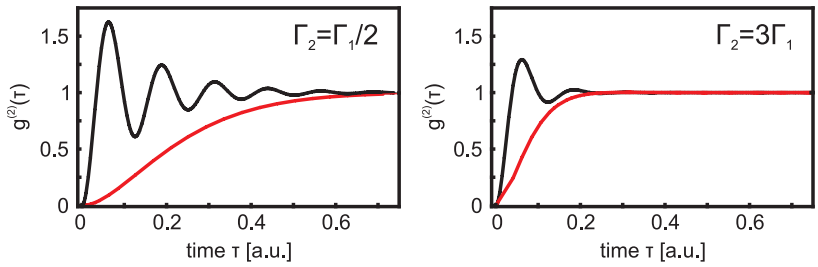

Figure 1.3: Second order correlation function $g^{(2)}(\tau)$ of TLS resonance fluorescence. The left side shows $g^{(2)}(\tau)$ in the limit of no dephasing, the right side for $\Gamma_2 = 3\Gamma_1$. The red curves are at low excitation $\Omega_\Gamma \ll \Gamma_1$, the black curves for strong excitation, $\Omega_\Gamma = 5\Gamma_1$.

The complete solution for $g^{(2)}(\tau)$ provided that a photon was detected at t=0 is given e.g. in [40] and in a compact version including longitudinal and transversal decay rates in [48]

$$\begin{aligned} g^{(2)}(\tau) &= 1 - \left(\cos(\Omega_\Gamma t) + \frac{\Gamma_1 + \Gamma_2}{2\Omega_\Gamma}\sin(\Omega_\Gamma t)\right) e^{-\frac{\Gamma_1+\Gamma_2}{2}t} \\ \Omega_\Gamma &= \sqrt{\Omega^2 - (\Gamma_1 - \Gamma_2)^2/4}\ , \end{aligned} \tag{1.15}$$

where Ω_Γ is the damped Rabi frequency. For $\Omega < \frac{1}{2}|\Gamma_1 - \Gamma_2|$, i.e. small excitation intensities, $g^{(2)}(\tau)$ shows an antibunching dip at τ=0. For large intensities the excited state population ρ_{22} oscillates and the emitted radiation shows Rabi oscillations in $g^{(2)}$. Figure 1.3 shows examples of $g^{(2)}$ functions for small and large driving fields, and in the limits of no or large dephasing.

1.3.3 Coherent and incoherent components

The dipole $\hat{\sigma}$ in Eq. (1.13) can be written as a sum of an average dipole and the instantaneous difference of $\hat{\sigma}$ from its average value [42][2]

$$\hat{\sigma} = \langle\hat{\sigma}\rangle + \delta\hat{\sigma}\ , \tag{1.16}$$

where $\delta\hat{\sigma} = \hat{\sigma} - \langle\hat{\sigma}\rangle$. The first term in Eq. (1.16) is the radiation from a classical dipole with a well defined phase with respect to the excitation field. The total emitted power in Eq. (1.10) then becomes the sum of two contributions

$$P_{\text{sca}} = \hbar\omega_0\Gamma_1\left\langle\hat{\sigma}^\dagger\hat{\sigma}\right\rangle = \hbar\omega_0\Gamma_1\left(|\langle\hat{\sigma}\rangle|^2 + \left\langle\delta\hat{\sigma}^\dagger\delta\hat{\sigma}\right\rangle\right)\ . \tag{1.17}$$

[2] A measurement in the stationary state can be thought of as a measurement of an ensemble of TSLs interacting with light. This ensemble has a fraction that oscillates with the average dipole and emits correlated fields, but also a fluctuating fraction that gives rise to uncorrelated emission.

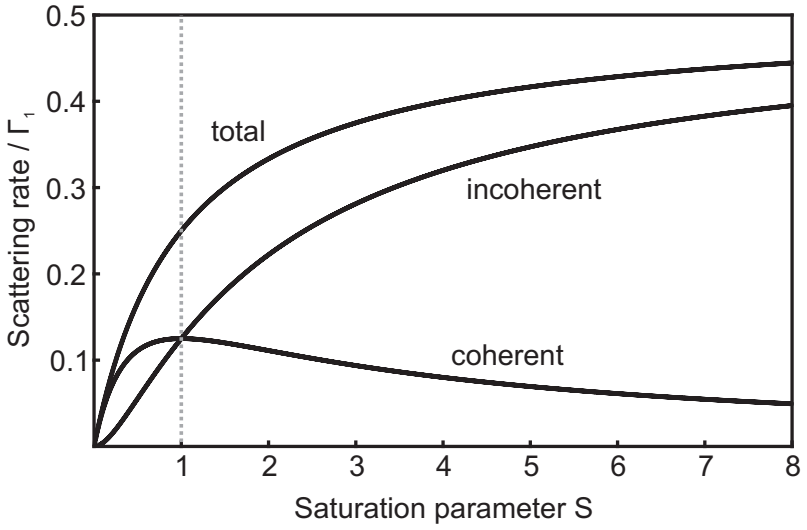

Figure 1.4: Dependence of coherent, incoherent and total scattering rate in units of Γ_1 as a function of saturation parameter with $\Gamma_2 = \Gamma_1/2$.

The first order correlation function $g^{(1)}(\tau)$ in Eq. (1.14) also splits into two parts

$$\begin{aligned} g^{(1)}(\tau) &= \frac{\left\langle \hat{\sigma}^\dagger(t)\right\rangle \left\langle \hat{\sigma}(t+\tau)\right\rangle}{\left\langle \hat{\sigma}^\dagger(t)\hat{\sigma}(t)\right\rangle} + \frac{\left\langle \delta\hat{\sigma}^\dagger(t)\delta\hat{\sigma}(t+\tau)\right\rangle}{\left\langle \hat{\sigma}^\dagger(t)\hat{\sigma}(t)\right\rangle} \\ &\rightarrow \frac{\left|\rho_{\mathrm{eg}}^{\mathrm{ss}}\right|^2}{\rho_{\mathrm{ee}}^{\mathrm{ss}}} , \quad \text{for } \tau \rightarrow \infty . \end{aligned} \tag{1.18}$$

The fluctuating part of the dipole will quickly become uncorrelated with itself and the second term in $g^{(1)}(\tau)$ decreases with a typical correlation time of $1/\Gamma_2$. However, the average dipole part will cause the emitted field to maintain a certain degree of correlation and $g^{(1)}(\tau)$ to approach a finite value for $\tau \rightarrow \infty$.

The normalized emission spectrum of the TLS can be calculated via the Wiener-Khintchine theorem (see e.g. chapter V.D in [42]) as the Fourier transform of its first order correlation function. The spectrum of the average dipole component in the rotating frame becomes

$$\begin{aligned} S_{\mathrm{coh}}(\omega_s) &= \frac{1}{2\pi}\int_{-\infty}^{\infty} \frac{\left|\rho_{\mathrm{eg}}^{\mathrm{ss}}\right|^2}{\rho_{\mathrm{ee}}^{\mathrm{ss}}} e^{i(\omega_s-\omega_{\mathrm{L}})\tau} d\tau \\ &= \frac{\left|\rho_{\mathrm{eg}}^{\mathrm{ss}}\right|^2}{\rho_{\mathrm{ee}}^{\mathrm{ss}}}\delta(\omega_s-\omega_{\mathrm{L}}) = \frac{1}{1+S}\delta(\omega_s-\omega_{\mathrm{L}}) , \end{aligned} \tag{1.19}$$

where the last equality sign is only true in the case of negligible dephasing.

This spectrum is a δ-function at the position of the exciting laser frequency. It is referred to as the coherent component because of its first order coherence, and is also known as elastic Rayleigh scattering. Like a classical dipole, the system oscillates at the laser frequency and reradiates at the same wavelength (with a certain phase shift that will become important for light extinction).

In terms of the saturation parameter S, the power of coherent scattering on resonance can be written as

$$P_{\rm coh} = \hbar\omega_0 \Gamma_1 |\tilde{\rho}_{\rm eg}^{\rm ss}|^2 = \hbar\omega_0 \frac{\Gamma_1^2}{4\Gamma_2} \frac{S}{(1+S)^2} \ . \tag{1.20}$$

$P_{\rm coh}$ grows linearly with the driving field for small intensities. It reaches a maximum at S=1, and decreases again at higher driving intensities. Figure 1.4 shows the coherent scattering rate as a function of saturation parameter. This behaviour has been described theoretically by Mollow [49].

The second, fluctuating component in Eq. (1.16) is called incoherent component and gives rise to a more complicated spectrum which will be presented below. However, its total power can be calculated from Eq. (1.20) and with $P_{\rm incoh} = P_{\rm sca} - P_{\rm coh}$ as

$$P_{\rm incoh} = \hbar\omega_0 \frac{\Gamma_1 S(\Gamma_2 + \Gamma_2 S - \Gamma_1/2)}{2\Gamma_2(1+S)^2} \xrightarrow{\Gamma_2=\Gamma_1/2} \hbar\omega_0 \frac{\Gamma_1}{2} \frac{S^2}{(1+S)^2} \ . \tag{1.21}$$

1.3.4 Spectrum of incoherent scattering, Mollow triplet

The full expression for $S(\omega_{\rm s})$ for a TLS driven by a monochromatic laser in the absence of dephasing was derived by Mollow in 1969 [49]. Like in this section, Mollow's treatment starts from a semiclassical theory of light-matter interaction and arrives at the two time atomic correlation function $\left\langle \hat{\sigma}^\dagger(t)\hat{\sigma}(t+\tau)\right\rangle$. The incoherent part of the spectrum, normalized to $P_{\rm sca}$, for strong ($\Omega > \Gamma_1/4$) on-resonance excitation and in the absence of dephasing has the form [40]

$$\begin{aligned} S_{\rm incoh}(\omega_s) &= \frac{1}{2\pi}\int_{-\infty}^{\infty} \frac{\left\langle \delta\hat{\sigma}^\dagger \delta\hat{\sigma}\right\rangle}{\rho_{\rm ee}^{\rm ss}} e^{i(\omega_s-\omega_{\rm L})\tau} d\tau \\ &= \frac{\Gamma_1/4\pi}{(\omega_0-\omega_s)^2 + (\Gamma_1/2)^2} \\ &+ \frac{3/2\Gamma_1\Omega_\Gamma(\Omega^2 - \Gamma_1^2/2) + \Gamma_1/2(5\Omega^2 - \Gamma_1^2/2)(\omega_0 + \Omega_\Gamma - \omega_{\rm s})}{8\pi\Omega_\Gamma(\Gamma_1^2/2 + \Omega^2)[(\omega_0 + \Omega_\Gamma - \omega_{\rm s}^2) + (3\Gamma_1/4)^2]} \\ &+ \frac{3/2\Gamma_1\Omega_\Gamma(\Omega^2 - \Gamma_1^2/2) - \Gamma_1/2(5\Omega^2 - \Gamma_1^2/2)(\omega_0 - \Omega_\Gamma - \omega_{\rm s})}{8\pi\Omega_\Gamma(\Gamma_1^2/2 + \Omega^2)[(\omega_0 - \Omega_\Gamma - \omega_{\rm s}^2) + (3\Gamma_1/4)^2]} \ . \end{aligned} \tag{1.22}$$

The inelastic part exhibits three peaks, the so-called Mollow triplet. The central peak is at $\omega_s = \omega_0$, the distance of the side maxima to the center is the damped Rabi frequency $\Omega_\Gamma = \sqrt{\Omega^2 - (\Gamma_1/4)^2}$. The FWHM of the three maxima is given by Γ_1 for the central, $3/2\Gamma_1$ for the side peaks. The height ratios are 1/3 to 1 to 1/3. Figure 1.5 shows the fluorescence triplet for different values of Ω, again for zero detuning and without dephasing.

At very strong excitation $\Omega_\Gamma \approx \Omega$ the spectrum consists of three approximately Lorentzian peaks, separated by the Rabi frequency. For small driving fields, when $\Omega < \Gamma_1/4$, Ω_Γ is imaginary, the three incoherent peaks fall together in the spectrum.

The triplet structure of the resonance fluorescence spectrum has been studied extensively, for a review see [50, 51]. A qualitative explanation for its occurence is that at strong driving fields the excited state population $\rho_{\rm ee}$ and hence the emission

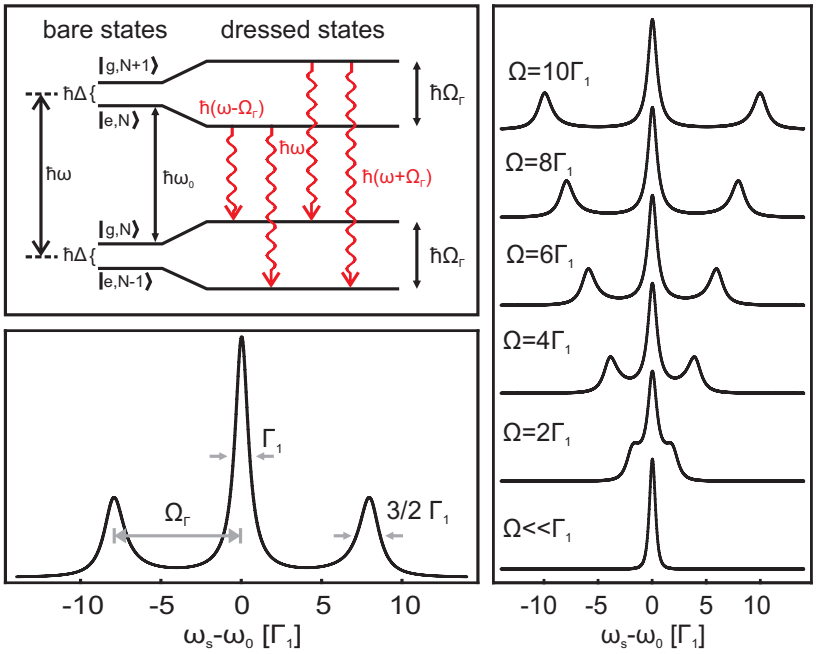

Figure 1.5: The Mollow fluorescence triplet. The upper left graph shows the occurence of the Mollow triplet as a fluorescence cascade down the ladder of dressed states in a strongly driven TLS coupled to a large number N of photons. The emission spectrum (lower left) for zero detuning exhibits two sidebands at a separation Ω_Γ from the central peak. The relative peak heights are 1:3:1 and the FWHM are 3:2:3. The coherent delta-peak at the laser frequency is not shown. On the right is the development of the spectrum for increasing resonant driving fields. For $\Omega < \Gamma_1/4$ the incoherent emission does not show a triplet.

probability is modulated by Rabi oscillations. The spectrum of a modulated emitter shows sidebands that are displaced by the modulation frequency from the carrier. In the dressed states picture, introduced by Cohen-Tannoudji and applied in chapter VI.C.3 of [42], the resonance fluorescence triplet can be understood as a cascade down the ladder of light-dressed atomic states. Since each atomic state is split into two dressed states with an energy spacing of Ω_Γ (on-resonance excitation), three different fluorescence frequencies are possible.

The TLS fluorescence spectrum consists of a first-order coherent component, which is the δ-like Rayleigh peak, and an incoherent component with a complex triplet structure. The second-order correlation function of the total emission will display antibunching, since the system is projected into its ground state after a photon emission. This is true as long as the emission time of the detected photons is well determined. Several theoretical works, e.g. [52, 53, 54] and also experiments [55, 56] have studied the second-order correlation function between frequency-filtered components of the fluorescence triplet. Spectral filtering will introduce a memory effect, depending on the spectral width of the filter. If this width is smaller than the inverse lifetime of the TLS, the emission time order of two consecutively detected

photons is no longer known, which destroys any correlation between the photons. For this reason, the second-order correlation function between Rayleigh scattered photons, which are narrowband-filtered from the incoherent central component of the fluorescence triplet, yields unity for all detection times [56]. For sufficiently strong driving fields and a well-separated triplet structure, the triplet sidebands can be frequency filtered with a bandwidth larger than the inverse lifetime. Correlation measurements display strong bunching between photons emitted successively into the different sidebands [55, 56].

1.4 Application to single molecule spectroscopy

The semiclassical description of interaction between a classical monochromatic light field and a quantum mechanical TLS can explain most of the phenomena observed in cryogenic single molecule spectroscopy. In fact, a dye molecule immobilized in a matrix at low enough temperature can constitute a surprisingly well-behaved realization of a TLS [57]. In the following I will elaborate on this by referring to the typical level-structure of a dye molecule in Fig. 1.1 under nearly resonant optical excitation, and explain how the triplet and vibrational levels of the system can be taken into account.

1.4.1 Optical Bloch equations

For small detunings the excitation light couples the singlet states $|S_0\rangle = |1\rangle$ and $|S_1\rangle = |2\rangle$. These states are non-degenerate and isolated, which allows one to approximate the molecule as a TLS. Light driven transitions into other levels (higher electronic, but also vibrational or phonon wing states) give a negligible contribution, since these levels are energetically far enough separated [57]. One has to consider that spontaneous emission events can not only project the system back to $|1\rangle$ but also into vibrational levels of $|1\rangle$. However, these states will quickly relax in a radiationless manner [27, 58], and their stationary state population is negligible. The manifold of vibrational levels of $|1\rangle$ and their phonon wings is introduced by an additional level $|3\rangle$. A more noticeable deviation is a singlet-triplet intersystem crossing.

In what follows, I will analyze the evolution of a molecule with a transition energy of $\hbar\omega_0$ in a monochromatic, classical laser field of angular frequency ω_L. The detuning $\Delta = \omega_\mathrm{L} - \omega_0$ is sufficiently small to apply the rotating wave approximation. At the beginning, the complete level structure in Fig. 1.1 will be taken into account in a four-level optical Bloch equation. The spontaneous decay from $|2\rangle$ is introduced with the longitudinal decay rate $\Gamma_1 = k_{21} + k_{23} + k_\mathrm{ST}$, and damping of the coherence between $|1\rangle$ and $|2\rangle$ is accounted for by the transversal decay rate $\Gamma_2 = \frac{1}{2}\Gamma_1 + \Gamma_2^*$.

The equations of motion for the density matrix elements in the rotating frame

(laser frame) are [23, 33]

$$\begin{aligned}
\dot{\tilde{\rho}}_{12} &= -\frac{1}{2}i\Omega\left(\rho_{22}-\rho_{11}\right)-\left(i\Delta+\Gamma_2\right)\tilde{\rho}_{12} \\
\dot{\rho}_{11} &= \frac{1}{2}i\Omega\left(\tilde{\rho}_{12}-\tilde{\rho}_{21}\right)+k_{21}^{\mathrm{ZP}}\rho_{22}+k_{31}\rho_{33}+k_{\mathrm{TS}}\rho_{\mathrm{TT}} \\
\dot{\rho}_{22} &= -\frac{1}{2}i\Omega\left(\tilde{\rho}_{12}-\tilde{\rho}_{21}\right)-\left(k_{21}+k_{23}+k_{\mathrm{ST}}\right)\rho_{22} \\
\dot{\rho}_{33} &= k_{23}\rho_{22}-k_{31}\rho_{33} \\
\dot{\rho}_{\mathrm{TT}} &= k_{\mathrm{ST}}\rho_{22}-k_{\mathrm{TS}}\rho_{\mathrm{TT}}\ . \qquad (1.23)
\end{aligned}$$

Lattice and molecular vibrations open additional channels for the spontaneous decays of the excited state, and consequently the purely electronic transition dipole moment $d_{21}=\left\langle 1|\hat{d}|2\right\rangle$ is decreased by $\sqrt{\alpha}=\sqrt{\alpha_{\mathrm{DW}}\alpha_{\mathrm{FC}}}$, the square root product of Debye-Waller and Franck-Condon factors[3]. The Rabi frequency Ω now has the form $\Omega=-\frac{1}{\hbar}\sqrt{\alpha}d_{21}E_0$.

The stationary states of Eq. (1.23) with the boundary condition

$$\rho_{\mathrm{TT}}+\rho_{11}+\rho_{22}+\rho_{33}=1$$

can again be written in a Lorentzian form, if an effective linewidth Γ_{eff} is introduced

$$\begin{aligned}
u^{\mathrm{ss}} &= \frac{\Omega\Delta}{2\left(\Delta^2+\Gamma_{\mathrm{eff}}^2\right)} \\
v^{\mathrm{ss}} &= \frac{\Omega\Gamma_2}{2\left(\Delta^2+\Gamma_{\mathrm{eff}}^2\right)} \\
\rho_{22}^{\mathrm{ss}} &= \frac{\Omega^2\Gamma_2}{2\Gamma_1\left(\Delta^2+\Gamma_{\mathrm{eff}}^2\right)}\ , \qquad (1.24)
\end{aligned}$$

as well as the triplet population

$$\rho_{\mathrm{TT}}^{\mathrm{ss}}=\frac{k_{\mathrm{ST}}/k_{\mathrm{TS}}\Omega^2\Gamma_2}{2\Gamma_1\left(\Delta^2+\Gamma_{\mathrm{eff}}^2\right)}\ , \qquad (1.25)$$

with

$$\begin{aligned}
\Gamma_{\mathrm{eff}}^2 &= \Gamma_2^2+\Omega^2K\frac{\Gamma_2}{\Gamma_1} \\
K &= 1+\frac{1}{2}\left(\frac{k_{23}}{k_{31}}+\frac{k_{\mathrm{ST}}}{k_{\mathrm{TS}}}\right) \\
&\simeq 1+\frac{k_{\mathrm{ST}}}{2k_{\mathrm{TS}}}\ , \quad k_{31}\gg k_{23}\ . \qquad (1.26)
\end{aligned}$$

The approximation $k_{31}\gg k_{23}$ is reasonable given the short lifetimes of vibrational and phonon wing states [27]. With k_{ST}=1250 s^{-1} and k_{TS}=4500 s^{-1} for DBATT in *n*-hexadecane [25], the factor K amounts to approximately $K=1.14$.

[3] in reference [59] we only included the Debye-Waller factor in the equation for the reduced dipole moment. In order to simplify the formulation of extinction spectroscopy (see chapter 2), I chose to include also the Franck-Condon factor at this point.

From Eqs. (1.24), the emitted fluorescence rate R_{fluo} of a molecule excited near resonance can be calculated according to $R_{\text{fluo}} = \Gamma_1 \rho_{22}^{\text{ss}}$. A system with triplet state shows the typical saturation behavior, however, including the triplet correction factor according to

$$\rho_{22}^{\text{ss}} = \frac{1}{2} \frac{S}{1 + KS} \ . \tag{1.27}$$

The populations of the excited and triplet state for S$\rightarrow \infty$ are

$$\rho_{22}^{\text{sat}} = \frac{1}{2K} \ , \quad \rho_{\text{TT}}^{\text{sat}} = \frac{K-1}{K} \ . \tag{1.28}$$

For the case of DBATT in *n*-hexadecane, the maximum triplet population is 13 %. The discussion about resonance fluorescence also applies to the zero phonon line of single molecules, taking into account the factor K.

1.5 Experimental realizations

Experiments on atomic ensembles and beams, as well as single trapped ions, have given an insight into resonance fluorescence phenomena of real quantum systems. The first observations of the incoherent fluorescence triplet were realized by the study of atomic Sodium beams [60, 61, 62]. Additionally, in [62] the resonance fluorescence spectrum of Barium showed a narrower than natural linewidth for small driving fields, a phenomenon first shown by Gibbs and Venkatesan [63]. This is the coherent component of the spectrum which was later shown for a single Magnesium ion to be only limited by the laser linewidth and as narrow as 0.7 Hz [64]. The second order correlation function and antibunching in such systems can be measured with start-stop schemes first introduced by Hanbury Brown and Twiss [65] with two photodetectors [66].

In solid state systems the observation of resonance fluorescence is challenging, mainly because of strong spurious scattering of the excitation laser light from interfaces or the sample matrix. The literature on this topic is very scarce and mostly limited to theoretical work. One can study resonant processes via coherently scattered light and its interference with excitation light, as has been done in quantum dot systems, e.g. [67, 68, 69], and molecules [59, 70, 71]. This aspect will be topic of chapter 2. Recently, progress has been made with quantum dots in waveguide-type structures, where the emission was collected perpendicular to the excitation light and could directly be studied [72, 73]. However, the spectral properties of resonance fluorescence from single solid-state quantum systems could only be deduced indirectly from the determination of the first order correlation function [72] or pump - differential probe transmission spectroscopy [74].

The second order correlation function of the red shifted fluorescence of single molecules can be studied fairly easily after blocking the excitation light [30, 75], and the same is true for above-resonance excitation of NV centers in diamond [76] and quantum dots [77]. Antibunching in resonance fluorescence from a single quantum dot was only measured recently by Müller et al. [48].

2 Extinction Spectroscopy

2.1 Scattering, extinction and absorption

Extinction, the attenuation of light by an obstacle, is explained in scattering theory as the result of interference between the excitation light and elastically scattered radiation [44, 78, 79]. A very instructive picture of wavelength-dependent extinction has been given in [80] for metal nanoparticles excited on and off their plasmon resonance, and in [81] for the case of an ideal TLS. In this chapter I will discuss expressions for the total power measured in the far field, given a TLS at the origin illuminated with near-resonant excitation light.

A resonantly excited TLS only scatters light, and the scattering is purely coherent in the low excitation limit. As a first approximation I will therefore treat the TLS as a classical dipole, and later introduce saturation effects. The excitation electric field $\mathbf{E}_{\text{inc}}^{(\pm)}$ and the scattered dipolar field $\mathbf{E}_{\text{sca}}^{(\pm)}$ add up to give a total field at any point $\mathbf{r}$

$$\begin{aligned} \mathbf{E}_{\text{total}}^{(\pm)}(\mathbf{r},t) &= \mathbf{E}_{\text{inc}}^{(\pm)}(\mathbf{r},t) + \mathbf{E}_{\text{sca}}^{(\pm)}(\mathbf{r},t) \\ \left\langle \mathbf{E}_{\text{total}}^{(-)}\mathbf{E}_{\text{total}}^{(+)} \right\rangle &= \left\langle \mathbf{E}_{\text{inc}}^{(-)}\mathbf{E}_{\text{inc}}^{(+)} \right\rangle + \left\langle \mathbf{E}_{\text{sca}}^{(-)}\mathbf{E}_{\text{sca}}^{(+)} \right\rangle + 2\Re\left\{ \left\langle \mathbf{E}_{\text{inc}}^{(-)}\mathbf{E}_{\text{sca}}^{(+)} \right\rangle \right\} \\ I_{\text{total}} &= I_{\text{inc}} + I_{\text{sca}} + I_{\text{intf}} \ , \end{aligned} \tag{2.1}$$

where I have introduced the intensity $I = \left\langle \mathbf{E}^{(-)}\mathbf{E}^{(+)} \right\rangle$ time-itegrated over at least one optical cycle. The integral of I over an extended detector of area Σ is proportional to power in counts per second (cps)

$$\begin{aligned} P_{\text{total}} &= \varsigma \int_{\Sigma} I_{\text{total}} \mathrm{dA} \\ P_{\text{total}} &= P_{\text{inc}} + P_{\text{sca}} + P_{\text{intf}} \ . \end{aligned} \tag{2.2}$$

The proportionality factor $\varsigma = \frac{\epsilon_0 c}{2\hbar\omega}$ converts field squared into photoelectron counts per second. $\frac{\epsilon_0 c}{2}E^2$ is an energy flux density, equal to the absolute value of the Poynting vector, and $\hbar\omega$ the energy of one photon.

Figure 2.1 gives an intuitive picture for the extinction of a gaussian light beam by a dipole in the focus. Figure 2.1 a) is I_{inc}, the squared and time-averaged electric field of a gaussian beam with a waist w_0 of 0.75 λ. The plotted area is 20x10 λ. Figure 2.1 b) is I_{sca}, the squared and time averaged scattered field of a resonantly driven classical dipole. For demonstration purposes the strength of total dipole emission is adjusted to yield comparable field amplitudes of dipole and gaussian beam in the far field. The dipole moment is along the polarization direction of the excitation beam.

Finally, Fig. 2.1 c) shows I_{total}, the squared and time-averaged sum of both fields. This is the intensity a detector at any point in the plane would register. A focused Gaussian beam acquires a Gouy phase of $-\pi/2$ from the focus to the far field, as compared to a plane wave at a fixed time [82]. In addition, the resonantly driven dipole reradiates with a phase shift of $\pi/2$ compared to the driving field. The total phase difference between the two fields in the forward direction becomes π, and the interference is destructive. In the backward direction, however, the counter-propagating fields result in a standing wave. Energy is conserved in the whole process; the effect of the dipole is an energy redistribution by interference.

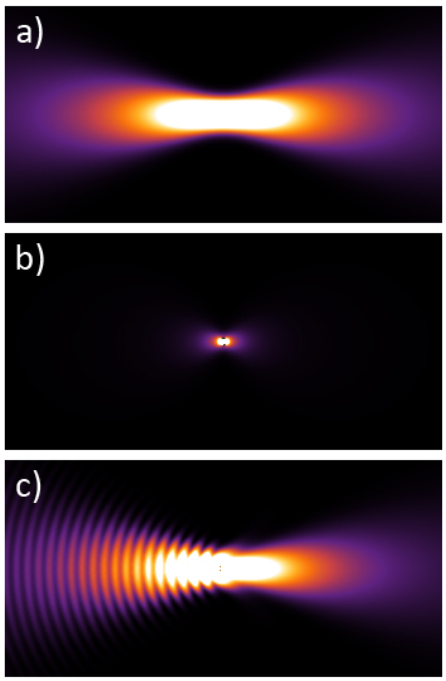

Figure 2.1: Time averaged field intensities of a) the gaussian excitation beam, b) the scattered dipolar field and c) the sum of both field contributions. The waist is 0.75 λ and the gaussian beam is incident from the left.

A large mode overlap between the ongoing excitation field and the scattered dipole wave results in a strong destructive interference, and hence a large interaction between the incident light and the oscillator. The optimal case is to send a dipolar excitation field, which will be perfectly reflected by a classical undamped dipole [83]. For a general excitation light distribution, one can perform a multipole expansion of the incident field around the origin [44, 83, 84, 85, 86]. The dipole component will be fully reflected. All other multipole components of the incident light are orthogonal to the dipole emission [44] and cannot contribute to an integrated interference term. An equivalent argumentation is that only the dipole wave component has a finite field E_0 at the origin [87]. The other multipole components can not drive any optical (dipole-)transitions and only contribute to the background of a transmission measurement.

Two idealizations will usually be lost in experiments. First, a quantum mechanical TLS shows saturation, i.e. a growing incoherent fraction in the total scattered radiation with increasing excitation intensity. This incoherent component does not interfere with the excitation light and consequently the observed extinction decreases. Secondly, if a single molecule does not only scatter, but also absorb light and re-emits the absorbed energy in any (possibly undetected) form, the observed extinction decreases as well. What this means for the total extinguished power will be shown later in this chapter.

With a positive sign the interference term is also called extinguished power P_{ext}. Throughout this and the experimental chapters, P_{intf} and P_{ext} are used both, depending on whether the sign of this term is of importance or the absolute amount of extinction is discussed.

2.2 Extinction cross section

The concept of an extinction cross section quantifies the interaction between a scatterer and an incoming wave by modeling the scatterer as a classical disk of a certain size inside which all of the incoming wave is affected. It is defined as the ratio of total extinct power to the incident power per unit area, $\sigma_{\text{ext}} = P_{\text{ext}}/I_{\text{inc}}$. If the fields of a plane wave and a TLS (see Eq. (1.13)) are inserted to Eq. (2.1), the integration of P_{intf} over a 4π solid angle gives the result that the total extinction is equal to the total emitted resonance fluorescence [88], as expected from an energy conservation argument

$$P_{\text{ext}} = -\frac{\epsilon_0 c}{2\hbar\omega_0}\int_{4\pi} I_{\text{intf}}\text{dA} = \Gamma_1\rho_{\text{ee}}^{\text{ss}} \ . \tag{2.3}$$

The extinction cross section can now easily be obtained by taking the total extinct power via Eqs. (2.3) and (1.10). The incident power per unit area is just the intensity of a plane wave at the origin times ς. With $S = \frac{\Omega^2}{\Gamma_1\Gamma_2}$ the on-resonance cross section is

$$\begin{aligned} P_{\text{ext}} &= \Gamma_1\rho_{\text{ee}}^{\text{ss}} = \frac{\Gamma_1}{2}\frac{S}{1+S} \ , \quad I_{\text{inc}} = \frac{\epsilon_0 c}{2\hbar\omega_0}E_0^2 \\ \sigma_{\text{ext}} &= \frac{\Gamma_1 d_{\text{ge}}^2 E_0^2}{\hbar^2\Gamma_1\Gamma_2}\frac{1}{1+S}\frac{2\hbar\omega_0}{\epsilon_0 c E_0^2} = \frac{3\lambda_0^2}{2\pi}\frac{\Gamma_1}{2\Gamma_2}\frac{1}{1+S} \ . \end{aligned} \tag{2.4}$$

For the last step I have used the relation $\frac{c}{\omega_0} = \frac{\lambda_0}{2\pi}$, as well as the definition of the Einstein A coefficient, which is equal to Γ_1

$$\Gamma_1 = \frac{\omega_0^3 d_{\text{ge}}^2}{3\pi\epsilon_0\hbar c^3} \ . \tag{2.5}$$

Equation (2.4) shows that at low excitation power and without dephasing, the extinction cross section of a TLS is $\sigma_{\text{ext}} = \frac{3\lambda_0^2}{2\pi}$. This quantity only depends on the resonance wavelenth. Dephasing and saturation decrease the extinction cross section.

2.3 Detected signals in the far field

Eq. (2.1) describes the total field at any point in the far field. The amplitude and phase of the involved fields have to be known in order to derive an expression for the detection signal.

Resonance fluorescence term

The molecular resonance fluorescence in the far field with polarization $\hat{\epsilon}$ can be written in detail using the source field expression of Eq. (1.13). Using Eq. (1.16)

one can also calculate the coherently scattered field and intensity

$$\begin{aligned}
\mathbf{E}_{21}^{(+)} &= \sqrt{\alpha}\frac{-\omega_0^2 d_{21}}{4\pi\epsilon_0 c^2}\frac{[(\hat{\mathbf{r}}\cdot\hat{\epsilon})\hat{\mathbf{r}}-\hat{\epsilon}]}{r}\hat{\sigma} \\
I_{21} &= \alpha\frac{\omega_0^4}{16\pi^2\epsilon_0^2 c^4}\frac{\sin^2(\theta)}{r^2}d_{21}^2\left\langle\hat{\sigma}^\dagger\hat{\sigma}\right\rangle =: |f|^2\alpha d_{21}^2\rho_{22}^{\mathrm{ss}} \\
I_{\mathrm{coh}} &= \alpha\frac{\omega_0^4}{16\pi^2\epsilon_0^2 c^4}\frac{\sin^2(\theta)}{r^2}d_{21}^2|\left\langle\hat{\sigma}\right\rangle|^2 =: |f|^2\alpha d_{21}^2|\rho_{12}^{\mathrm{ss}}|^2 \ , \qquad (2.6)
\end{aligned}$$

where I have used $|(\hat{\mathbf{r}}\cdot\hat{\epsilon})\hat{\mathbf{r}}-\hat{\epsilon}|^2 = 1-|\hat{\epsilon}\cdot\hat{r}|^2 = \sin^2(\theta)$ for a dipole oriented along $\theta = 0$, i.e. perpendicular to the optical axis. Note that one factor α is included in ρ_{22}^{ss} and $|\rho_{12}^{\mathrm{ss}}|^2$ and accounts for the decreased Rabi frequency, as explained in section 1.4, and a second factor α is inserted in the intensities as the fraction of resonance fluorescence in the total emitted power.

The complex modal factor $f(\theta,\varphi) = |f|e^{i\phi_f}$ bundles some factors and describes the amplitude and phase of the molecular field at any point in the far field, emitted by the dipole $\sqrt{\alpha}d_{21}$ at the origin, and taking into account possible interfaces and boundaries in the detection path.

Integration of ςI_{21} over 4π with $\mathrm{dA} = \mathrm{r}^2\sin(\theta)\mathrm{d}\theta\mathrm{d}\varphi$ and introduction of Γ_1 via Eq. (2.5) yields the expression $P_{21} = \alpha\Gamma_1\rho_{22}^{\mathrm{ss}}$ for the total resonance fluorescence power, consistent with Eq. (1.10).

Incident field

Similarly, the excitation field at the detector can be written in terms of the field E_0 at the position of the molecule

$$I_{\mathrm{inc}} =: |g|^2 E_0^2 \ , \qquad (2.7)$$

where the complex modal factor $g(\theta,\varphi) = |g|e^{i\phi_g}$ describes the angular distribution of amplitude and phase of the excitation field.

Detector signal

With the above expressions, and using the equalities $\langle\hat{\sigma}\rangle = \rho_{12}^{\mathrm{ss}} = (u^{\mathrm{ss}} - iv^{\mathrm{ss}})$ and

$\Omega = -\frac{\sqrt{\alpha} d_{21} E_0}{\hbar}$, all terms of Eq. (2.1) can be written as

$$
\begin{aligned}
I_{\text{total}} &= I_{\text{inc}} + I_{21} + I_{\text{intf}} \qquad (2.8)\\
I_{\text{inc}} &= |g|^2 E_0^2 \\
I_{21} &= |f|^2 \alpha d_{21}^2 \rho_{22}^{\text{ss}} = |f|^2 \alpha d_{21}^2 \frac{1}{2} \frac{\alpha d_{21}^2 E_0^2 \Gamma_2 / \hbar^2}{2\Gamma_1 (\Delta^2 + \Gamma_{\text{eff}}^2)} \\
&= \underbrace{\left|\frac{f}{g}\right|^2 \frac{\alpha^2 d_{21}^4}{2\hbar^2 \Gamma_1 \Gamma_2}}_{C_{21}} I_{\text{inc}} \frac{\Gamma_2^2}{\Delta^2 + \Gamma_{\text{eff}}^2} \\
I_{\text{intf}} &= 2\Re\{E_{\text{inc}}^{(-)} E_{\text{coh}}^{(+)}\} = 2\Re\{g^* E_0^{(-)} f \sqrt{\alpha} d_{21} \langle \hat{\sigma} \rangle\} \\
&= 2|gf| \sqrt{\alpha} d_{21} E_0 \Re\{\frac{e^{i(\phi_{\text{f}} - \phi_{\text{g}})} \Omega (\Delta + i\Gamma_2)}{2(\Delta^2 + \Gamma_{\text{eff}}^2)}\} \\
&= -2 \underbrace{\left|\frac{f}{g}\right| \frac{\alpha d_{21}^2}{2\hbar \Gamma_2}}_{C_{\text{intf}}} I_{\text{inc}} \frac{\Gamma_2 (\Delta \cos\phi + \Gamma_2 \sin\phi)}{\Delta^2 + \Gamma_{\text{eff}}^2} \ ,
\end{aligned}
$$

and

$$
\begin{aligned}
I_{\text{coh}} &= |f|^2 \alpha d_{21}^2 |\rho_{12}^{\text{ss}}|^2 = |f|^2 \alpha d_{21}^2 \frac{1}{4} \frac{\alpha d_{21}^2 E_0^2 / \hbar^2 (\Delta^2 + \Gamma_2^2)}{(\Delta^2 + \Gamma_{\text{eff}}^2)^2} \\
&= \underbrace{\left|\frac{f}{g}\right|^2 \frac{\alpha^2 d_{21}^4}{4\hbar^2 \Gamma_2^2}}_{C_{\text{intf}}^2} I_{\text{inc}} \frac{\Gamma_2^2 (\Delta^2 + \Gamma_2^2)}{(\Delta^2 + \Gamma_{\text{eff}}^2)^2} \ . \qquad (2.9)
\end{aligned}
$$

One point to make is that the coherently scattered power is not a Lorentzian fuction of Δ, but exhibits a double-peak structure at strong driving fields.

2.4 Other decay channels and intensity dependence

The above equations show that additional decay channels, quantified with the factor $\alpha = \alpha_{\text{DW}} \alpha_{\text{FC}}$, lead to a decrease of interaction of a single molecule with the incident light, compared to an ideal TLS. As Eqs. (2.8) show, the total extinguished power P_{ext} is reduced by a factor α. This power is now distributed between resonance fluorescence P_{21}, which is reduced by a factor α^2, and absorbed power. Absorption is here defined as the energy that is converted into any form of energy aside from resonance fluorescence, and in particular covers any transitions into phonon wing and vibrational levels, i.e. Stokes shifted fluorescence. If one introduces an effective dipole moment for the vibrational transitions, $d_{23} = \sqrt{1-\alpha} d_{21}$, the amount of power per unit area that is absorbed by the molecule and reradiated as red-shifted photons becomes

$$
I_{23} = |f|^2 (1-\alpha) d_{21}^2 \rho_{22}^{\text{ss}} = \underbrace{\left|\frac{f}{g}\right|^2 \frac{(\alpha - \alpha^2) d_{21}^4}{2\hbar^2 \Gamma_1 \Gamma_2}}_{C_{23}} I_{\text{inc}} \frac{\Gamma_2^2}{\Delta^2 + \Gamma_{\text{eff}}^2} \ . \qquad (2.10)
$$

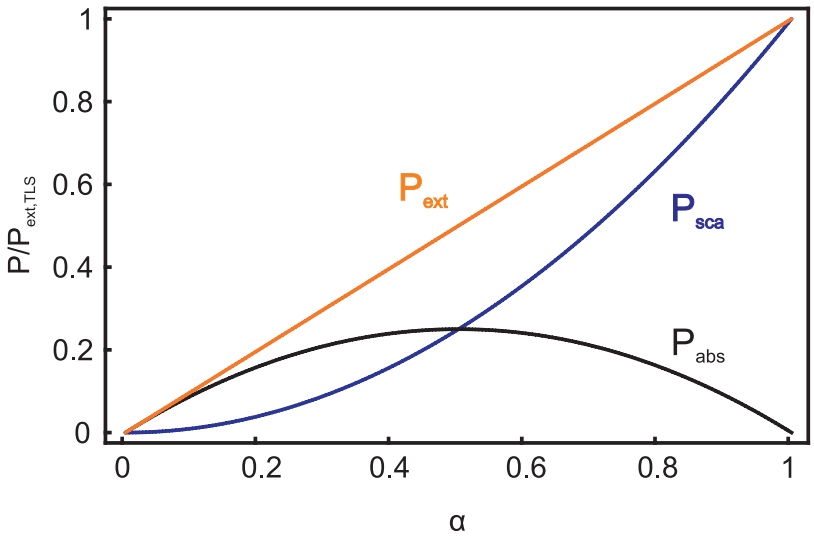

Figure 2.2: Energy conservation in extinction, scattering and absorption for a system that deviates from an ideal two-level case. The plot shows total extinguished, scattered and absorbed powers as a function of α according to Eq. (2.11), normalized to the power extinguished by an ideal TLS.

Figure 2.2 shows the extinguished, resonance fluorescence and absorbed power from a TLS with additional decay channels as a function of α, the fraction of resonance fluorescence. This is for a fixed P_{inc} at $S \ll 1$ and normalized to the extinguished power for an ideal TLS. For a value of α=0.5 the absolute value of absorbed power has a maximum. The figure also shows, as van de Hulst remarks in [78]: "A 'black' obstacle, that absorbs light but does not scatter any, cannot exist".

The dependence of the detected P_{21}, P_{ext} as well as P_{coh} and P_{23} on molecular parameters like α and the dephasing "parameter" $2\Gamma_2/\Gamma_1$ is very insightful. Keeping in mind that $\Gamma_1 \propto d_{12}^2$, one can see that

$$P_{\text{ext}} \propto \alpha\frac{\Gamma_1}{2\Gamma_2}\ , \quad P_{\text{coh}} \propto \alpha^2\frac{\Gamma_1^2}{4\Gamma_2^2}\ , \quad P_{21} \propto \alpha^2\frac{\Gamma_1}{2\Gamma_2}\ , \quad P_{23} \propto (\alpha-\alpha^2)\frac{\Gamma_1}{2\Gamma_2}\ . \tag{2.11}$$

The factor α describes the branching ratio between resonance fluorescence and absorption, the factor $\Gamma_1/2\Gamma_2$ describes the branching ratio between coherent and incoherent resonance fluorescence. Both factors linearly influence P_{ext}, but are linearly or quadratically involved in the different components of the total detected signal. However, the 4π integrated sum of P_{coh}, P_{incoh} and P_{23} always yields P_{ext}.

If one considers these effects in Eq. (2.4), the total on-resonance extinction cross section for a single molecule under plane wave illumination is given by

$$\sigma_{\text{ext}} = \frac{3\lambda_0^2}{2\pi}\alpha_{\text{DW}}\alpha_{\text{FC}}\frac{\Gamma_1}{2\Gamma_2}\frac{1}{(1+S)}\ . \tag{2.12}$$

2.5 Experimental realizations

The attenuation a beam of light with an area A suffers by the presence of a single quantum system can be approximated as

$$P_{\text{total}} = \frac{\sigma_{\text{ext}}}{A} P_{\text{inc}} \ . \tag{2.13}$$

The extinction cross section was so far only calculated for plane wave excitation. The same quantity can be used for arbitrary illumination, if the focal beam waist A is calculated for the given focusing geometry and field distribution. Different scenarios are explained in [83]. It is shown that an ideal half-space focusing optics with a numerical aperture of 1 can result in roughly 87% extinction of a plane wave, and total extinction of a directional dipole wave. Experimental realizations of such a setup are mainly limited technologically. In gaseous systems like ion or atom traps, the focusing optics cannot reach high numerical apertures. Solid state systems suffer from dephasing and additional vibronic transitions. Nonetheless, experimental efforts towards reaching strong extinction of light by a single quantum system have been recently pursued in several labs. In the papers on this topic, the terms absorption and extinction are often used for the same effect, namely the attenuation of an ongoing excitation beam in forward direction. The first experiments were done in 1987 by Wineland, Itano and Bergquist on a single Mercury ion in a trap [1]. Shortly after, in 1989, Moerner and Kador achieved the first optical detection of a single impurity molecule via extinction spectroscopy [2]. Quantum dots have been studied via extinction for a few years, both with near-field excitation [14], and far-field optics [68, 89]. In all these cases, the effect of the single quanum system has been minute, and modulation techniques had to be employed. In the past year, due to better suited solid-state emitters and new experimental techniques, the visibility in these extinction experiments could be increased to several percent [17, 18, 59], and in some cases modulation and lock-in techniques are no longer needed.

Experimental projects aim at reaching complete extinction of a single photon by an ideal single quantum system [90] by time-reversing the spontaneous emission process. In this experiment, the incident light will be offered from 4π solid angle with radial polarization [91]. Also, the temporal shape of the photon wavepacket should be a time-reversed copy of a spontaneously emitted photon [92].

3 Experimental setup

The experimental setup was used in a similar form for the cryogenic near-field experiments that are explained in detail in Ilja Gerhardt's thesis [93] and in short in chapter 7. A different perspective on the optical setup and the cryostat can therefore be found in [93]. The main new advancement here has been the introduction of a solid immersion transmission microscopy setup. Therefore, I will put some weight on the new applications of solid immersion lens (SIL) microscopy in cryogenic single molecule spectroscopy, as well as a characterization of the system.

3.1 Optical setup

Laser source and beam parameters

A `Coherent 899-21` autoscan dye ring laser is used as a narrowband, widely tunable laser source in the wavelength range between 580 and 620 nm. It is operated with rhodamine 6G, and pumped with a 532 nm `Coherent Verdi V8` frequency doubled Nd:Vanadate. The dye laser has a tuning range of 30GHz, and can be scanned over several tens of nm by sequential 10 GHz scans. An autoscan unit provides an absolute frequency measurement with an accuracy of about 50 MHz. The out-coupled laser beam has a $1/e^2$ diameter of circa 1 mm, a typical power of several hundred mW, and a linewidth of less than 1 MHz.

The laser beam then passes a `Panasonic EFLM` 200 MHz acousto-optical modulator (AOM) for intensity stabilization, as explained in the next paragraph. The first order of the AOM is coupled into a single mode fiber patchcord, `Nufern HP460`, with a mode feed diameter of $3.5 \pm 0.5\ \mu m$ and numerical aperture (N.A.) of 0.13, and transfered to the experimentation table. Here, a $10\times$ objective with $N.A. = 0.25$ is used to collimate the beam, which results in a transverse electromagnetic TEM_{00} gaussian profile with a $1/e^2$ beam diameter of 3 mm and an ellipticity of 0.98, as measured with a CMOS camera. The knowledge and optimization of the beam intensity profile is important to increase the performance of the focusing lens in the cryostat. The light subsequently passes through a linear polarizing Glan Taylor Calcite Polarizer (`Thorlabs GT10`) to ensure a defined vertical polarization in the setup.

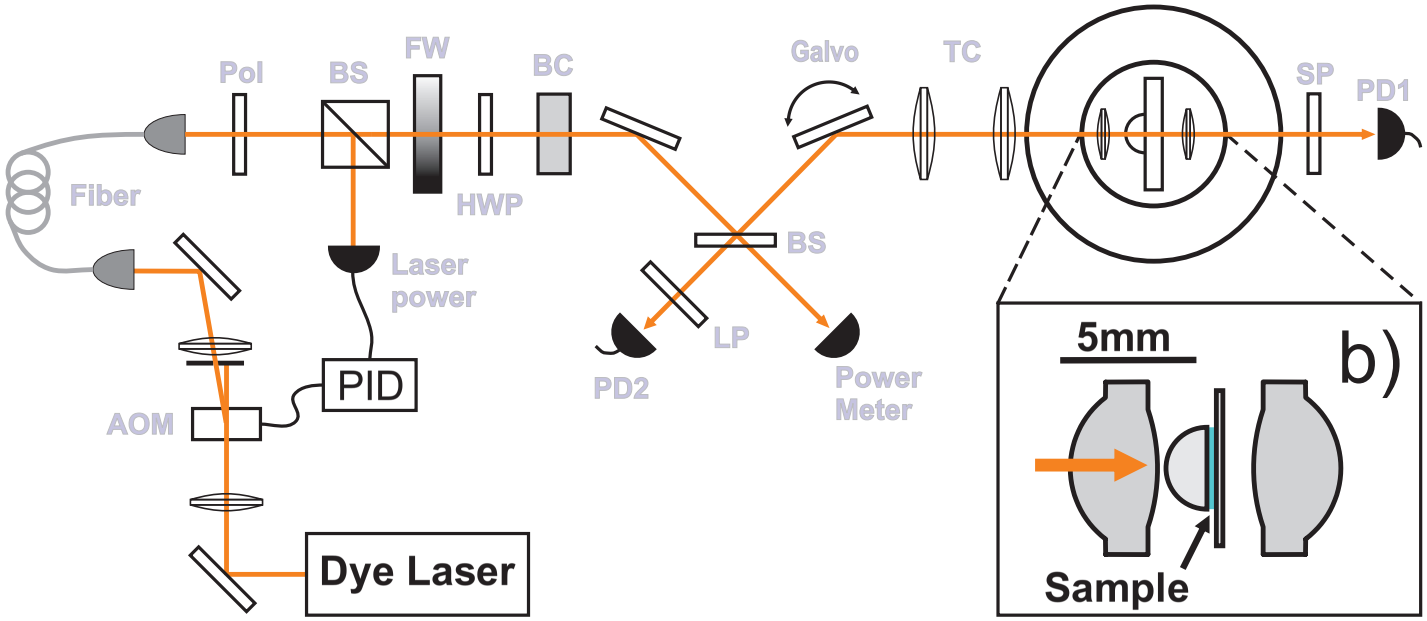

Figure 3.1: The path of the excitation light from the dye laser up to the sample is described step by step in the text. The abbreviations are: acousto-optical modulator (AOM), calcite polarizer (Pol), beamsplitter (BS), photodiode (PD), variable grey filter wheel (FW), multi-order half wave plate (HWP), variable waveplate or Berek Compensator (BC), optical long-pass filter (LP), Galvoelectric scanning mirrors (Galvo), telecentric lens system (TC), optical short-pass filter (SP). Also shown is a magnification of the optical setup inside the cryostat with two aspheric lenses and the solid immersion lens.

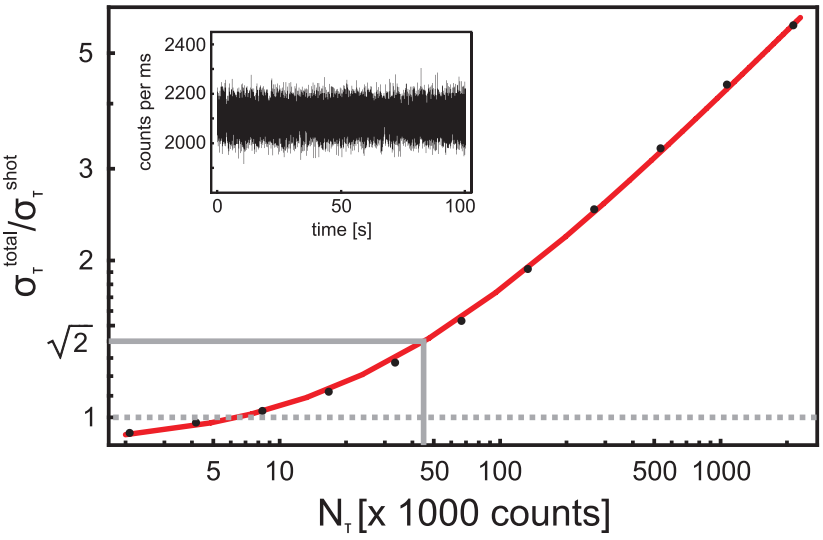

Figure 3.2: Noise characteristics of the PID stabilized excitation laser, measured on PD1 in Fig. 3.1. Shown is the total noise normalized by the expected shot noise for a given total counts per scan-bin, assuming that the excitation light power is much larger than the detector dark counts.

Laser intensity stabilization and control

Most intensity fluctuations in this setup are either directly caused by the instabilities in the dye jet, or polarization changes of the light guided by the single mode fiber, which are translated to intensity changes after the linear polarizer at the fiber output [94]. To stabilize the intensity of the laser beam, a part of the light was split with a 92/8 pellicle beam splitter (`Thorlabs BP108`) and directed onto an amplified photodiode [93]. The signal of the photodiode was fed into a home-built PI control-loop feedback, which in turn was connected to the modulation input of the AOM driver. After a stable laser intensity was obtained, a set of absorptive neutral density filters [FW] could be used to attenuate the excitation power by up to 9 orders of magnitude. The intensity of the excitation laser light needed to be adjustable over several orders of magnitude in order to study the interaction of light with single molecules in both the low excitation and the very high excitation regime. The PI-system also allowed for fine-tuning of the laser intensity by changing the desired set-point. Care was taken to align the filter set in such a way that the focus on the sample did not move noticably when changing the filters. The input power was continuously monitored on a calibrated powermeter behind the beam splitter BS shown in Fig. 3.1, and the measured power at this position corresponded to a power reduced by a factor of roughly 1/30 directly in front of the cryostat.

We worked in photon counting mode with an avalanche photodiode (APD) as a detector. The limiting factor for any intensity measurement is the shot noise, which is given by the square root of the mean counts per data point. The relative contribution of shot noise can be reduced by increasing the number of counts per data point, either with a longer integration time or by increasing the light intensity.

This is in contrast to laser amplitude noise [95], which is linear in the light intensity and is not averageable. Figure 3.2 shows a measurement to characterize the noise of our laser system. An intensity trace as shown in the inset was recorded for 100 seconds on PD1 in Fig. 3.1 for a given stabilized laser power P_{laser} of approximately 2.1 million counts per second. This is the typical power we used for later extinction measurements. The integration time was 1ms, i.e. the counts per data point are roughly N_0 =2100. This trace was used to simulate data sets with longer integration times $\tau \geq$ 1ms, which results in a mean counts per data point of $N_\tau = \frac{\tau}{1\text{ms}} N_0$. For each of the new data sets the standard deviation $\sigma_\tau^{\text{total}}$ was calculated, as well as the expected shot noise $\sigma_\tau^{\text{shot}} = \sqrt{N_\tau}$. The ratio $\sigma_\tau^{\text{total}}/\sigma_\tau^{\text{shot}}$ versus N_τ is then plotted.

The dots in Fig. 3.2 are values derived from the inset noise trace, the red curve is a simulation according to the formula

$$\sigma_\tau^{\text{total}}/\sigma_\tau^{\text{shot}} = \frac{\sqrt{{\sigma_\tau^{\text{shot}}}^2 + {\sigma_\tau^{\text{laser}}}^2}}{\sigma_\tau^{\text{shot}}} = \frac{\sqrt{N_\tau + (\kappa_1 N_\tau^{\kappa_2})^2}}{\sqrt{N_\tau}} \ . \tag{3.1}$$

To match the measured data, κ_1 was set to 0.013 and κ_2 to 0.925. A heuristic assumption of a linear dependence with κ_1=0.004 and κ_2=1 deviates slightly in slope for higher N_τ. Below $45 \cdot 10^3$ counts per data point, the noise is governed by shot noise, and above this value the relative noise stays constant at roughly 0.4 % of the count rate. An important consequence is that with this detection system, the sensitivity is limited to a 0.4 % signal.

Note that the curves reach below one for small N_τ, despite the fact that poissonian light source cannot beat the shot noise limit. Probably an offset in the synchronization of APD counting module and the analog input of the measurement computer caused a moving average effect during the measurement of the noise trace.

Polarization Control

For most experiments, a near to perfect linear polarization is desirable, because all polarization components that are perpendicular to the molecular dipole moment will not interact with the molecule and therefore add to a background level including the associated noise. Furthermore, the polarization of the excitation beam has to be freely selectable to be aligned with the randomly oriented but fixed dipole moment of the molecule under study. On the other hand, all dielectric mirrors, beam splitters and interfaces in the setup exhibit a different transmission or reflection for the s- or p-polarization components. However, the effect of each optical element in the beam path can be described by so-called Jones matrices. The effect of the complete setup between the fiber output and the position of the sample in the cryostat can be calculated as a product of each element's transfer matrix, which results in a cumulative phase retardation at an average orientation. A broadband variable waveplate, called Berek compensator (`New Focus 5540`), was set up to annul the cumulative polarization influence of the optical setup, in other words, to exhibit an exactly inverse retardation. After this addition, a linear polarizion of the excitation light, independent of its main polarization axis and with an ellipticity of only 0.3 to 1 percent measured on PD1, could be reproducibly achieved. This

presented a limit, probably because the local structure of the tetradecane sample introduced some amount of depolarization when the sample thickness was too large.

Galvanometric mirrors and telecentric

To laterally scan the laser focus across the sample, a system of galvanometric mirrors and a telecentric lens is used. The galvanometric mirrors are two 1cm large silver mirrors that are attached to two orthogonal rotation axes, 1 cm apart. The galvonometric mirrors are placed in the focal plane of the first telecentric lens, which therefore translates an angle deflection by the galvos to a parallel beam displacement between the telecentric lenses. The second lens is placed two focal lengths of the first lens, and converts the beam displacement again to a beam tilt. Finally, the microscope objective in the cryostat is positioned approximately such that its backfocal plane coincides with the focal plane of the second telecentric lens. This way the whole assembly virtually places the galvonometric beam tilt to the backfocal plane of the microscope objective. By moving the galvanometric mirrors, the focus is then laterally moved across the sample. The stepsize is given by the angular resolution of the electrically driven galvos and the magnification of the cryogenic microscope. It was calibrated for our setup to be 4.6 nm.

3.2 Detectors

3.2.1 Avalanche photodiodes

The detectors mostly used for both extinction and fluorescence measurements were actively quenched, single photon counting, silicon avalanche photodiodes (`Perkin-Elmer` SPCM-AQR-14). These detectors have a photon detection efficiency of up to 65 % in the wavelength range of interest for us, i.e. 580-650 nm. Also, the number of dark counts is very low, on the order of 50-150 counts per second. These detectors are commonly used for applications that need high quantum efficiency, such as quantum cryptography [96] and single emitter spectroscopy (see e.g. [97]), and have therefore been characterized and optimized extensively [98, 99].

In an avalanche photodiode detector (APD) a reverse bias voltage is applied across the diode's *pn*-junction to create a depletion region. Electron-hole-pairs can be created by absorption of a suitable photon or by thermal generation (giving rise to a dark count) in that region. The carriers are accelerated towards the respective electrodes and multiplied by repeated impact ionizations, which creates an avalanche effect. Each absorbed photon can result in several hundred to thousands of electrons that can be registered with high certainty. To prevent burning the device and to arm it for the arrival of the next photon, this avalanche should be quenched as soon as its onset can be detected. This can be done passively by placing a large resistor in series with the diode [100]. However, in this configuration, the time needed to recharge the bias voltage, i.e. the detector dead time, can be as large as several microseconds [98]. A shorter dead time can be achieved by actively quenching the avalanche with an electronic sensing circuit that lowers the bias voltage and reapplies it 30-50ns after the leading edge of an avalanche is detected [101].

Timing Performance

The depletion region in `Perkin Elmer` SPCM-AQR detectors is roughly 30 μm thick and the device is 175 μm in diameter. This relatively large volume gives rise to a timing uncertainty in the detection of avalanches originating in different locations of the device (transit time spread or TTS). Strong focusing of the light into the center of the active area decreases the TTS by up to 25 % [98]. An additional timing uncertainty is introduced by amplifiers and the quenching circuit [98]. Also reported are shifts of the photon detection time with increasing count rates [99, 102], which is due to the reacharging time for the bias voltage. Furthermore, a so-called diffusion tail [103], which gives rise to avalanche detection events several tens of nanoseconds after the photon absorption incident, can seriously degrade the timing performance. This diffusion tail is caused by the generation of carriers outside the depletion region which slowly drift into the active region and trigger an avalanche long after the photon hit the detector. This diffusion tail is wavelength dependent [103] and depends strongly on how well the light is focused onto the active area [97].

The timing uncertainty of the `SPCM`-APD modules does not present any problems as long as extinction or fluorescence excitation spectra are examined in a steady state measurement. However, for experiments where the photon arrival time is vital, e.g. for autocorrelation or lifetime measurements, this uncertainty has to be characterized. To quantify the TTS of the detectors used for the autocorrelation measurements shown in chapter 6, the instrument response function or prompt function was measured in a start-stop experiment. A picosecond laser with 75 MHz repetition rate (`Time Bandwidth GE-100-XHP`) was strongly attenuated, split and directed both onto a `New Focus` Model 1601 high-speed photoreceiver and the APD under study. The signals were fed into a `Becker & Hickl` SPC-130 time correlated single photon counting module. The histogram of start-stop time intervals shows the uncertainty in the determination of the true photon arrival time, which should be as small as possible for the measurement of autocorrelation functions. Figure 3.3 shows the results for two APDs, **5713 Rev F** and **5343 Rev F** for three different average count rates, and tab.(3.1) summarizes the measured TTS FWHM. The time axis resolution for these measurements was fairly low, around 200ps per pixel. Nonetheless, the results suggest a strong photon timing uncertainty, especially for spectrally broad signals of high, fluctuating count rates. Also, the particular shape of the instrument response function could be recovered. In chapter 6, I will discuss the implications of this for single molecule autocorrelation measurements in more detail.

	70 kHz	1 MHz	2.4 MHz	max. shift
5713 Rev F	550 ps	620 ps	750 ps	1.2 ns
5343 Rev F	600 ps	900 ps	1050 ps	1.4 ns

Table 3.1: FWHM of the instrument response function for two APDs used in the experiments, measured with a 15ps, 532 nm laser. The width of the response growths with countrate and shifts by *max. shift* when the countrate is increased from 70 kHz to 2.4 MHz.

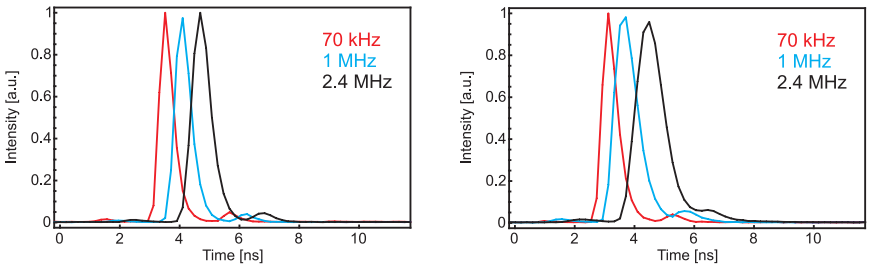

(a) APD 5713 Rev F (b) APD 5343 Rev F

Figure 3.3: Instrument response function for two APDs used in the setup. Excitation light was a 532 nm, 15 ps laser. Both APDs show a count rate dependent TTS and a shift of the total response function with increasing countrate. The afterpulses are probably a result of reflexions in the BNC cables. Table 3.1 summarizes the FWHM derived from this plot.

Detector dead time

The detector dead time is necessary to recharge the bias voltage across the *pn*-junction of the photodiode after a photon counting event. The active quenching circuit decreases this time to 35-60ns [98, 104] during which the APD can not detect any photons. One result is that at high count rates a certain fraction of photons arrives during the dead time and is missed, therefore reducing the determined count rate. A correction factor cf has to be introduced for a given dead time t_d and measured count rate c_R as given by [104],

$$\mathrm{cf} = \frac{1}{1 - \mathrm{t_d c_R}} \ . \tag{3.2}$$

This correction factor is important when quantitative results are to be obtained at high count rates, as is the case for extinction measurements. The correction factor for the used "extinction"-APD **5267 Rev F** was determined several times during different experiments, and Fig. 3.4 shows a typical example. To measure the correction factor, the countrate on the APD behind a strong ND filter was compared to the output of a low sensitivity, linear photodiode for several different intensities. Alternatively, a triggered measurement of the output pulses in a long persistence mode of a digital oscilloscope can directly visualize the dead-time of the APDs. Such a trace is shown as an inset of Fig. 3.4. It yields the same dead time of 45-50 ns as the comparison with a linear photo diode.

Breakdown flash

The detection process in an APD gives rise to faint light emission, the so-called breakdown flash. This light emission can be a problem in quantum cryptography protocols, and the timing as well as spectral properties of the emission have been studied in detail [105]. For second-order correlation measurements of a single

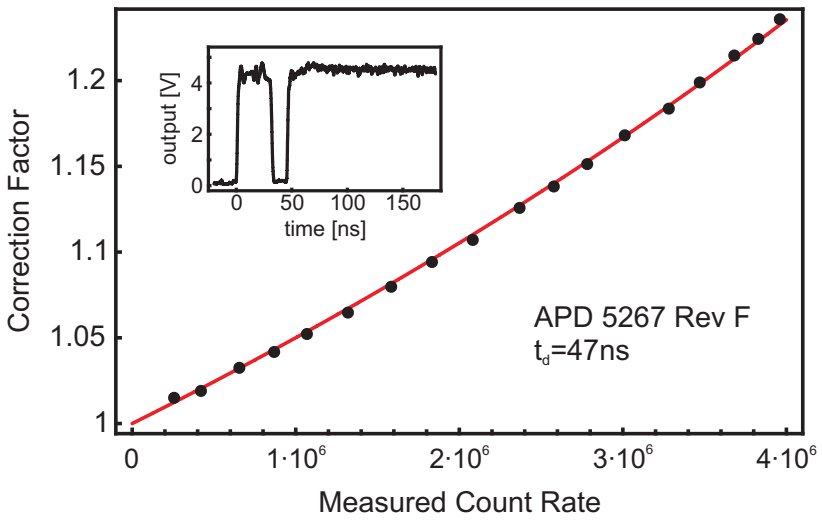

Figure 3.4: Correction factor cf versus measured countrate determined for the "extinction"-APD 5267 Rev F. A fit with Eq. (3.2) yields a dead time t_d of 47 ns.

molecule (see chapter 6), a beamsplitter directs the emission of a molecule onto two APDs. One has to be careful not to allow any cross-talk between the two detectors, otherwise the breakdown flash can cause artefacts in the correlation function. Figure 3.5 shows an example of this, when two APDs behind a 50/50 beamsplitter are illuminated with coherent laser light. The two features are the time evolution of the breakdown flash of one detector as seen by the other, and vice versa. A simple measure against this artefact is to place a 700 nm optical short pass filter (`Omega Optical`) in front of one of the detectors, which blocks almost all of the breakdown flash emission [105].

3.2.2 CCD camera

A serious alternative to APDs is the use of charge coupled device (CCD) cameras. For some angle dependent extinction measurements, a back-illuminated electron multiplying CCD [106], the `Andor` iXon DU-860 was used. This device features a 128x128 pixel back-thinned silicon-CCD chip, with a pixel size of 24 μm (CCD60 sensor from `e2v`). The quantum efficiency of such a chip reaches 92.5 % in the visible. However, the readout process in which the whole charge distribution (i.e. the image) is first shifted vertically into a storage array of the same size as the image array, and then line by line through a charge to voltage conversion, generates up to 50 additional detected electrons per pixel, depending on the readout speed. The electron multiplying (EM) CCD amplifies the photo-generated electrons in each pixel during the readout process by a factor of up to 1000. This is accomplished in an additional multiplication register via repeated impact ionization before the actual charge to voltage conversion. This results in true single photon sensitivity at full

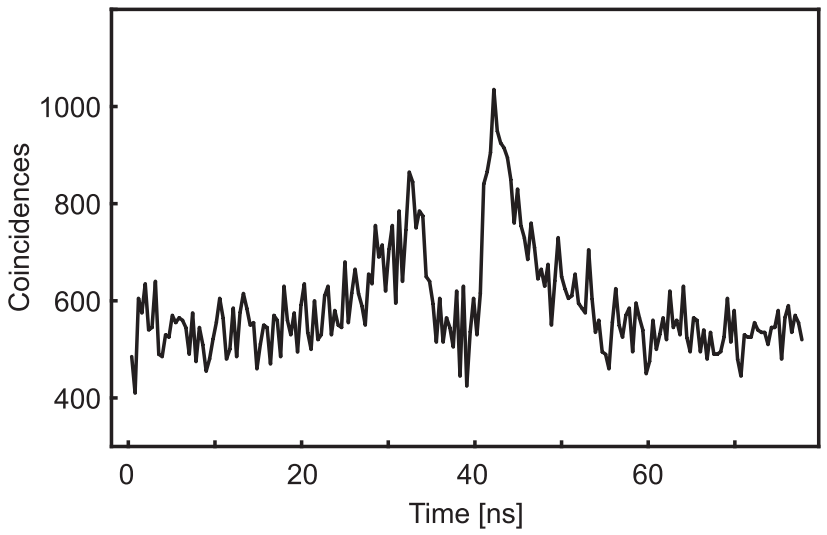

Figure 3.5: Second-order correlation function of attenuated laser light measured with a HBT setup. The breakdown flash of the two APDs gives rise to the feature in the center, explained in [105]. A 700 nm optical short pass filter eliminates this artefact.

readout speed. Furthermore, the sensor is cooled to -80°C to minimize thermally generated dark counts.

This camera proved advantageous for imaging light extinction by single molecules, especially due to its high dynamic range of 16 Bit (2^{16} shades of grey) and low dark count noise. The full image readout speed is 500 frames per second, which was usually not exploited. The camera could be triggered at each laser frequency pixel, and later several camera images that corresponded to the same excitation frequency averaged to further reduce the noise. For most measurements, however, a 128x128 pixel image was not necessary and despite comparable performance to APDs, the camera was used only for specialized experiments.

3.3 Solid immersion microscope

3.3.1 Aspheric lenses

Aspheric lenses were employed for focusing and collimation of the laser light. Unlike conventional lenses with spherical surfaces which are formed by grinding, aspheric lenses are fabricated by molding glass or a polymer into a predetermined form that eliminates any spherical aberrations. The optimal surface curvature is calculated for a specific application at a certain design wavelength, and has to take into account the dispersion of the lens medium, the coefficient of thermal expansion and the change of refractive index with temperature. The production of aspheric lenses is low-cost compared to aberration free multi-element systems. The main application of these lenses is in fiber coupling and consumer electronics and optics. For

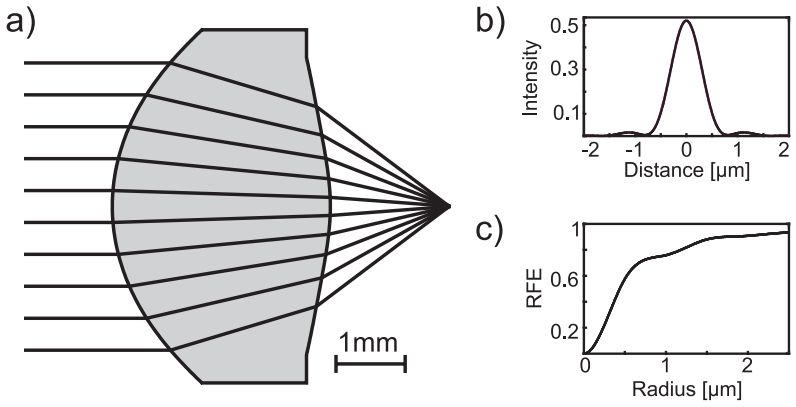

Figure 3.6: The aspheric lens `Lightpath 350330` used for focusing and recollimation of the excitation laser light. a) shows a sideview and ten rays of 590 nm traced through the system, b) is the PSF at the focus, revealing a FWHM of 680 nm, and c) the encircled energy (**R**adial **F**ractional of **E**nergy). For explanations see the text.

low temperature applications it is important that a single lens can have diffraction limited performance similar to delicate multi-element spherical systems.

The lenses that were used in this experiment were `Thorlabs` C330TM-A, produced by `Lightpath Technologies` Lens Code 350330. They have a specified numerical aperture of 0.68, effective focal length of 3.1 mm and a working distance of 1.76 mm, the clear aperture is 5 mm. The lenses are made from `Corning` C0550 glass with an index of refraction around 1.6. The design wavelength for this lens is 830 nm, which is suboptimal for the used excitation wavelength of 590 nm. The reason to work with this lens nonetheless is first, that it offered a good combination of high N.A. and long working distance (needed for the addition of a solid immersion lens), and second, that most commercially available aspheres have either a long design wavelength (diode laser collimation), or are designed to focus through a transparent layer (CD/DVD). At the time of setting up the experiment, the `C330TM` lens seemed to be the best compromise for the proposed setup.

wavelength	radial distrib.	EFL	WD	Strehl ratio	FWHM
830 nm	top-hat	3.09 mm	1.77 mm	0.96	680 nm
830 nm	3 mm gaussian	”	”	0.95	820 nm
590 nm	top-hat	3.05 mm	1.73 mm	0.29	611 nm
590 nm	3 mm gaussian	”	”	0.52	680 nm

Table 3.2: Performance of the aspherical lens `350330` from `Lightpath Technologies`. Shown is the effective focal length, working distance, Strehl ratio and FWHM of the PSF as obtained by the `OSLO` optical design program. This was calculated for two wavelengths and two radial intensity distributions of the input beam.

The specifications and performance of the lenses was checked with the OSLO Optics Software for Layout and Optimization from Sinclair Optics. Both aspheric surfaces of the lens were modelled according to the aspheric coefficients provided by the supplier, and a laser beam with either 830 nm or 590 nm as well as different radial intensity distributions was ray-traced through the system. The point-spread-function (PSF) is obtained from OSLO by a combination of geometrical and physical optics. Details of how OSLO obtains spread functions is given in [107].

Table (3.2) shows the focusing properties extracted from the simulation. Clearly the performance of the lens is diffraction limited for the design wavelength of 830 nm. A lens system is called diffraction limited if the Strehl ratio, which compares the maximum of the attained point spread function to the corresponding value of an aberration free lens, exceeds 0.8 (see e.g. [108]). The company-specified values for the effective focal length (EFL) and working distance (WD) are also recovered from the simulation. A top-hat radial intensity distribution of the input beam yields a smaller FWHM of the focus than the measured 3 mm $1/e^2$ gaussian beam that was used in the experiment. It is always advantageous to overfill a focusing lens in order to exploit the full NA, but for the experiments described here, a high transmission of an input laser beam was desirable. A top-hat distribution inevitably results in a high loss of excitation light at the entrance aperture. For 590 nm wavelength the situation is different. Since the lens curvature is optimized for 830 nm, especially rays with a larger distance from the optical axis will no longer be accurately focused. The Strehl ratio is decreased to 0.52 for a gaussian beam, and is even lower for a top-hat beam. Figure 3.6 b) shows the PSF versus lateral radial distance from the focus for a 590 nm, 3 mm gaussian beam.

3.3.2 Solid immersion lens

The solid immersion microscope was first introduced by Mansfield and Kino in 1990 [109, 110]. A very similar concept based on the use of immersion oil was published in 1990 by Guerra [111]. Both cases exploit the fact that inside a material with refractive index n the wavelength of light is reduced to $1/n$ of the vacuum value, which correspondingly also reduces the diffraction limit by the same factor. A solid immersion lens (SIL) can easily have a refractive index of 2 and more [112], and is also suitable for cryogenic conditions. It can be used as an addition to a conventional microscope and is placed between the objective lens and the sample surface. If a hemispherical SIL is used, the light rays from the objective hit the round side of the SIL perpendicularly, and the beam path will not be altered. There are two different scenarios of how a SIL can help to increase the interaction of incident light and the solid-state emitter under study. The first, which is especially important for quantum dot spectroscopy [17, 18, 113], is that an index-matched SIL in the excitation path can regain the angle of illumination offered by the focusing lens, which is usually limited by refraction at the otherwise planar sample surface[1]. On the other hand, the host crystal in single molecule spectroscopy has a refractive index of approximately 1.5 and a SIL with a higher index can be used to create a strong focus at the interface, with the molecule embedded in a lower index medium

[1]GaAs with n≈3.5 limits this angle to 17° at 960 nm [18].

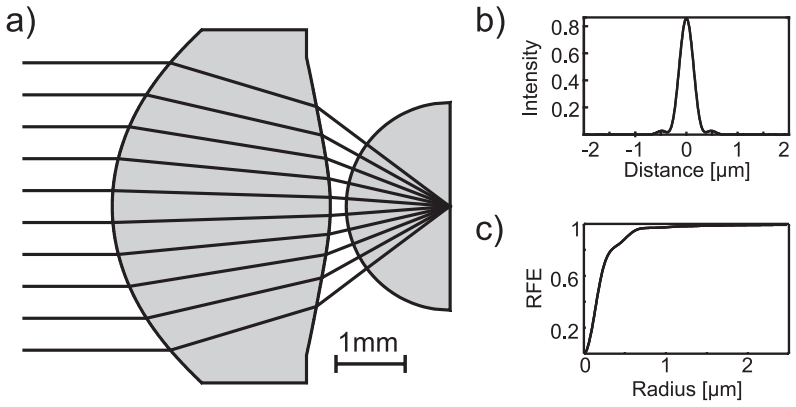

Figure 3.7: Combination of aspheric lens `Lightpath 350330` and cubic circonia solid immersion lens. a) shows a sideview and ten rays traced through the system, b) is the PSF at the focus, and c) the encircled energy (**R**adial **F**ractional of **E**nergy). For explanations see the text.

close to this interface. In this sense, SIL microscopy is essentially a near-field method [114].

A different approach is the so-called super-hemispherical, or Weierstrass SIL [114, 115, 116], a ball lens truncated at the inner aplanatic point [117]. As a result, this SIL is a refractive element, which will change the actual "geometrical" NA of the system and reduce the focal spot to $1/n^2$ of its value in vacuum. On the other hand, also the field of view is reduced by $1/n^2$, and other allowances are stricter for a Weierstrass lens. I will describe in this section only the hemispherical lens that was used for all experiments within this work.

Fig. 3.7 shows a raytrace, point spread function and radial fractional energy for the combination of Lightpath 350330 asphere and the cubic circonia solid immersion lens that was used for the experiments, for 590 nm excitation light and 3 mm gaussian input beam. The point spread function shows a tighter focussing of the incident light, and the FWHM is 315 nm, roughly a factor 2.18 smaller than for the asphere alone, see Fig. 3.6. Furthermore, the addition of the solid immersion lens increases the Strehl ratio to 0.88, which for the asphere alone was only 0.52.

3.3.3 Properties and aberrations of a solid immersion microscope

A hemispherical SIL surface will, provided a perfect on-axis positioning and illumination, not alter the beam path of the illumination light. In this case, all rays intersect the interface between air and high-index SIL material under normal incidence. If, however, the SIL is not perfectly aligned, or the illumination is off-axis, the SIL will introduce aberrations and impair the focus quality. The effects of misalignment and fabrication errors were studied in detail in the PhD thesis of Mansfield [110] and in work by Baba et al. [118]. Here I will introduce the two most important cases. For the simulations with `OSLO`, I inserted parameters that we used in our experiments,

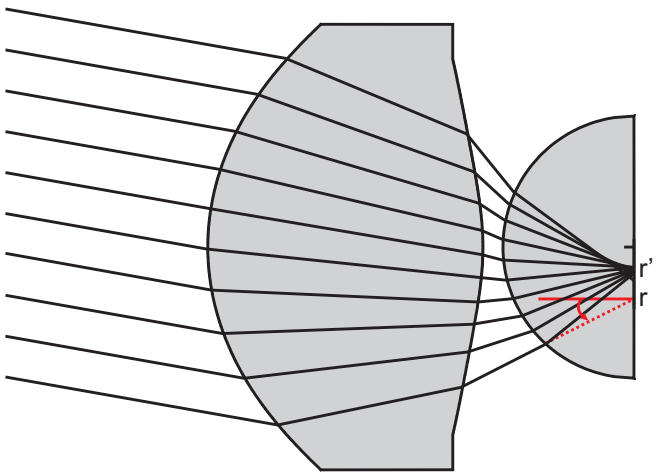

Figure 3.8: Field of view reduction in solid immersion microscopy. In this raytrace the input beam is rotated by 10 degrees. The introduction of a spherical interface diffracts the beam and shifts the focal from a point r to a point r', where to first order $r' = \frac{1}{n}r$. The red dotted line shows the lowest ray in absence of the SIL. The angle θ from EQ. (3.3) is the angle under which the ray would have intersected the normal to the focal plane without the SIL in place and is denoted by the red arrow next to the point r.

i.e. the asphere Lightpath 350330, a solid immersion lens with radius a=1.5 mm and refractive index n=2.18, a gaussian input beam with λ=590 nm and $1/e^2$ diameter of 3 mm.

Magnification, field of view

First, the effect of a SIL on either off-axis illumination or imaging will be discussed. This can be encountered when imaging extended objects that are located at a distance from the optical axis, or when the excitation beam is scanned across the sample. A similar effect is a lateral displacement of the SIL from the optical axis, for example through non optimal alignment. In these cases the rays no longer intersect the SIL perpendicularly and will be diffracted at the spherical interface. Mansfield derived an equation for the lateral displacement r' of a ray that would have hit the focal plane at r under an angle θ without the SIL. See Fig. 3.8 and [110] for explanations of the parameters used here.

$$r' = \frac{r}{n} + \frac{r^2}{na}\left(1 - \frac{1}{n}\right)\sin(\theta) + O(r^3) \ , \tag{3.3}$$

where n is the refractive index of the SIL, and a is its radius. This equation is valid for any angle θ, its derivation involves quite some trigonometry and approximations for small shifts. The equation shows that, in first approximation, the presence of the SIL shifts the focus from r to a spot $\frac{r}{n}$, which is equivalent to a magnification by

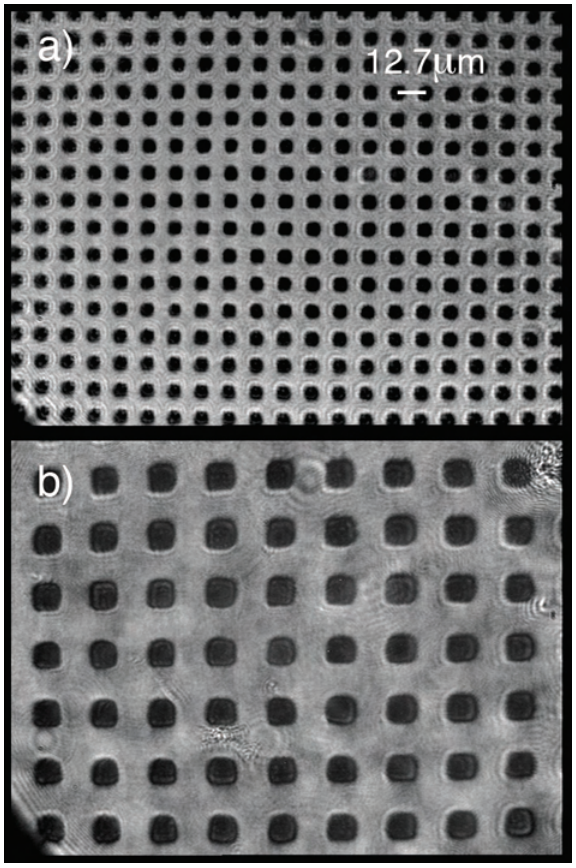

Figure 3.9: Magnification in a solid immersion lens microscope. The top shows a camera image of a 2000 lines per inch aluminum calibration sample, recorded with just a C330TM aspheric lens as an objective. The bottom image shows the same sample after addition of the cubic circonia solid immersion lens. The magnification is increased exactly by a factor of 2.18, the refractive index of the SIL material. The field of view is decreased accordingly.

a factor of n. The raytrace in Fig. 3.8 recoveres this shift exactly. The second term is dependent on θ, and can be interpreted as a wavefront curvature at the focus. One can clearly see a reduction in focus quality in Fig. 3.8, which is exaggerated by the large input angle. With the convention that this curvature should not be larger than $\lambda/4$ in order to call the focus unaberrated, one can calculate the maximum r' where this condition is met, or the field of view (FOV) for a given maximum $\theta_{\max}$ which in our case is ArcSin(0.68), see [110, 118].

$$2r' \leq \left(\frac{2a\lambda}{n(n-1)\sin(\theta_{\max})} \right)^{1/2} . \tag{3.4}$$

For our experimental setup, the FOV which meets the $\lambda/4$-condition is about 30μm in diameter. Fig. 3.9 shows two images of the 12.7 μm square calibration grid explained in the next subsection. Figure 3.9 a) was taken with just the asphere Lightpath 350330 as an objective, whereas Fig. 3.9 b) was taken through SIL and

asphere. The magnification is increased exactly by a factor 2.18. The unaberrated FOV is already sub-ideal in a), and should be decreased to 30 μm in b). This is, however, more pronounced in the calibration scans explained in the next subsection. Here, an incoherent white light source coupled out of a multimode fiber was used for illumination. The light source is not single mode, and introduces additional aberrations towards the edges of the image.

Refractive index mismatch

The main applications of SIL microscopy lie in semiconductor spectroscopy [119] and optical data storage [115, 120, 121]. In these cases care is taken to match the indexes of SIL and substrate, and only a small (air)-gap has to be taken into account. Correspondingly, the situation of non-matched interfaces is not covered often in the literature.

The focus evolution after traversing the interface into an optically thinner medium is studied in [114, 122]. In [114] a full vector electromagnetic field model was used to model the focal spot intensity distribution at the interface of a n=1.845 super-hemispherical SIL to air. One of the findings is that the focus is elliptically shaped, and that the FWHM in direction of the polarization vector increases by 30 % when entering the low index medium. In the setup described in [114], the super-hemispherical SIL in combination with a NA=0.55 objective results in large parts of the light being totally internally reflected. In our case, the sample consists of n-tetradecane, which has a refractive index of 1.43 [123], and all of the focused light will be transmitted into this medium[2]. However, we can assume that molecules very close to the SIL-sample interface are not spectrally stable, as our own observations in thin film samples have shown, and was studied for terrylene close to hexadecane-glass interfaces [124]. The search for stable molecules leads us to choose molecules which have at least a distance of 100 nm from the interface. No detailed numerical analysis can be given here, however, it is fair to assume an increase in the focal spot FWHM compared to the diffraction limited value in the SIL medium.

3.4 System calibration and performance

Calibration

A periodic array of aluminum squares was used to calibrate the step size of the galvanometric mirrors. The squares had a thickness of 100-200 nm and were evaporated onto the flat side of a cleaned solid immersion lens using a 2000-mesh Nickel square grid (`Plano G249N`, manufactured by `Agar Scientific`) which are available as TEM magnification test objects. These grids have 2000 lines per inch, corresponding to a lattice spacing of 12.7 μm. Figure 3.10(a) shows a roughly 100x100 μm LSM calibration scan of the aluminum squares, which yielded a Galvo step size of 4.6 nm. The image was taken with the cryostat warm and open, which does not

[2]Total internal reflection happens at the interface of coverslip to vacuum.

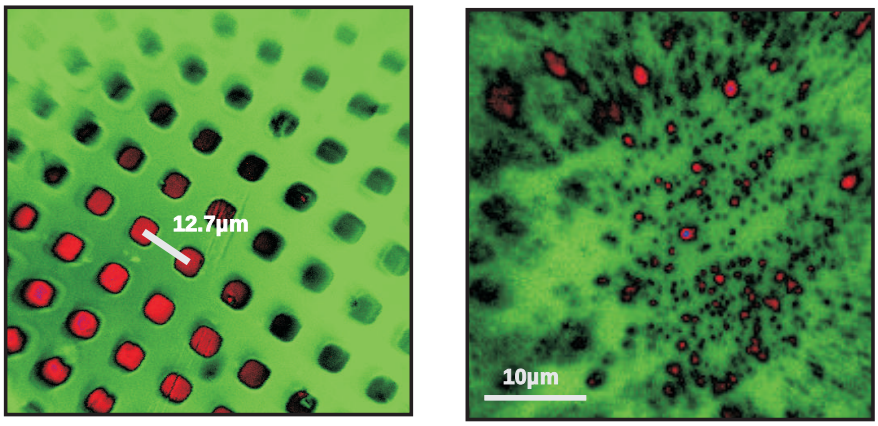

(a) LSM calibration (b) Imaging quality

Figure 3.10: Confocal scans to calibrate the LSM stepsize and monitor the imaging quality of the asphere-SIL system. a) shows a 100 × 100 μm scan of the calibration sample in the warm and open cryostat: `08MayScan007`. The calibration yielded a stepsize of 4.6 nm. Picture b) is a 40 x 40 μm scan of 100 nm beads in the cryostat.

change the result of the experiment compared to the usual running conditions. The laser was kept at a fixed wavelength around 590 nm, and the backreflected intensity recorded on an APD. Clearly visible is a deterioration of the image quality for distances more than about 15 μm from a central spot. This is due to the off-axis aberrations of a solid-immersion microscope system as explained in section 3.5. Both the focal spot quality and the detection efficiency are drastically reduced when the laser beam does not hit the solid immersion lens on-axis.

A second image, Fig. 3.10(b), taken at a different time, shows the same small FOV when looking at 100 nm fluorescent latex beads (`Molecular Probes`). In order to obtain a high quality small focal spot and high detection efficiency, one is required to work within about 10 μm of the center position of the SIL.

Minimal focus size

A rough estimate of the possible diffraction-limited spot size using an asphere with N.A.=0.68 SIL with n=2.18 gives a value of 240 nm for a 590 nm illumination. Figure 3.11 shows an `OSLO` simulation for the actual parameters that we used in the experiment, including the deviation from the design wavelength, and the gaussian input beam distribution. The top shows the FWHM of the central peak of the PSF for the asphere alone (green dots), and for the asphere-SIL combination (red dots) as a function of asphere displacement from the focussed position. The intensity at the center will reach a maximum in the "diffraction focus" position. For the asphere alone, the simulations yield a focal spot FWHM of roughly 680 nm. In combination with the SIL this decreases to 315 nm, nearly an exact factor of 2.18 smaller. In addition, the SIL increases the Strehl ratio of the system. At the bottom of Fig. 3.11

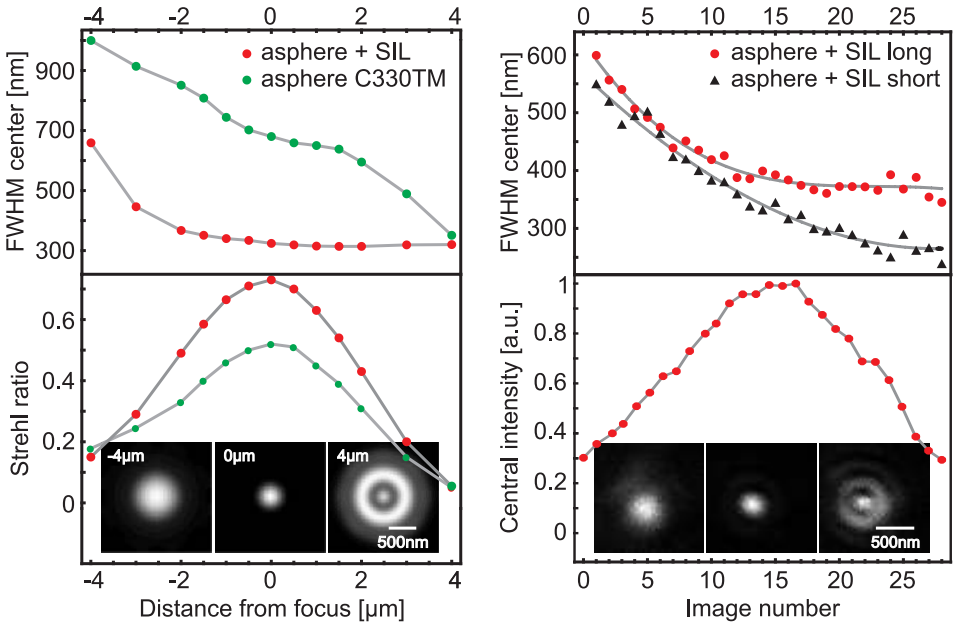

Figure 3.11: Focal spot size of the SIL objective. The left graphs show the FWHM and the intensity (in terms of Strehl ratio) of the central peak of the point spread function, as resulting from OSLO simulations with 590 nm and a $1/e^2$=3 mm gaussian input beam. The green symbols are for the aspheric lens alone, the red symbols for asphere and SIL. The right side is the measured FWHM and intensity maximum for the asphere-SIL combination, measured by scanning the incident laser beam across fluorescent beads attached to the flat side of the SIL. Sample mounted in the cryostat, however at room temperature. For details see the text.

a) three normalized density plots of the focus are shown for displacements of the asphere from the focussed position of 4, 0 and -4μm, where a negative sign designates a too large distance between the lens and SIL.

The right side, Fig. 3.11 b) shows the focus FWHM as measured on a 100 nm fluorescent bead, placed on the flat side of the SIL. This measurement was repeated for several beads and later single molecules and yielded comparable results. The illumination laser was moved via galvo mirror scanning across the sample, and the red fluorescence of the bead was collected via the same objective and recorded on an APD. In between different scans, the asphere was moved closer to the SIL by several steps of the on-axis piezo slider (see cryostat insets). The bead itself stayed fixed in space. Although the changing illumination focus also results in a changing detection efficiency of the beads fluorescence, the bead-APD system can be regarded as a point like detector of the illumination laser focus, given the small displacements shown here. Each bead contains hundreds of dye molecules with random orientations, which renders the bead a polarization-insensitive detector for the total field magnitude at a given point. Since the piezo slider steps are not calibrated, any comparison with the simulations shown in Fig. 3.11 a) can at best be qualitative. One observation is that

the focal spot intensity distribution behaves as expected from the simulations, with a smeared out distribution for larger, and a ring structure for smaller distances. This picture is consistent with the reflected image of the focus, recorded on a camera in the backward direction[3]. The focus itself appears slightly elliptical, which probably is a result of the linear input polarization [114], a point that is not taken into account for the simulations. The measured FWHM along the long axis is -at the point of highest central peak intensity- 360 nm, along the short axis 315 nm. After deconvolution with the bead size of 100 nm this yields values of 345 nm and 300 nm, respectively. This result is close to the simulated values. The difference might be due to improper alignment of the system and the incident laser beam or imperfections in the SIL shape.

In order to achieve diffraction limited performance at the desired wavelength of 590 nm, the aspheres should be replaced with lenses of a matching design wavelength. However, for the experiments conducted in the scope of this thesis, a focal spot size of little more than 350 nm was sufficient.

System transmission

In an ideal extinction measurement, one has to make sure to capture 100 % of the incident laser light on the detector. In this case the extinction signal has a negative Lorentzian line shape, and directly gives a number for the efficiency of light-matter interaction achieved. However, the laser light transmission trough the cryostat including both aspheres and a SIL/sample/coverslip combination amounted to only 25 %, as measured with a powermeter. A large portion of the incident light is lost at the eight cryostat windows, as well as other surfaces hit under normal incidence. The windows have a transmission of ≈ 0.8, the round side of the SIL gives rise to $\frac{(n-1)^2}{(n+1)^2}$=13.8 % reflection, and $T_{\mathrm{SIL}} = 0.862$ transmission. The same factor T_{SIL} applies for the transition from cubic circonia to air for all angles somewhat below the critical angle.

The sample geometry results in an additional loss of excitation light. The laser is focused into the high refractive index SIL, and transmitted through two flat interfaces, the first from cubic zirconia to the cover slip (BK7 glass) and then into vacuum. The effect of the two interfaces can be simplified as one interface from

[3]Karrai et al. [114] describe a discrepancy between the reflected image and the actual focal distribution, which was mainly a result of the large amount of total internal reflection in their setup. See also [122].

configuration	output power in mW	transmission coefficient
2 aspheres	3.8	0.95
2 aspheres + SIL left	1.5	0.375
2 aspheres + SIL right	2.6	0.65
2 apsheres + Hamburger	2.7	0.675

Table 3.3: Transmission of a 3 mm gaussian beam through different arrangements of aspheres and cubic circonia solid immersion lenses. The input power was 4mW, all measurements have been done at room temperature outside the cryostat.

n_1=2.18 to n_3=1, and the angle of incident light (in terms of an "incident N.A.") that will be recollimated with a lens of $\mathrm{NA_{out}}$=0.68 can be calculated from Snell's law according to

$$\mathrm{NA_{in}} = \frac{\mathrm{n_3}}{\mathrm{n_1}}\mathrm{NA_{out}} \approx 0.31 \ . \tag{3.5}$$

A ray trace can give a good estimate of what the maximum distance of a "critical ray" from the optical axis can be so that it still will be transmitted through the system. Figure 3.12 shows the geometrical arrangement of focusing and recollimation lens, as well as SIL and cover slip. Also shown are the input rays that are just transmitted through the system, and the portion of the input light that lies within these rays. The Gaussian function on the left side depicts the intensity distribution in the incident laser beam with $1/e^2$ diameter of 3 mm. The recollimation of input light is not perfect for the high angles, owing to the deviation from the design wavelength. This figure shows that 80 % of the incident light will be recollimated, giving a $T_{\mathrm{recoll}} = 0.8$. Finally, the aspheres have a measured transmission of T_{aspheres}=0.95.

The total transmission coefficient is the product of all components

$$T = T_{\mathrm{windows}} \cdot T_{\mathrm{aspheres}} \cdot T_{\mathrm{SIL}} \cdot T_{\mathrm{SIL}} \cdot T_{\mathrm{recoll}} \approx 0.45 \ . \tag{3.6}$$

The deviation from the measured 25 % can have several reasons: scattering of power out of the beam by sample structures, additional window absorption, etc. For the sake of an unambiguous determination of the interaction efficiency between molecule and light field, it would be desirable to enhance the transmission through the optical system. One way is to use a matching refractive index at the collimation

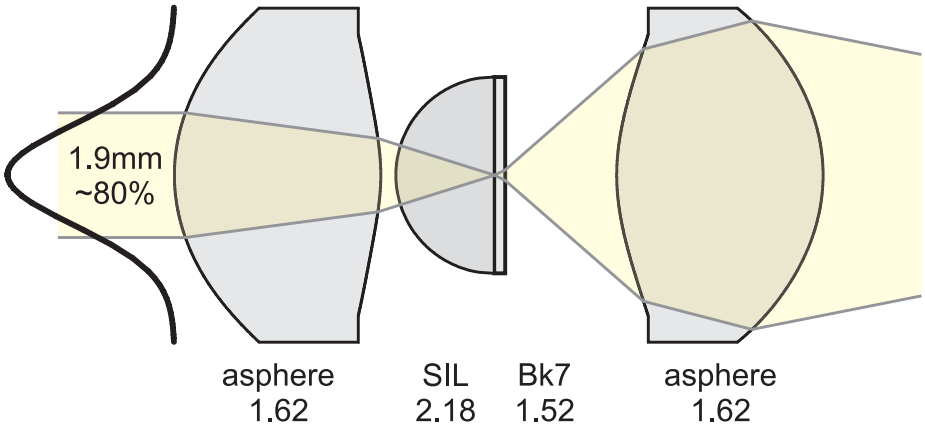

Figure 3.12: Transmission of laser light through the interfaces of the optical system. Only the inner part of the excitation beam, shown in yellow shading will be recollimated by the second asphere after being refracted at the interfaces of SIL to BK7 glass and glass to vacuum. Roughly 80 % of the incident light lies within the "critical rays".

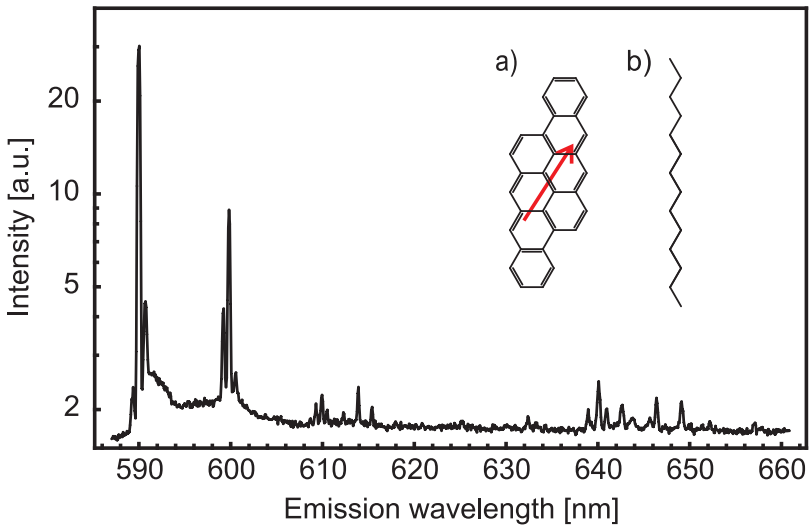

Figure 3.13: Single-molecule emission spectrum of DBATT in *n*-tetradecane under 0-1 excitation. Recorded on a grating spectrometer with 0.1 nm resolution and shown on a logarithmic scale. Inset: a) Structural formula of the subject under study, DBATT. Also shown is the direction of the transition dipole moment. b) is the host matrix molecule, *n*-tetradecane. Courtesy of Robert Lettow.

side of the setup, in other words a "hamburger" of two solid immersion lenses. The use of index matched SILs, i.e. with $n_{\mathrm{SIL}} = n_{\mathrm{tetradecane}}$ would get rid of unwanted total internal refraction, and provide a system most close to an emitter in free space, however, at the cost of focus size. In addition, all interfaces should in principle be anti-reflection coated, which could even be an option for the SIL.

The total transmission through the optical system was measured outside of the cryostat for different arrangements. Just for the two aspheres, for one SIL, the same SIL flipped, as well as a "hamburger" consisting of two solid immersion lenses whose flat sides touch. Tab.(3.3) summarizes the results of these measurements.

3.5 Sample

The sample has to be prepared on the flat side of the hemispherical solid immersion lens with a surface diameter of only 3 mm. The SIL material is cubic circonia which has different surface physical properties than a glass cover slip, but experience has shown that the sample preparation is not largely affected by this substrate.

For all of the experiments discussed in this thesis, the sample was DBATT in *n*-tetradecane. This system, and other combinations of DBATT with *n*-alcanes have been extensively studied at Leiden University [25, 34, 125]. See the theory chapter for a more detailed discussion on the Shpol'skii effect and the photophysical properties of DBATT.

DBATT has several favourable properties for our experiments, namely a large fluorescence quantum yield of Φ_{fl}=0.8 [125], a strong zero-phonon line [22], and a small triplet-population [25], all of which yield a large extinction cross section. The choice for *n*-tetradecane was made because this matrix seems to introduce less crystal defects than the longer *n*-hexadecane [25]. Figure 3.13 shows an emission spectrum of DBATT in *n*-tetradecane after 0-1 excitation. The excitation light at around 582 nm is filtered out. The strong line at 590 nm is the 0-0 ZPL of DBATT. The experimental values for the Debye-Waller and Franck-Condon factors are 0.7 and 0.3, respectively [22].

The sample praparation is greatly simplified by the fact that *n*-tetradecane is a liquid at room temperature, and freezes at around 6°C [123]. To fabricate a sample, first a minute amount of DBATT is solved in tetradecane and sonicated for around one hour to yield a saturated solution of slightly pink color. A droplet of this solution is applied onto the flat side of the SIL, and squeezed with a glass cover slip. This way a thin liquid film formed between the cubic circonia and glass, which froze quickly when inserted into the cryostat.

Sample structure and widefield images

Fig. 3.14 a) shows a typical white light image of a *n*-tetradecane sample in the cryostat. Most of the times the film that forms between SIL and cover slip cracks along multiple lines when cooled down to 1.4 K. Fig. 3.14 b) is a reflected image of the focus at the SIL/sample interface when the camera is focused on the molecule's fluorescence. A reason for this often observed out-of-focus appearance of the reflected laser is probably the strong achromaticity of an imperfectly aligned microscope system. The focus shift effect described in [122] is not likely to have a big influence since our SIL/sample interface does not result in total internal reflection.

Fig. 3.14 c) and d) show fluorescence images of DBATT molecules in the sample, obtained by wide-field illumination and blocking the excitation light with a long-pass filter. The frequency difference between c) and d) was about 500 MHz. The lower left corner of c) and d) seems to be less resolved, which is probably a result of aberrations in combination with a large number of background molecules. The upper right corner presents an area suitable for further experiments. Note that a), c) and d) were taken on a different date and sample than b), however, the effect for the reflected focus image as explained above could be observed similarly in different samples.

Saturation behavior

DBATT in *n*-tetradecane, in our experimental arrangement, showed a large fraction of single molecules that exhibited near to lifetime limited linewidths at low excitation power. Furthermore, several molecules sustained high driving fields with negligible light induced spectral jumps or matrix induced dephasing. See Fig. 3.15 as an example of consecutive fluorescence excitation scans of the same molecule at excitation powers changing by a factor 10^4. This approximately corresponds to saturation parameters S of 0.1 to 1000. The fluorescence intensity saturates while the

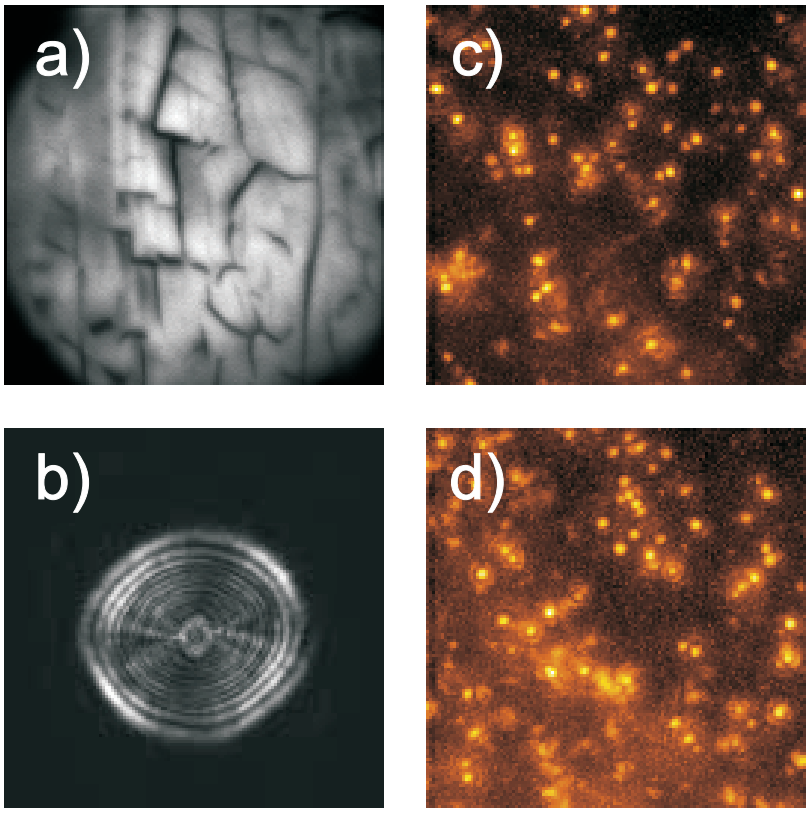

Figure 3.14: a) white light transmission image of a n-tetradecane sample, imaged through solid immersion lens and asphere. b) is a reflected image of the excitation focus when the red shifted molecular emission is focused on the camera, c) and d) fluorescence images of DBATT molecules in the sample. This image is in false color, but corresponds to what can be easily seen through the SIL with the unaided eye. See the text for explanations.

linewidth is power broadened in perfect agreement with Eq. (1.9). The power that is deposited in the system when a single molecule is in resonance with the external field is in the range of 50pW [4], which is not noticed in the contact gas filled sample chamber of the cryostat.

3.6 Cryostat

The Helium bath cryostat was a custom construction from `Cryovac` for experiments that combined cryogenic single molecule spectroscopy with scanning probe microscopy and which had been conducted in the group over the past 10 years. The specialty of the system is a comparably large cylindric sample chamber of 9cm

[4] At $S \gg 1$ the number of scattering events involving phonons is very roughly $\Gamma_1/2$=50 10^6, and the average fluorescence photon is Stokes shifted from 590 to 610nm. The matrix itself does not absorb noticeably.

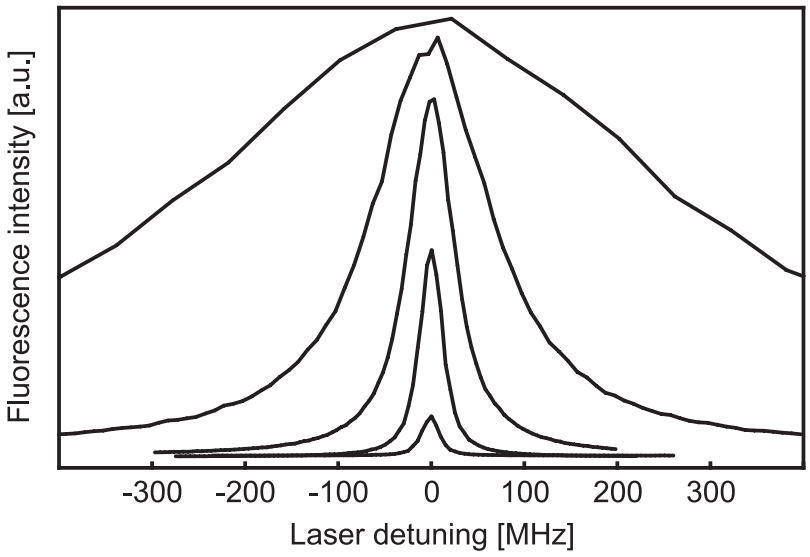

Figure 3.15: Fluorescence excitation spectra of the same DBATT molecule at different saturation parameters. The excitation power was raised by a factor of 10 000 from the lowest to the highest spectrum. The saturation parameters are approximately 0.1, 1, 10, 100, 1000. The FWHM changes from 19 MHz to 600 MHz, in agreement with Eq. (1.9) for negligible dephasing.

height and 14cm diameter, and 5 optical accesses. Nitrogen shields are missing in this cryostat to avoid mechanical vibrations due to boiling of the liquid, nonetheless the running time for the filled cryostat is up to 14 hours. A detailed description of the cryostat and the history of several different insets and improvements is given in various theses of the group [93, 126, 127, 128, 129]. This cryostat system provided enough space for a first solid immersion transmission microscope setup with multiple controllable axes.

3.6.1 Transfer system

The sample chamber is mounted directly under the lower helium tank which holds up to 6 liters of liquid helium, and can be connected to a vacuum pump in order to lower the temperature of the contained helium by following the vapour pressure curve to a minimum of 1.4K. The lower helium tank is connected to an upper tank which holds 8 liter of liquid Helium at 4.2K via a cold valve. Otherwise, these two tanks are not in direct thermal contact. The lower tank is surrounded by two thermal copper shields, and the whole system placed inside a vacuum vessel. When the cryostat is cold and full, the pressure in the insulating vacuum is in the upper 10^{-8} or lower 10^{-7} mbar range and keeps the temperature of 1.4K for up to 14 hours. During experiments the sample chamber is filled with a low pressure of helium gas as an exchange medium to ensure thermal equilibrium between all parts of the setup inside the cryostat. To exchange the insets of the cryostat, mainly the sample and

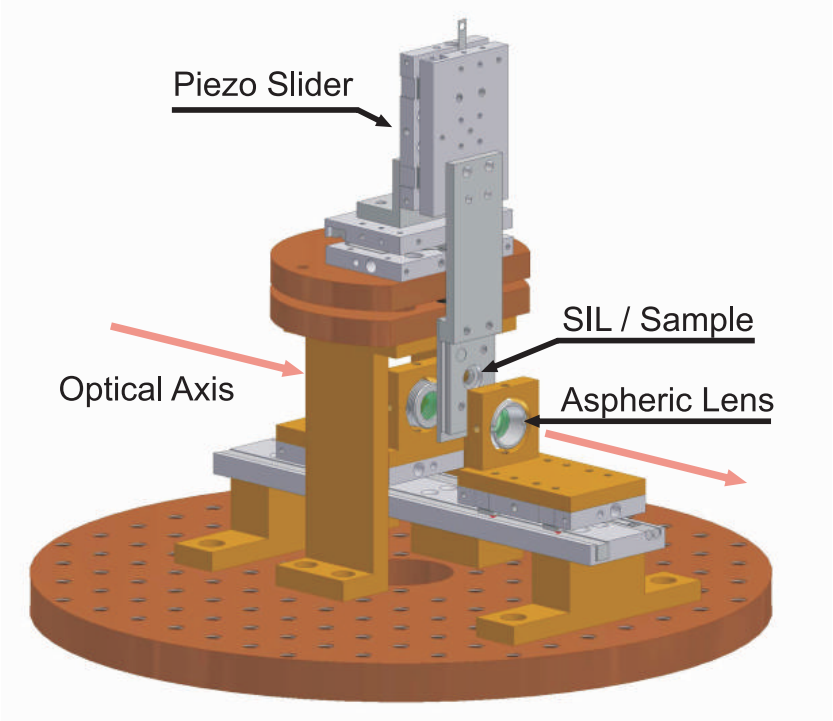

Figure 3.16: Cryostat setup, isoview and the most important parts.

the solid immersion lens setup, a transfer system was constructed. The sample setup, see Fig. 3.16, and the nessessary electrical contacts were attached to a long stainless steel rod that could be pulled into a vacuum lock, which allowed a sample exchange without exposing any cold parts directly to air.

3.6.2 Cryostat inset

The direction of this setup was to keep the aspheres and solid immersion lens with sample fully movable with respect to each other. This allowed the optimization of the lateral and on-axis position of the solid immersion lens while inside the cryostat. Piezoelectrically driven slip-stick linear motors (sliders) were employed to move the optical elements at cryogenic conditions. The sliders, described in detail in [127], were not designed in a very compact package which resulted in a somewhat spacious and complex 4 axes stage illustrated in Fig. 3.16.

The final version of the cryostat setup kept the aspheres inside the cryostat. This reduced the number of piezo-sliders on the transfer system, which were the most likely to break when warmed and cooled during sample exchange. Figure 3.16 shows the cryostat setup for the solid immersion transmission microscope. The aspheres were mounted on two piezo-sliders and placed on a rail at the bottom of the sample chamber to ensure their movement along the optical axis. Both lenses were held by four microscrews inside a larger bore, which allowed fine tuning of the two aspheres once the optical axis and the rail were set up to be parallel. This way we first tried to achieve a perfect focusing and recollimation of the laser beam from the telecentric

by just the two aspheres alone. The solid immersion lens, sample and cover slip were mounted on a holder which was attached to a X-Y piezo-slider stage. The whole system was held via a conus by the transfer system, so that after placing the solid immersion setup on its holder above the asphere-rail, the transfer system rod could be completely detached mechanically from the experiment.

4 Direct far-field extinction detection of single molecules

4.1 Direct extinction measurements

4.1.1 Setup and performance of the SIL objective

The solid immersion setup is schematically sketched in Fig. 4.1 a) and b). The tunable excitation laser light is directed into the cryostat via reflection off a glass wedge beam splitter [BS] which transmits 92 % of the light. This allows for the simultaneous detection of the Stokes shifted fluorescence at λ_{23} in the backward direction on PD2, while recording an extinction spectrum on PD1. A galvoelectric mirror pair and telecentric lens system is used to scan the excitation laser beam over the sample. Figure 4.1 c) shows the detected total fluorescence from a single DBATT molecule at T=1.4 K as the focus is scanned and the excitation frequency is kept on the molecular resonance. The molecule acts as a point-like and polarization sensitive detector of the intensity distribution in the focal area. The spot has a FWHM of 370 nm. We routinely measured intensity distributions in the same fashion in order to position the molecule under study in the diffraction focus. Images recorded with a single molecule at T=1.4 K look very similar to the ones obtained with fluorescent beads at room temperature (see Fig. 3.11 in Sec. 3.4).

4.1.2 Extinction

Detector PD1 positioned behind the cryostat recorded the excitation light intensity. In most cases, no additional optical elements were placed between the cryostat and the focusing lens of the detection APD, except for an optical short pass filter that blocked the Stokes shifted fluorescence of the molecule. Furthermore, all measurements presented in this work were directly recorded in single photon counting, and no lock-in detection was employed in the experiments. We typically worked with 1-2 million counts per second detected power on PD1 for the extinction measurements. When the laser frequency is scanned across the molecule's resonance, detector PD2 records a fluorescence excitation spectrum as shown in Fig. 4.2 a). On detector PD1 we simultaneously observed attenuation of the laser light that, depending on the achieved focus size, polarization overlap, sample properties and homogeneous linewidth of the molecule, showed visibilities between 5 and 11 percent. Displayed in Fig. 4.2 b) is the maximum extinction by a single molecule measured in this setup. A dip of 11.5 % is determined by the Lorentzian fit through the experimentally measured points. This spectrum was recorded for 160 ms per pixel at an excitation of

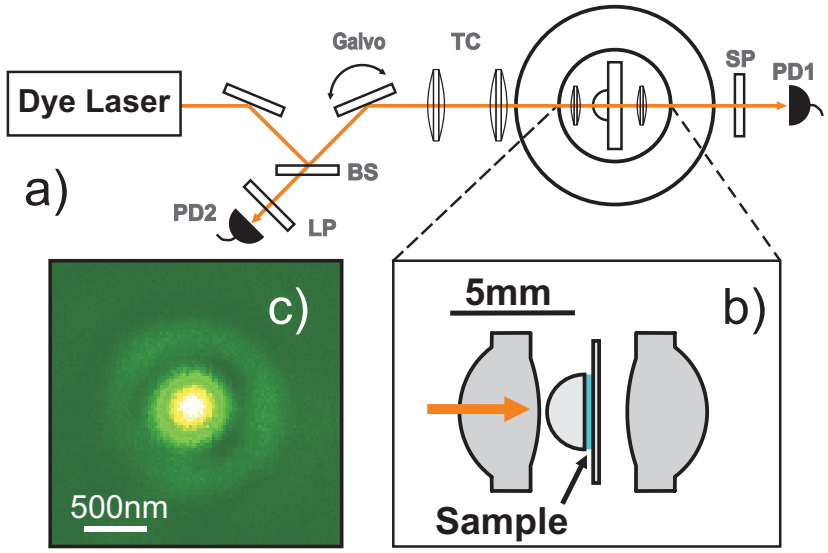

Figure 4.1: Optical setup for single molecule far-field extinction measurements. Detector PD1 is placed directly outside of the cryostat, behind an optical short-pass filter SP that blocks Stokes shifted fluorescence from the molecule. All measurements are recorded on PD1 directly, without the use of modulation techniques. b) is a close-up of the cryostat inset and shows the asymmetric sample geometry. c) displays a focus scan over a single molecule which yields a focal spot FWHM of 370 nm at 1.4K.

(detected) 130.000 cps. The noise amounts to 0.7 %, which is limited by the shot noise of this measurement.

Visibility and phase

Equations (2.8) are valid for point-like detectors in the far field, but an extended detector integrates I_{total} over its surface area. An experimental focusing and recollimation system, however, maps the incoming near-plane wave fronts of a propagating beam onto spherical wave fronts and back onto the outgoing beam. One can safely assume that a focused excitation beam and the emission from a dipole in the focus have matching spherical phase fronts. The total signal P_{total} recorded on an extended detector, and each of its terms, can be described with a set of equations of the same form as Eq. (2.8).

Generally, the recorded spectrum will be negative Lorentzian due to energy conservation. However, the experimentally observed spectra sometimes show a slight deviation from this shape, hinting at non-ideal experimental conditions. On the other hand, the phases of the involved fields can be strongly manipulated at will, yielding dispersive or even positive Lorentzian spectra. Examples of such situations are Sec. 4.4 and the experiments in Chap. 6. For these reasons, recorded spectra were always fitted with a phase ϕ as free parameter.

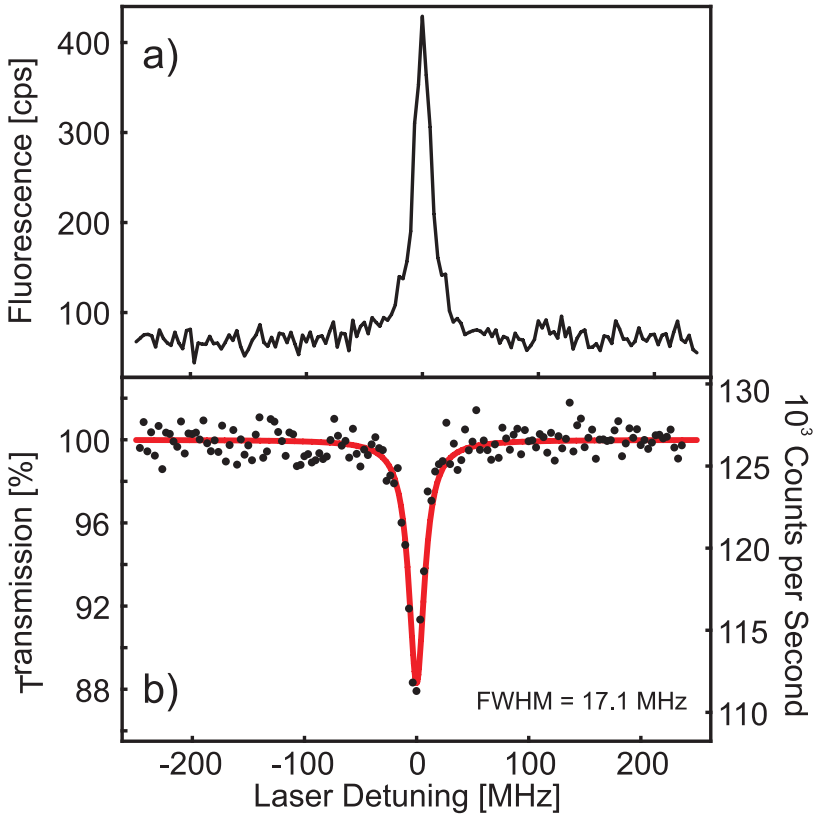

Figure 4.2: Fluorescence excitation and simultaneously recorded far-field extinction spectrum of a single DBATT molecule at T=1.4K. The molecule exhibits no dephasing and is optimally aligned with the input polarization. The integration time per pixel was 160ms, and the cryostat-incident power amounted to roughly 180fW.

In the regime of efficient interaction, i.e. if P_{21} is comparable to $P_{\rm inc}$ and $P_{\rm intf}$, its presence will influence the shape of the recorded spectrum. One can recollect the terms of Eqs. (2.8) into a purely absorptive or emissive part with coefficient $\mathcal{M}$, and a purely dispersive component with coefficient $\mathcal{N}$, according to

$$P_{\rm total} = P_{\rm inc} + \frac{\Gamma_2(\mathcal{M}\Gamma_2 + \mathcal{N}\Delta)}{\Delta^2 + \Gamma_{\rm eff}^2} \ , \tag{4.1}$$

where

$$\begin{aligned} \mathcal{M} &= C_{21}P_{\rm inc} - 2C_{\rm intf}P_{\rm inc}\sin\phi \\ \mathcal{N} &= -2C_{\rm intf}P_{\rm inc}\cos\phi \ . \end{aligned} \tag{4.2}$$

On the other hand, in the weak interaction limit, $C_{\rm intf}$ is small and P_{21} will be negligible compared to $P_{\rm intf}$. The remaining signal is then almost exclusively due to the interference of the coherently scattered field and the excitation field. One

can assign a visibility $\mathcal{V}$ and phase ϕ to the spectrum which in the low interaction regime is directly related to the coefficients in Eq. (2.8)

$$P_{\text{total}} = P_{\text{inc}} \left(1 - \mathcal{V} \frac{\Gamma_2(\Delta \cos\phi + \Gamma_2 \sin\phi)}{\Delta^2 + \Gamma_{\text{eff}}^2} \right) , \tag{4.3}$$

with

$$\begin{aligned} \mathcal{V} &= 2C_{\text{intf}} \\ \phi &= \arg(\mathrm{g}^* \mathrm{f}) = \phi_{\mathrm{f}} - \phi_{\mathrm{g}} . \end{aligned} \tag{4.4}$$

The values for $\mathcal{V}$ and ϕ obtained from such a fit are indicated in a number of scans.

4.2 Visibility versus efficiency

The spectrum shown in Fig. 4.2 suggests that 11.5 % of all photons interacted with the single molecule. However, this is only true as long as all the excitation light is re-collimated and detected. In our case, as explained in chap.3.4, the transmission of light through the cryostat amounts to 25 %. A large part of the light is absorbed in or reflected from cryostat windows or the solid immersion lens, and a portion of roughly 20 % of the excitation light is not collected anymore due to the asymmetric SIL/sample setup. Parts of the lost light can still interfere with the coherently scattered light from the molecule and lead to a nonvanishing integrated extinction outside the detected solid angle [70]. Saturation scans offer a way to nonetheless quantify the absolute efficiency of interaction.

4.2.1 Saturation scans

The total extinct power for a two-level system is given by Eq. (2.3) as $P_{\text{ext}} = \hbar\omega_0 \Gamma_1 \rho_{22}^{\text{ss}}$. In the case of DBATT the triplet factor $K = 1.14$ has to be taken into account, and if dephasing is negligible this equation is

$$P_{\text{ext}} = \hbar\omega_0 \Gamma_1 \frac{1}{2} \frac{S}{1 + KS} . \tag{4.5}$$

With the known excited state decay rate $\Gamma_1/2\pi = 16$ MHz [25], the total extinct power for a resonance at 590 nm and S=1 is $P_{\text{ext}} \approx 7.8$ pW. This power can be compared to the incident power as measured on a powermeter, in front of the cryostat, at this saturation parameter.

Fig. 4.3 displays a saturation scan of a single DBATT molecule[1]. The vertical axis shows Stokes shifted fluorescence P_{23} in cps, measured in the backward direction on PD2. The data was fitted with a function proportional to $S/(1+KS)$. The bottom horizontal axis shows the saturation parameter S obtained from this fit. The top axis is the incident power in picoWatt, calculated from the data recorded on a calibrated logarithmic photodiode PD behind the beam splitter BS. A scaling factor between

[1] This scan was recorded on the same molecule that was used for the Mollow-triplet measurement explained in chapter 6

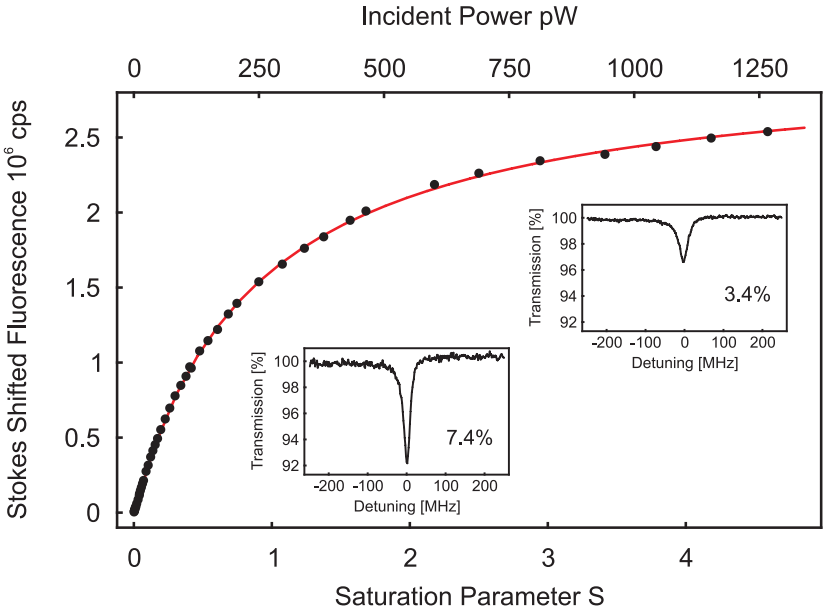

Figure 4.3: Saturation scan of a single DBATT molecule in *n*-tetradecane. The red curve is a fit proportional to $S/(1+KS)$. The incident power at the molecule's position was derived from a photodiode reading before the laser beam entered the cryostat (see the text for details of the diode calibration). The power at which the molecule saturates allows for an independent determination of the interaction efficiency. Insets: two extinction measurements recorded on PD1 at saturation parameters of $S \ll 1$ and $S = 1$.

the power measured on this diode, and the power at the location of the molecule was calculated as follows: a factor of 10 between the photodiode reading and the power directly in front of the cryostat was verified for this particular experiment. A factor of 2 is lost because of a 50/50 beam splitter in front of the cryostat, and another factor of 2 due to a 45° alignment of the molecule with respect to the linear polarized incident light. This was a specific feature of the Mollow triplet measurement that was performed on this molecule, but was deliberately set, carefully characterized and does not interfere with the general argument given here. Lastly, a factor of 0.7 was measured as the power lost due to 4 cryostat windows, one aspheric lens and reflections on the SIL surfaces. The determined power needed to arrive at S=1 for this molecule is 270pW. For this experiment the efficiency of interaction at S=1 is therefore roughly $(P_{\mathrm{ext}}/P_{\mathrm{inc}})|_{\mathrm{S}=1} \approx 2.9$ %. Keeping in mind that at S=1 the system is already in the nonlinear regime, the efficiency at zero incident power would be 5.8 %. The value has a small uncertainty as the exact excitation power at the position of the molecule has to be derived indirectly, but it corresponds closely to the simultaneously recorded extinction spectra with 3.4 % and 7.4 % visibility as shown in the insets in Fig. 4.3.

These kind of saturation experiments have been recorded a number of times, but mostly on molecules that did not show a strong extinction as in the above example.

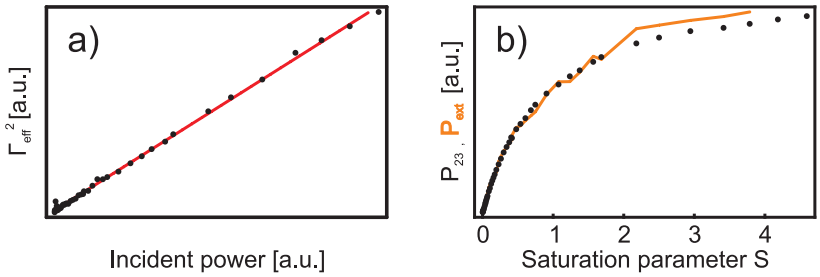

Figure 4.4: Dependence of the squared linewidth and extinction signal on saturation parameter. a) is the squared linewidth of the fluorescence excitation spectra versus excitation power. A linear dependence shows that no additional dephasing processes are introduced by higher driving fields and $\Gamma_2 \approx \Gamma_1/2$. The orange line in b) plots P_{ext}, the absolute signal of the extinction dip versus saturation parameter, whereas the dots are the fluorescence excitation data P_{23}, multiplied with a scaling factor. The fit to the P_{23} data was displayed in Fig. 4.3. Around S=2 a ND filter change in front of PD1 caused a systematic deviation of P_{ext} from the fluorescence excitation data.

Each time the obtained values of $(P_{\mathrm{ext}}/P_{\mathrm{inc}})|_{\mathrm{S}\to 0}$ between 2 and 6 % were similar to the simultaneously measured extinction visibility. However, in all cases the extinction spectra show a visibility that is 10-20 % larger than the interaction efficiency as determined by saturation scans. This again hints at a non negligible amount of incident laser light interfering with the molecular emission in an undetected solid angle [70]. For this reason the saturation intensity gives an alternative measure for the absolute interaction efficiency which does not depend on the exact sample geometry, whether measured via Stokes shifted fluorescence or the extinction signal itself.

Power broadening

Fig. 4.4 a) shows the squared FWHM of the fluorescence excitation spectra, plotted versus the incident power. Recalling Eq. (1.9), a linear dependence on the incident power is expected, if no additional dephasing channels are introduced at higher excitation. In this and most other saturation experiments, the corresponding curve is nearly perfectly linear. The extrapolated intercept at $\Omega = 0$ directly gives the value $\Gamma_2/2\pi = 10$ MHz in the above example. The dephasing rate $\Gamma_2^*/2\pi$ derived from such scans yields values of 2-3 MHz.

Extinction saturation

The right side of Fig. 4.4 shows the absolute extinction signal (orange line), measured on PD1 for the same saturation scan, together with the Stokes shifted fluores-

cence signal (dots) times a scaling factor. The extinction signal saturates according to $S/(1+KS)$ in the same way the fluorescence does, and the visibility reduces with $1/(1+KS)$. The saturation behavior of the extinction term is derived in Eqs. (2.8). Note that a systematic deviation from the ideal curve above S=2 coincides with the insertion of a neutral density filter in front of PD1, which might have caused a beam shift and different detection efficiency.

4.2.2 Saturation intensity and detection efficiency

The value of 270 pW input power to saturate the molecule corresponds to an intensity of circa $90\frac{\mathrm{mW}}{\mathrm{cm}^2}$ in the 370 nm FWHM focus (which is roughly 630 nm $1/e^2$-diameter). Saturation intensities in this range have been obtained for DBATT in n-tetradecane in earlier work by Durand et al. [130]. Furthermore, a saturation scan directly allows us to estimate the collection efficiency of PD2. The power emitted into Stokes shifted fluorescence amounts to $P_{23} = P_{\mathrm{ext}}(1-\alpha_{\mathrm{FC}})$. With a Franck-Condon factor of 0.3 [22] a comparison with the saturation data results in a collection efficiency of 9.8 %. This value is relatively large [131], because the emission is backward-detected on PD2, and the high-index SIL favors emission into this direction [132]. Experiments in which Stokes shifted fluorescence of a molecule was measured in both directions showed that the collection efficiency is about ten times larger on PD2 than PD1.

4.3 Extinction imaging

An interesting question is how the extinction of light by a single quantum emitter changes with different excitation geometries, i.e. with the molecule displaced from the focus center. Another question is how angularly resolved extinction spectra look before integrating over a larger detector surface in the far field. We have performed two different experiments which explore these questions. The theoretical description of extinction e.g. for a displaced gaussian focus is beyond the aim of this work, and requires a more rigorous mathematical treatment [133]. Nonetheless, the two examples given below provide a qualitative impression on what effects are to be expected.

A third possibility, the detection of extinction in wide-field illumination would coincide most with the intuitive picture of a shadow against a bright background. The coherent nature of the excitation light, however, makes such an experiment challenging, because any roughness of the sample leads to a strong interference pattern in the far field that would be hard to separate from the signal of a single molecule. A similar experiment was performed with gold particles in our group [134], where the whole sample was spatially modulated with a piezo-scanner and later deconvolved. The strong frequency dependence of single molecule signals compared to the relatively stationary background interference pattern could be a way to realize wide-field extinction imaging also in single molecule samples.

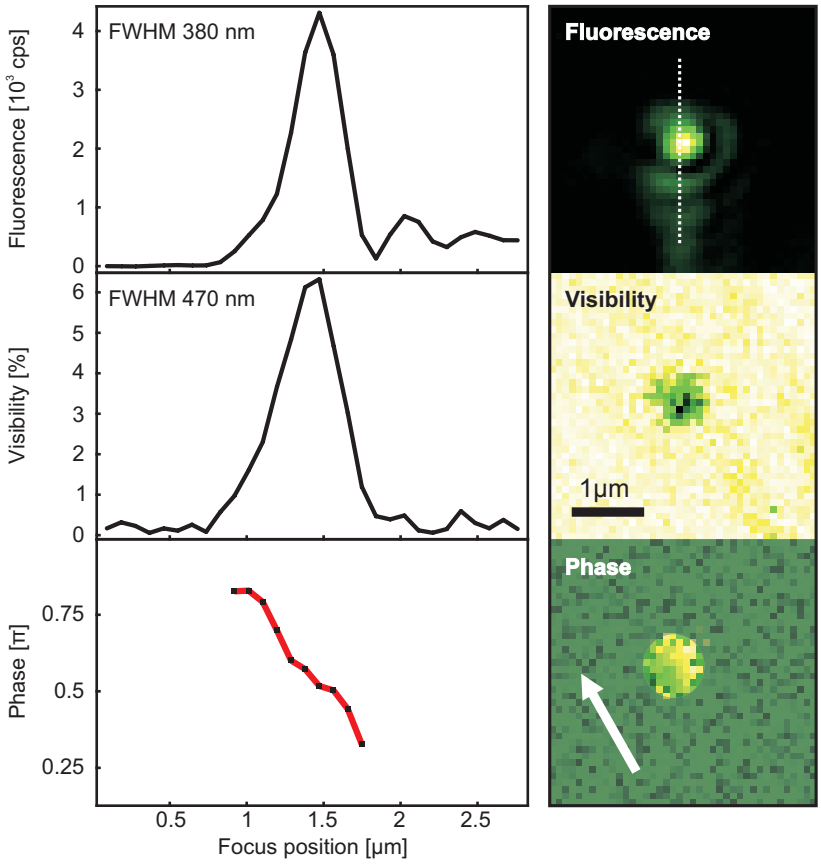

Figure 4.5: Spatial scan of the focus across a single molecule with 100 nm resolution. At each point a laser scan was performed, leading to both a fluorescence excitation and an extinction spectrum. The right side panel shows fluorescence intensity, extinction visibility and phase as a function of position of the focus. To blind out those parts with very small visibilities, the phase-image was partially masked. The arrow indicates the independently determined orientation of the polarization and molecular dipole moment. The left side shows a higher-resolution linescan along the dotted line shown on the right.

4.3.1 Lateral focus scan

Usually the spatial position of the excitation laser focus was adjusted to yield the maximum Stokes shifted fluorescence. Figure 4.5 is one example where the focus was scanned across the sample in steps of 100 nm, and at each position a fluorescence excitation and extinction spectrum was recorded. The right side shows images derived from the analysis of the spectra, the left side displays one-dimensional scans, recorded after the image scan and with a slightly higher spatial resolution. The top shows the intensity of fluorescence from the molecule, i.e. the focal intensity distribution, and a one-dimensional scan along the dotted line. The FWHM is on the order of 380 nm, and the focus shape not perfectly symmetric. This might be a result of imperfect alignment of the focusing asphere and SIL with respect to the

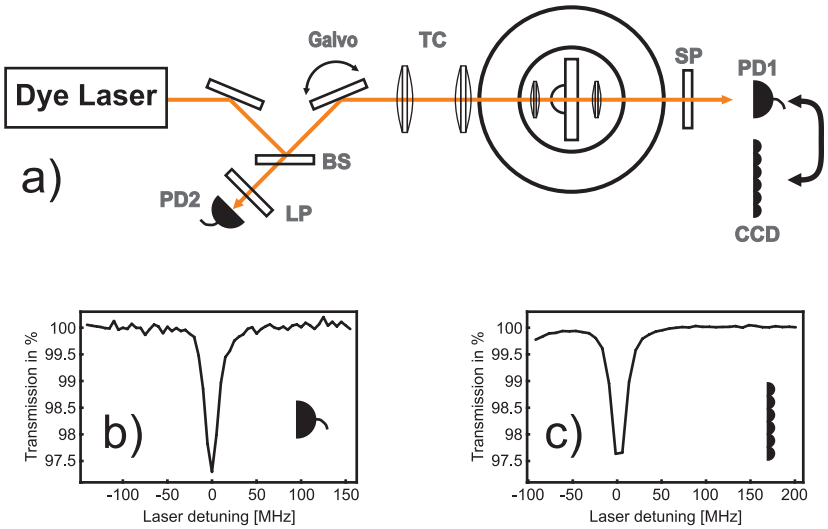

Figure 4.6: Setup for angularly resolved extinction measurements. The detector PD1 was replaced by a 128x128 pixel CCD camera which recorded the unfocused collimated beam exciting the cryostat. b) is the extinction spectrum on the single-pixel APD detector, c) the sum of all individual extinction spectra of the camera pixels.

optical axis. The extinction spectrum at each position was fitted with Eq. (4.3), and the resulting visibility and phase plotted. The visibility is maximally 6 % at the center position. The FWHM of the visibility linescan yields a larger value of 470 nm.

Energy conservation requires that the shape of the extinction spectrum measured on a forward detector should always be absorptive and P_{ext} is proportional to P_{23}. Figure 4.5 clearly shows that depending on the position of the scatterer in the beam, the overlap of excitation and emission modes can strongly vary, leading to a nontrivial dependence of the integrated extinction shape. Also, the larger FWHM of the extinction linescan is not in accordance with energy conservation. These experiments show the need for a more complete collection of the excitation light in experiments that change the illumination geometry.

4.3.2 Camera image and angular distribution of the extinction signal

The Andor iXon EMCCD camera (see chapter 3.2.2 for details) was used in a number of experiments to record the angular distribution of the interference term I_{intf} without integration over a detector surface. This was previously done for the case of near-field excitation as summarized in the thesis of Ilja Gerhardt [93]. Some theoretical work has been published on this topic, notably on the change of photon statistics in different directions [135], caused by areas of constructive and destructive interference. Especially if the molecule is displaced with respect to the center of the excitation focus or interferes with reflected parts of the excitation light, locally more complex interference patterns can be expected.

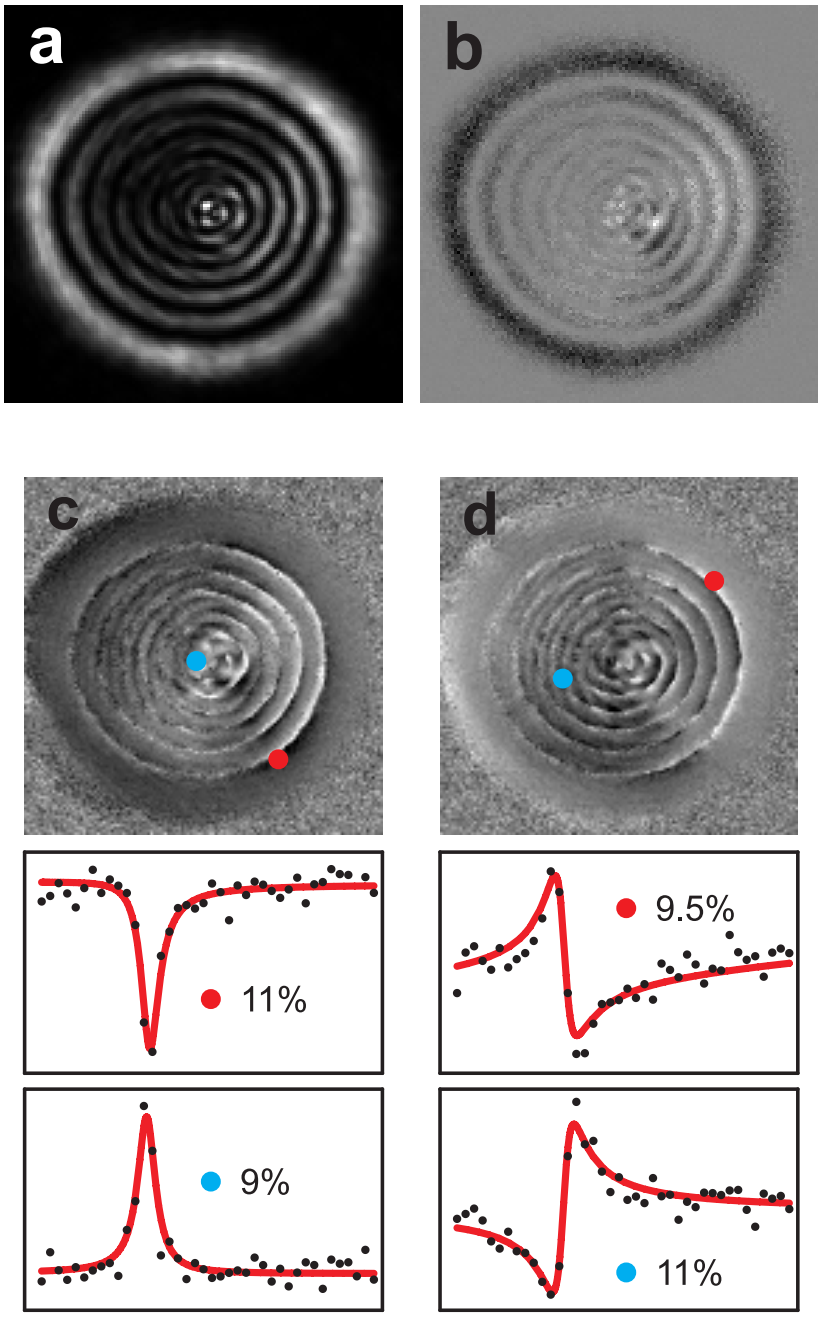

Figure 4.7: Angularly resolved extinction spectra. a) is the unfocused image of the collimated excitation beam after the cryostat, exhibiting a Fraunhofer diffraction pattern. b) shows the off-resonance image substracted from the on-resonance image, c) and d) show the results of fits to the extinction spectrum recorded on each camera pixel. For details see the text.

Fig. 4.6 a) shows the setup for this experiment. We can switch between an APD which records an angularly integrated transmission spectrum, and the Andor iXon CCD camera which was used without an objective. The re-collimated laser beam from the cryostat has roughly the same diameter as the camera CCD chip. The recorded cross section of the beam shows a pattern as depicted in Fig. 4.7 a), and the ring-like structure is caused by Fraunhofer diffraction of the beam on the edges of the collimation asphere. This pattern can be calculated using the aspheric lens diameter of 5mm and a distance between lens and CCD array of 1.5 m. It is desirable to avoid this diffraction by directly imaging the back-focal plane [93, 136] in which the radiation pattern of both the molecule and the excitation beam should be undisturbed by the back-aperture. However, even in this mode we have observed strong interference patterns in the excitation light image, probably caused by the many optical interfaces in the beam path.

After optimization of the focus size and position, first an extinction spectrum was recorded on an APD, to obtain a typical, beam-integrated value for the extinction visibility and phase. This scan is shown in Fig. 4.6 b). Next, the APD was replaced by the CCD camera, and the readout speed and amplification were adjusted to take advantage of the full 16 Bit greyscale resolution at 128 x 128 pixels. The laser was scanned in 40 steps across the molecular resonance, and the camera was triggered at each pixel. A first impression of directional extinction patterns can be seen by substracting an off-resonance image from the on-resonance image. Such a plot is shown in Fig. 4.7 b). Clearly visible is destructive interference mainly on the outer ring of the Fraunhofer pattern, but also bright rings that indicate constructive interference. This is a sign that depending on the detector direction the distribution functions f and g of the molecular emission and excitation light from Eq. (2.8) can aquire any relative phase between 0 and 2π.

To fully analyze the data, the laser scan corresponding to each of the 128 x 128 pixels was fitted with Eq. (4.3), and visibility $\mathcal{V}$ and phase ϕ were extracted. To visualize the results of these fits, the panels in Fig. 4.7 c) and d) show an image of $\mathcal{V}\sin\phi$ and $\mathcal{V}\cos\phi$, respectively. This way the areas with extinction shapes close to absorptive or emissive (in c), and those with dispersive shapes (in d) are emphasized. Below each image, two examples of areas with distinct shapes and high visibility are shown. The visibility reaches values of more than 10 %, mainly in areas that show a dark fringe in the Fraunhofer diffraction pattern. A surprising feature is the strongly fluctuating phase of the extinction pattern with distance from the beam axis, with the phase flipping by π sometimes within a few pixels (each pixel has a size of 24 μm). This pattern is most probably due to a small shift of the molecule's position with respect to the origin of the focused beam [133] or interference with multiply reflected excitation light. These kind of experiments need further attention and more reproducible conditions. Nonetheless, if the sum spectrum of all 128 x 128 pixels is taken, the resulting extinction spectrum again recoveres what was seen on the "single-pixel" APD as evident in Fig. 4.6 c).

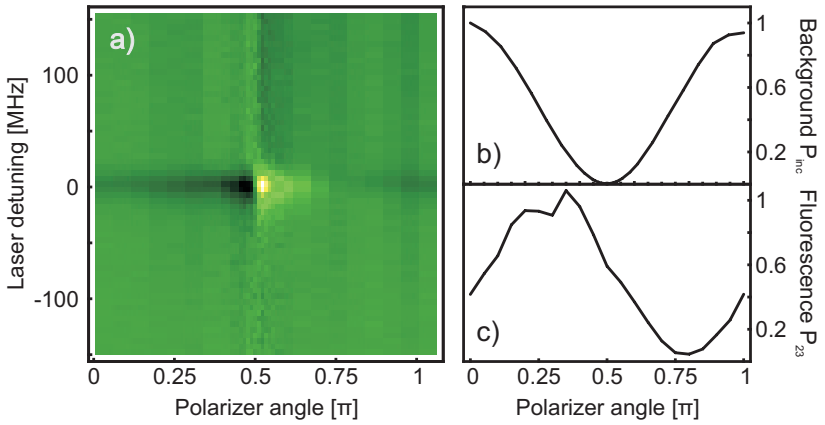

Figure 4.8: A polarizer in the detection path manipulates phase and visibility of extinction. a) All extinction spectra as a function of polarizer angle ψ_{P}, b) and c) show the recorded excitation power P_{inc} and Stokes shifted fluorescence P_{23} as a function of polarizer angle.

4.4 Phase manipulation

The scattered field and the excitation field interfere on the detector and yield an extinction spectrum that is in most cases negative Lorentzian in our experiments. Above we have shown that when using a limited detection area, depending on the detector position, other lineshapes can arise. Here I will introduce an experiment where the relative phase between the excitation and scattered field is manipulated deliberately. A very similar scheme is later used to determine the absolute intensity of coherently scattered radiation.

If the molecular dipole orientation is offset with respect to the illumination beam's linear polarization, the relative amplitudes and phases of excitation and scattered fields can be changed by placing a linear polarizer between the cryostat and the detector and then rotating it to a desired angle. In this manner, the visibility of the extinction signal can easily be increased to more than 20 %, however at the cost of signal to noise ratio. In the experiment shown in Fig. 4.8 the illumination orientation is fixed at zero degrees[2], and the molecular orientation rotated by an angle ψ_m. A linear polarizer with an angle ψ_p with respect to the excitation light axis is placed in front of the detector. The unit vectors for the fields involved as well as the polarizer $\hat{P}$ read

$$\hat{\mathbf{E}}_{\mathrm{inc}} = \mathcal{E}_{\mathrm{inc}} \begin{pmatrix} 1 \\ 0 \end{pmatrix}, \quad \hat{\mathbf{E}}_{21} = \mathcal{E}_{\mathrm{m}} \begin{pmatrix} \cos\psi_{\mathrm{m}} \\ \sin\psi_{\mathrm{m}} \end{pmatrix}, \quad \hat{\mathbf{P}} = \begin{pmatrix} \cos\psi_{\mathrm{p}} \\ \sin\psi_{\mathrm{p}} \end{pmatrix}$$
$$\mathcal{E} = \begin{pmatrix} \cos\epsilon & i\sin\epsilon \\ i\sin\epsilon & \cos\epsilon \end{pmatrix},$$

[2]The linear polarization axis of the excitation light is defined to be the zero degree axis, no matter where in the lab frame it might lie.

where the matrix $\mathcal{E}$ introduces an elliptic component to the molecular and excitation field with ellipticities of ϵ_{m} and ϵ_{inc}, respectively. The detected power of the three terms in Eq. (2.8) become

$$\begin{aligned} P_{\mathrm{inc}} &= P_0|\hat{\mathbf{P}}\cdot\hat{\mathbf{E}}_{\mathrm{inc}}|^2 = \cos^2\psi_{\mathrm{P}} P_0 \ , \qquad P_0 = \varsigma|g|^2 E_0^2 \\ P_{21} &= C_{21}|\hat{\mathbf{P}}\cdot\hat{\mathbf{E}}_{\mathrm{m}}|^2\cos^2\psi_{\mathrm{m}} P_0 \frac{\Gamma_2^2}{(\Delta^2+\Gamma_{\mathrm{eff}}^2)} \\ P_{\mathrm{intf}} &= -2C_{\mathrm{intf}}\cos\psi_{\mathrm{m}} P_0 \Re\left\{\left(\hat{\mathbf{P}}\cdot\hat{\mathbf{E}}_{\mathrm{inc}}\right)^*\left(\hat{\mathbf{P}}\cdot\hat{\mathbf{E}}_{\mathrm{m}}\right)e^{i\phi}\left(\Delta - i\Gamma_2\right)\right\}\frac{\Gamma_2}{\Delta^2+\Gamma_{\mathrm{eff}}^2} \\ &= -2C_{\mathrm{intf}}\cos\psi_{\mathrm{m}} P_0 |\hat{\mathbf{P}}\cdot\hat{\mathbf{E}}_{\mathrm{inc}}||\hat{\mathbf{P}}\cdot\hat{\mathbf{E}}_{\mathrm{m}}|\frac{\Gamma_2\left(\Delta\cos\Phi + \Gamma_2\sin\Phi\right)}{\Delta^2+\Gamma_{\mathrm{eff}}^2} \ . \end{aligned} \tag{4.6}$$

The extra $\cos\psi_{\mathrm{m}}$ terms in P_{21} and P_{ext} come from the reduced Rabi frequency due to the rotated molecular orientation. In the extinction term one can recognize a visibility and phase of

$$\begin{aligned} \mathcal{V} &= 2C_{\mathrm{intf}}\frac{|\hat{\mathbf{P}}\cdot\hat{\mathbf{E}}_{\mathrm{inc}}||\hat{\mathbf{P}}\cdot\hat{\mathbf{E}}_{\mathrm{m}}|}{|\hat{\mathbf{P}}\cdot\hat{\mathbf{E}}_{\mathrm{inc}}|^2}\cos\psi_{\mathrm{m}} \\ \Phi &= \arg\left[\left(\hat{\mathbf{P}}\cdot\hat{\mathbf{E}}_{\mathrm{inc}}\right)^*\left(\hat{\mathbf{P}}\cdot\hat{\mathbf{E}}_{\mathrm{m}}\right)\mathrm{e}^{\mathrm{i}\phi}\right] \ , \end{aligned} \tag{4.7}$$

where ϕ is the phase of the interference term in the case of colinearly polarized molecule and illumination. In general, an ellipticity of both the molecular emission and the excitation field has to be taken into account, which will be particularly important if the polarizer is nearly crossed with the excitation or molecular field.

Fig. 4.8 b) shows the excitation light power P_{inc} as a function of the linear polarizer angle ψ_{P}, normalized by P_0. The detected power follows a $\cos^2$ function, and the minimum power is a factor of 285 smaller than the maximum. The ellipticity can be estimated to be $|\epsilon_{\mathrm{inc}}| \leqslant 0.05$, which was achieved by optimizing the Berek variable waveplate in the excitation beam path. c) is the Stokes shifted molecular fluorescence P_{23} which is proportional to P_{21}, recorded on PD1 after insertion of an optical long pass filter. The angle ψ_{m} can be fitted to be close to 45°. The apparent ellipticity ϵ_{m} is larger in this case, probably due to birefringence in the detection path, or a residual on-axis component of the dipole moment. The spectra P_{total} for 12 different polarizer positions are shown on the left side as a density plot, normalized by the respective background power P_{inc}.

Fig. 4.9 shows the results of fitting each of the extinction spectra, as a function of ψ_{P}. Part a) shows the visibility and the phase, according to Eq. (4.3). When the polarizer is perpendicular to the excitation light, the phase Φ jumps by π from absorptive to emissive, and the visibility reaches values up to 23 %. A more elliptic polarization of the excitation light washes out the phase jump, resulting in extinction spectra with dispersive shapes. The visibility exhibits a drop close to the crossed polarizer position, which is caused by the P_{21} term becoming comparable to P_{ext}. Another, more washed out, phase jump by π follows when the polarizer is crossed with the molecular dipole direction, and here the visibility is minimal.

A fit of the data with Eq. (4.1) yields the parameters $\mathcal{M}$ an $\mathcal{N}$ which specify the amount of absorptive and dispersive components of the spectrum. These parameters behave sinosoidal with ψ_{P} and can be used to fit values for C_{ext} and C_{21}. An example of such an analysis is given in chapter 6.

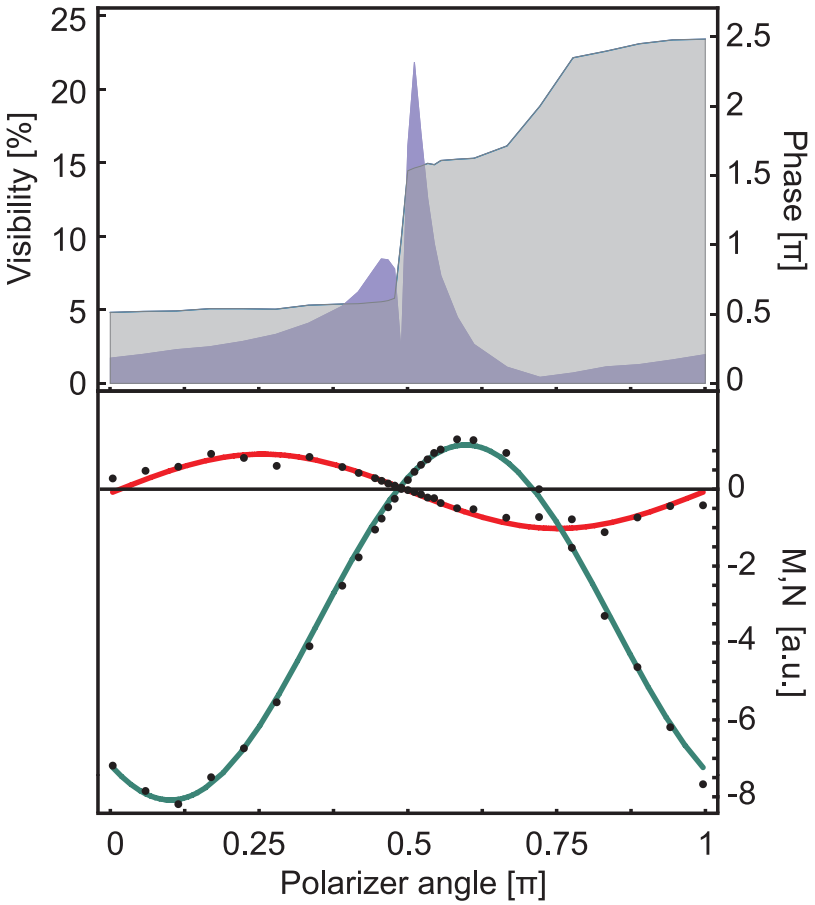

Figure 4.9: Fitresults for the extinction spectra shown in Fig. 4.8. The upper graph is visibility $\mathcal{V}$ and phase Φ, the lower graph the absorptive $\mathcal{M}$ and dispersive $\mathcal{N}$ components of P_{total}.

4.5 Discussion and outlook

Fig. 4.2 displays a direct far field transmission spectrum with 11.5 % visibility. Extrapolation of these results for a two-level with α=1 would lead to a roughly 5 times larger extinction signal, and 50-60 % visibility in our geometry, in which case the resonance fluorescence term would have a non negligible effect. To rate these numbers, an experimental exploration of the limits of interaction efficiency between a single emitter and a freely propagating laser beam is needed. Strong focusing via Weierstrass SILs is one option [116], but also the use of metallic nanostructures that influence the emission pattern of the emitter, similar to antennas at radio frequencies [137]. In this context saturation scans provide a way to quantify the true efficiency of interaction without the full knowledge of mode patterns and detection efficiencies. This is important, since as angle resolved detection via a camera demonstrates, the interferometric extinction signal seen on a limited detector area can over- or underestimate the true interaction efficiency.

The deliberate manipulation of the phases of excitation and coherently scattered

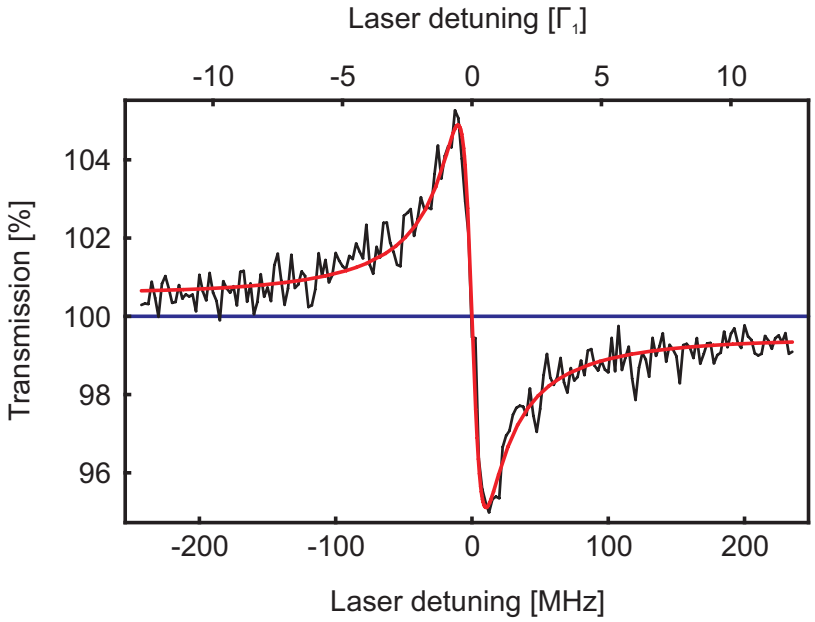

Figure 4.10: Purely dispersive response of a single molecule. The phases of the scattered light and excitation light are changed independently by insertion of a quarter wave plate and a linear polarizer in front of PD1.

light can be used to measure phase shifts of light far off resonance, rather than directly absorptive responses. Figure 4.10 shows an example of a purely dispersive transmission spectrum, obtained by inserting a quarter waveplate (QWP) and linear polarizer (LP) in the detection arm, and off-setting the molecular dipole moment with respect to the excitation polarization[3]. A far detuned laser beam essentially experiences a phase shift which is detected interferometrically, without exciting the molecule. This is a useful situation for a number of reasons. One example is that the illumination power can be increased without saturating the transition [138], which relaxes the requirements on the detection. Additionally such a configuration, in combination with a method to prepare the molecule in a certain superposition of ground and excited state, would enable the application of conditional measurable phase shifts to a laser beam in a single pass.

[3]In this particular example the presence of QWP and LP reduces the transmission of the system by a factor of about 4.

5 Ultrasensitive detection of single molecules

5.1 Detection methods

A single emitter placed in an excitation beam can be detected directly via its fluorescence, or interferometrically by mixing the coherent emission with the excitation light, i.e. via extinction. In both cases the signal-to-noise ratio (SNR) evaluates the quality of the measurement, or the prospect of succeeding in it, by comparing the signal caused by the emitter to the noise of the measurement system. The total signal on a detector in the far field is

$$P_{\text{total}} = P_{\text{las}} + P_{\text{fluo}}^{\Sigma} + P_{\text{ext}} \ . \tag{5.1}$$

One can choose to record the second or the third term in the above equation, P_{las} is just the original laser power that hits the detector. The term P_{fluo}^{Σ} is composed of resonance fluorescence and Stokes shifted fluorescence, the superscript Σ denotes the solid angle of light detection. The key to successful detection of the fluorescence is efficient rejection of P_{las}, which is achieved via geometrical blocking or optical filtering. Examples are total internal reflection (TIR) microscopy [139], the use of waveguide structures for perpendicular detection [72] or fluorescence excitation [3]. Major sources of noise in this type of detection, other than the detector dark count noise, can be spurious lights from autofluorescence or Rayleigh scattering from the sample matrix. Detecting P_{ext}, or the exctinction, takes on an opposite approach in the sense that the excitation light is interfered with the coherent fluorescence, and one monitors the resulting change in the excitation beam intensity [2, 14, 59, 140]. Alternatively, instead of using common-path excitation light, one can introduce a coherent external reference beam to emulate the interference effect of extinction [69, 70, 141]. In this method the major source of noise is the laser intensity fluctuation, which in the ideal case reduces to the quantum shot-noise. The detector dark counts are not as detrimental as in the case of fluorescence detection. Extinction is basically a homodyne detection method [142, 143], and the excitation light as local oscillator shifts the background above the dark count level.

Extinction detection of single emitters has experienced increasing popularity during the past few years. An important feature for the detection of ever smaller gold nanoparticlesis is that the scattered field (and hence the extinction) is proportional to the volume of the particle, whereas the intensity of the emission term (or rather scattering term) is proportional to volume squared [141]. Extinction detection also provides phase information which is lost in fluorescence excitation or modulation

techniques used in the early extinction measurements. It therefore offers complete access to the particle or emitters complex dielectric constant [69, 144, 145]. As I will show below, extinction detection should -in the low power and shot-noise limited regime- provide a superior SNR to a direct measurement of the fluorescence signal, especially if background is present or non-ideal detectors are used. However, the relative extinction signal has to be larger than the laser amplitude noise. This condition made the widespread use of single emitter detection via extinction challenging, as it requires highly efficient interaction between the emitter and the excitation light.

In the experiment presented in this chapter, we detected a single dye molecule via both Stokes fluorescence and extinction on one and the same detector and directly compared the obtained signal-to-noise ratios in a shot noise limited regime. We investigated this in the excitation range far below and above saturation, for very fast data acquisition and long integration times. A quantitative treatment is given which depends on a number of experimental parameters that are specific for our setup. The question whether direct detection of fluorescence or interferometric detection via extinction yields a better SNR, and under what conditions, has been discussed in the literature in the past few years [70, 141, 146, 147, 148]. So far, an experimental comparison under real conditions has not been shown for a single emitter.

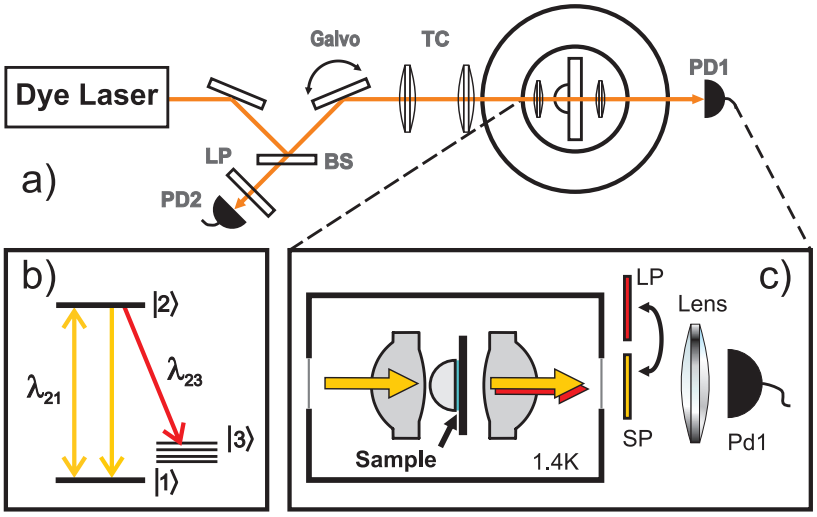

Figure 5.1: Setup to determine the signal-to-noise ratio in single molecule detection via extinction and fluorescence. Both signals are either subsequently recorded on the same detector, PD1, or simultaneously on PD1 and PD2. A long pass filter LP only transmits emission at λ_{23}, a short pass filter SP selects the excitation wavelength. The detection efficiencies of PD1 versus PD2 have been determined via single molecule fluorescence.

5.1.1 Setup

For this experiment we used the same setup and sample as shown in chapter 4. After proper alignment of focus and polarization, a single DBATT molecule can routinely yield a 10% extinction signal. To quantify the signal-to-noise ratio and compare extinction with fluorescence excitation, detector PD1 in the forward direction was used in combination with either an optical short pass (SP) or long pass (LP) filter, respectively. This ensured nearly identical optical configurations for both detection methods. For the experiments with high excitation power, also detector PD2 was used after careful calibration against PD1.

5.2 Detected signals

For the following I assume that all the focused laser light is recollected and directed onto detector PD1. In units of counts per second (cps), the terms of Eq. 5.1 are

$$\begin{aligned}
P_{\text{las}} &= \frac{\epsilon_0 c}{2\hbar\omega}\int_{\Sigma}\left\langle \hat{\mathbf{E}}^{-}_{\text{las}}\cdot\hat{\mathbf{E}}^{+}_{\text{las}}\right\rangle d\Sigma \\
P^{4\pi}_{\text{fluo}} &= \frac{\epsilon_0 c}{2\hbar\omega}\int_{4\pi}\left\langle \hat{\mathbf{E}}^{-}_{\text{m}}\cdot\hat{\mathbf{E}}^{+}_{\text{m}}\right\rangle d\Sigma = \Gamma_1\rho_{22} = \frac{\Gamma_1}{2}\frac{S}{1+S} \\
P^{\Sigma}_{\text{fluo}} &= \zeta P^{4\pi}_{\text{fluo}} \\
P^{\text{res}}_{\text{fluo}} &= \alpha P^{\Sigma}_{\text{fluo}} \\
P^{\text{red}}_{\text{fluo}} &= (1-\alpha)P^{\Sigma}_{\text{fluo}} \\
P_{\text{ext}} &= -\frac{\epsilon_0 c}{2\hbar\omega}\int_{\Sigma} 2\Re\left\langle \hat{\mathbf{E}}^{-}_{\text{las}}\cdot\hat{\mathbf{E}}^{+}_{\text{fluo}}\right\rangle d\Sigma\ .
\end{aligned} \tag{5.2}$$

The quantity $P^{4\pi}_{\text{fluo}}$ gives the total power emitted by the molecule into the 4π solid angle. The parameter ζ signifies the fraction of the total emitted molecular power to that collected into the detection solid angle Σ. In general, one might have to account for total internal reflection and waveguiding in the substrate which influence the angular distribution of the laser light and the molecular emission. ρ_{22} is the population of the excited state, and the on-resonance saturation parameter S is

$$S = \frac{\Omega}{\Gamma_1\Gamma_2}, \tag{5.3}$$

where, as before, Ω is the Rabi frequency defined by $\hbar\Omega = d_{\text{ZPL}}\cdot E_{\text{las}}(\text{O})$. The transition dipole moment d_{ZPL} and the incident electric field $E_{\text{las}}(\text{O})$ at position of the molecule are assumed to be parallel for simplicity here. The factor α is the ratio of the power emitted on the 0-0 ZPL to the total excited state emission, in our case the product of Debye-Waller and Franck-Condon factors. Therefore, $d_{\text{ZPL}} = \sqrt{\alpha}d_{\text{eg}}$ where d_{eg} denotes the dipole moment associated with the total spontaneous emission rate of the excited state given by $\Gamma_1 = d^2_{\text{eg}}\omega^3/(3\pi\epsilon_0\hbar c^3)$. Γ_2 represents the transverse decay rate which equals $\Gamma_1/2$ in the absence of any dephasing. Finally, the quantities $P^{\text{res}}_{\text{fluo}}$ and $P^{\text{red}}_{\text{fluo}}$ represent the portions of the molecular emission into the solid angle Σ that are resonant with the excitation laser and red shifted from it, respectively. Red-shifted refers to the emission into phonon wing and vibrational levels.

Using the definitions of Γ_1 and Ω, one can rearrange the saturation parameter in Eq. (5.3) to read

$$S = \frac{\alpha}{\Gamma_2}\mathcal{K}P_{\text{las}} \ . \tag{5.4}$$

The factor $\mathcal{K}$ in this equation is

$$\mathcal{K} = \frac{d_{\text{eg}}^2 E_{\text{las}}^2(\text{O})}{\hbar^2 \Gamma_1 P_{\text{las}}} \tag{5.5}$$

$$= \frac{\epsilon_0 c E_{\text{las}}^2(\text{O})}{2\hbar\omega_0}\frac{3\lambda^2}{2\pi}\frac{1}{P_{\text{las}}} = \frac{I_{\text{las}}\sigma_0}{P_{\text{las}}} \ , \tag{5.6}$$

where σ_0 is the extrinction cross section of an ideal TLS. $\mathcal{K}$ is a unitless geometrical factor that denotes the ratio of the total power extinguished by a weakly excited two-level system and the incident power. Via I_{las} it depends on the spatial mode of the laser beam and the focusing optics. Reference [83] gives detailed calculations of $\mathcal{K}$ for various illumination geometries and field distributions for a classical dipole. Equation (5.4) separates the properties of the laser beam ($\mathcal{K}$, P_{las}) from the spectroscopic features of the emitter (α, Γ_2).

5.2.1 Fluorescence

The expressions in Eq. (5.2) provide the red shifted fluorescence $P_{\text{fluo}}^{\text{red}}$. The background of such a measurement is solely given by the detector dark counts P_{dark}, assuming that the excitation light is completely rejected by the filters. In the literature on this subject [146, 148, 149], the signal is compared to the noise in the presence of the signal, i.e. on-resonance. Therefore it contains both the rms of the detector dark counts and of the signal itself. The SNR is a matter of convention and it might also be intuitive to define the SNR as the ratio of signal to the noise if the signal is not present. However, I will stick with the conventional definition of fluorescence SNR for now. The total noise then becomes $N_{\text{fluo}} = \sqrt{P_{\text{dark}} + P_{\text{fluo}}^{\text{red}}}$ and the SNR for a fluorescence excitation measurement is

$$\text{SNR}_{\text{red}} = \frac{\mu P_{\text{fluo}}^{\text{red}}}{N_{\text{fluo}}} = \frac{\mu\zeta(1-\alpha)\Gamma_1}{2\sqrt{P_{\text{dark}} + \mu P_{\text{fluo}}^{\text{red}}}}\frac{S}{1+S}. \tag{5.7}$$

where the factor μ was introduced to account for losses (e.g. cryostat windows, filters, etc.) and the detector efficiency. The noise and hence the SNR is governed by the detector dark counts for very weak emitters or when the system is excited with low light intensities. On the other hand, for strong emitters and strong excitation, the dark count noise becomes negligible and the maximum SNR is given by $\text{SNR}_{\text{red}}^{\text{max}} = \sqrt{\mu\zeta(1-\alpha)\Gamma_1/2}$, which occurs in the fully saturated regime.

5.2.2 Extinction

Considering that the solid angle Σ collects all the incident laser light, P_{ext} in Eq. (5.1) must correspond to the total power $P_{\text{fluo}}^{4\pi}$ emitted by the molecule, see Chap.2. A

detection at the wavelength of the excitation light will see the laser power P_{las}, superimposed with a dip of size

$$P_{\text{dip}}^{\text{res}} = P_{\text{ext}} - P_{\text{fluo}}^{\text{res}} = P_{\text{fluo}}^{4\pi} - P_{\text{fluo}}^{\text{res}} = (1-\alpha\zeta)\frac{\Gamma_1}{2}\frac{S}{1+S} \ . \tag{5.8}$$

The extinction term yields a reduction of detected power, whereas the resonance fluorescence of the molecule emitted into Σ gives a positive contribution. The noise on a resonant detection is composed of the shot noise $\sqrt{P_{\text{las}}}$ of the laser power, the laser intensity fluctuations κP_{las} [95], where κ is a proportionality constant, and again $\sqrt{P_{\text{dark}}}$. Since these contributions are statistically independent, the total noise can be written as $N_{\text{res}} = \sqrt{\mu P_{\text{las}} + (\mu\kappa P_{\text{las}})^2 + P_{\text{dark}}}$. The factor μ accounts again for losses and the detection efficiency. Note that in extinction measurements the rms noise is usually evaluated off-resonance. This seems to be due to the fact that, unless highly efficient interaction is achieved, the detected power on-resonance is comparable to the detected power off-resonance. To keep the equations simpler, I will follow this convention in the following[1]. Assuming that intensity fluctuations have been mastered at a sufficient level and that the laser power is much larger than the detector dark counts, the noise is given by the rms of the laser background alone, $N_{\text{res}} \simeq \sqrt{\mu P_{\text{las}}}$. The signal-to-noise ratio for an extinction measurement becomes

$$\text{SNR}_{\text{res}} = \frac{\mu P_{\text{dip}}^{\text{res}}}{N_{\text{res}}} \simeq (1-\zeta\alpha)\frac{\Gamma_1}{2}\sqrt{\frac{\mu\alpha\mathcal{K}}{\Gamma_2}}\frac{\sqrt{S}}{1+S} \ . \tag{5.9}$$

This function has a maximum at S=1. The highest attainable SNR in a shot-noise limited resonant detection is $\text{SNR}_{\text{res}} = \sqrt{\Gamma_1^2\alpha\mathcal{K}\mu/(16\Gamma_2)}$, if we assume $\zeta\alpha \ll 1$.

5.2.3 Power dependence of SNR

The signal-to-noise ratio in extinction detection of a single molecule shows a different behavior than the fluorescence measurement. For low excitation powers both curves increase with $\sqrt{S}$. The exact prefactors $\alpha, \mathcal{K}, \zeta$ as well as P_{dark} and the ratio Γ_1/Γ_2 determine which method will yield a higher SNR. At stronger excitation, when $S \gg 1$, the exctintion SNR decreases with $\sqrt{S}^{-1}$, while the fluorescence SNR saturates at a constant value. This trend is verified in the following experiment for a single DBATT molecule in *n*-tetradecane.

We have excited a single molecule with excitation powers in the range of a few fW up to nW, which corresponded to a measured laser power μP_{las} in between 1000 to 10^9 cps range[2]. To achieve high power measurements on PD1, we attenuated the beam impinging on the detector with calibrated neutral density filters and later corrected accordingly. Our system could perform shot-noise limited detection down to sub Hertz bandwidth over the whole power range presented here.

[1] To be accurate, the rms of the total signal on-resonance should be used in the calculation of the noise, i.e. as $\sqrt{\mu(P_{\text{las}} - P_{\text{dip}}^{\text{res}})}$ as well as the associated intensity fluctuations. Given that we typically see 5-10 % extinction, the correction to the extinction SNR as shown in this text is on the order of 2-5 %

[2] the transmission through the cryostat amounted to 25 %, the APD detection efficiency at 590 nm is roughly 65 %

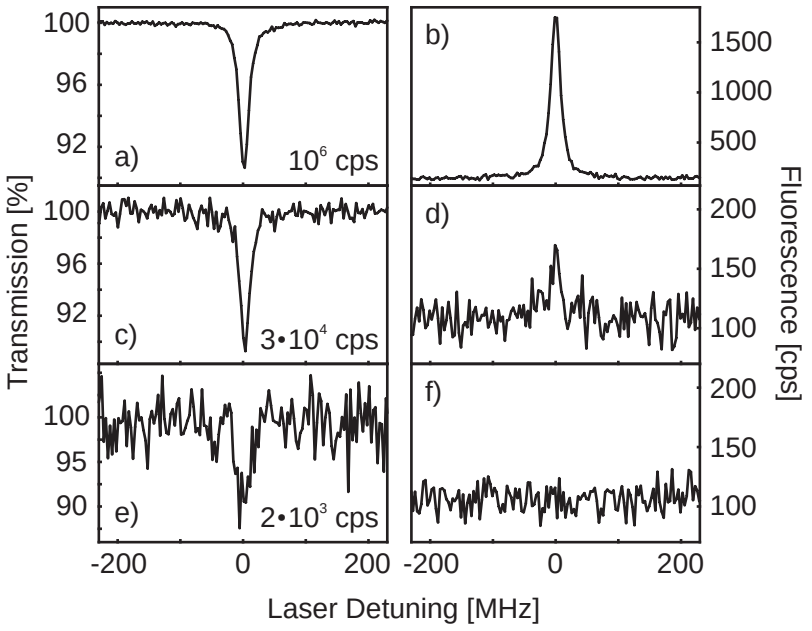

Figure 5.2: Examples of extinction (left side) and fluorescence excitation spectra (right side) of a single molecule at low excitation powers, all scans recorded with one second integration time per pixel on PD1. Marked in the plots is the detected P_{las} in counts per second.

Figure 5.2 displays frequency scans at three different low excitation powers, for each power showing an extinction and fluorescence excitation spectrum of the same molecule, recorded subsequently on PD1 with 1s integration time per pixel. The data was acquired by adding 100 scans of 10ms integration time for each excitation power. This was to correct for possible laser drifts and spectral diffusion of the molecule. When the detected laser power reads 10^6 cps on PD1 (corresponding to an excitation regime well below saturation) both extinction (a) and fluorescence (b) yield comparable spectra. For a detected laser power of 3.2×10^4 cps, the fluorescence of the molecule is hardly above the detector dark count rate of 100 cps. However, the extinction is still easily observable at 10% visibility. Even at an ultra-low illumination level of 2000 cps the extinction signal succeeds in detecting the molecule whereas the fluorescence peak is fully buried under the detector noise, which becomes the main limiting factor for the detection of small fluorescence signals.

The experimental SNR was determined from scans as shown in Fig. 5.2 by dividing the signal resulting from a Lorentzian fit to the data by either the background rms in case of extinction, or by the combined background and signal rms in case of fluorescence. Fig. 5.3 displays the signal-to-noise ratio obtained from the whole excitation power range as a function of saturation parameter and measured laser power μP_{las}. The saturation parameter was independently derived from the power broadened linewidth of fluorescence excitation spectra recorded on PD2. The fluorescence measurements were recorded on two different detectors for the low and high power

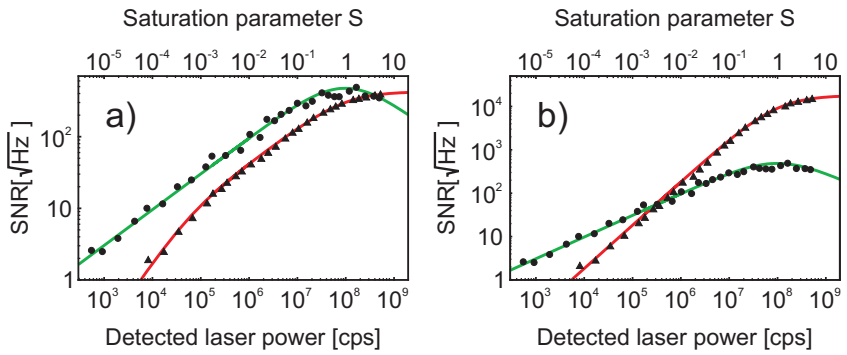

Figure 5.3: The signal-to-noise ratios of the extinction (circles, green lines) and fluorescence (triangles, red lines) measurements as a function of the excitation power and saturation parameter for two different definitions of noise: (a) noise determined from the fluctuations of the signal on resonance, (b) noise evaluated from the fluctuations of the off-resonant background.

experiments. Nevertheless, a careful calibration of the detection efficiencies of PD1 and PD2 with a single molecule fluorescence signal was taken into account to plot both fluorescence datasets in this graph. The red and green curves show simulations of the data according to Eqs. (5.7) and (5.9), respectively. The parameters ($\mu = 0.2$, $\mathcal{K}$=0.5, $\alpha = 0.2$, $\Gamma_2 = \Gamma_1/2, \Gamma_1/2\pi = 17$ MHz and $\zeta = 0.02$) have been derived as follows. The linewidth Γ_2 is determined from low power fluorescence measurements, α is known from characterizations of the molecule/matrix system [22]. A saturation parameter S=1 is is reached at a laser power $\mu P_{\mathrm{las}} = 9.8 \times 10^7$ cps. The quantity $\mathcal{K}/\mu$ can then be derived from Eq. (5.4), and the quantity $\mathcal{K}\mu$ from a fit to the measured extinction SNR data. Finally, ζ is obtained from a fit to the fluorescence SNR curve.

It is evident that in the weak excitation regime where detector dark count becomes considerable, the homodyne advantage of extinction measurements leads to a superior SNR as compared to fluorescence detection. However, it is somewhat surprising that the SNR of extinction measurements wins in the case of stronger excitations up to saturation. Two decades of solid-state single emitter spectroscopy has nearly exclusively relied on fluorescence measurements. The difference here is that, contrary to the conventional experiments, we have achieved a substantial $\mathcal{K}$ by strong focusing. In general, the competition between the performances of fluorescence and extinction measurements is decided by many experimental factors entering Eqs. (5.7) and (5.9). The chosen definition of SNR can also affect the outcome of such a comparison. Next to the given definition, a reasonable alternative measure for the detectability of a single emitter could also be the ratio of the signal to the noise associated with the off-resonant background, i.e. neglecting the fluctuations of the signal. In Fig. 5.3 b) the same experimental data was analyzed according to this latter strategy and was fitted using a correspondingly modified version of Eqs. (5.7) and (5.9). In this intuitive measure, fluorescence detection seems advantageous at higher power.

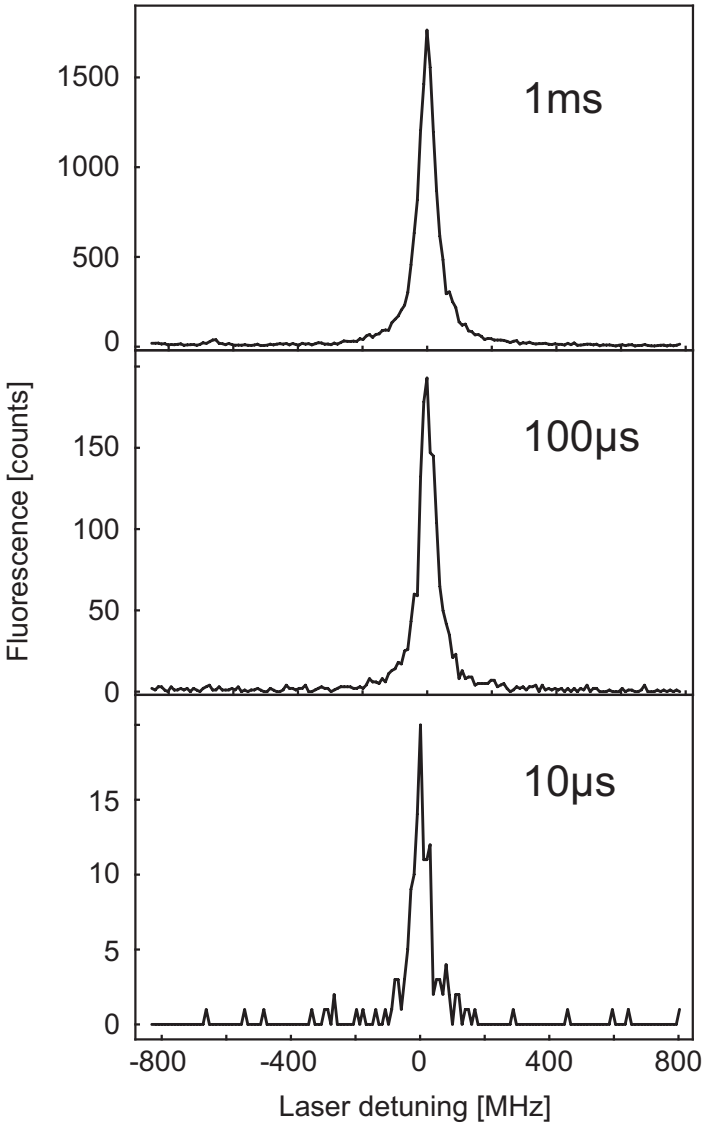

Figure 5.4: Fluorescence excitation spectroscopy. Integration times as indicated.

5.3 Fast detection

The fast detection of a single molecule is interesting for the study of dynamic processes [150, 151]. So far the shortest integration times used for fluorescence excitation is in the range of a few ms [150, 152]. both SNR_{res} and SNR_{red} scale as the square root of the integration time and thus, the comparison between the fluorescence and extinction methods holds for fast and slow measurements alike. Unlike in the case of low excitation power, the detector dark count noise is of no importance for fluorescence detection at short integration times. For 1ms integration time, an average number of 0.1 dark counts per pixel can be expected for our detectors. In this regime, successful detection of a signal is limited only by Γ_1 and the detection efficiency. I will therefore present fluorescence excitation spectra recorded on

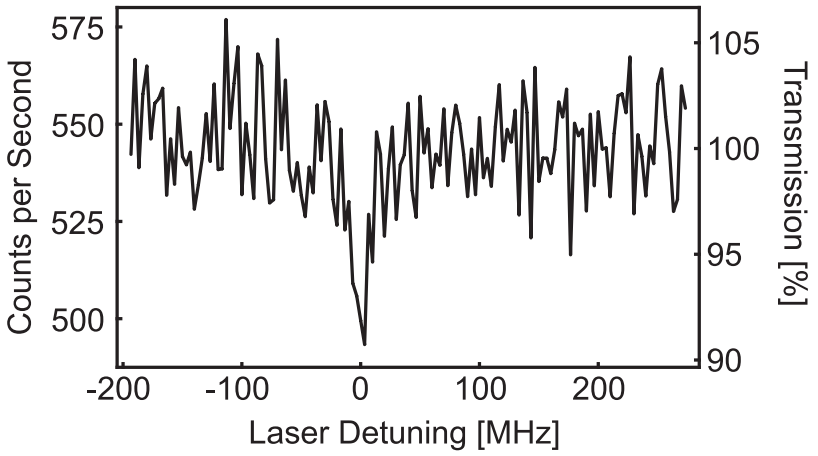

Figure 5.5: Extinction spectrum of a single molecule, recorded with 4s integration time per pixel and an excitation power of 600 aW.

PD2 in the backward direction. Due to the high index SIL material, PD2 detects fluorescence roughly 10 times more efficiently than PD1.

The dye laser is limited in its scanning speed, as a frequency scan is performed by tilting a Brewster plate in the laser cavity. A way to bypass this problem is to use an AOM for frequency tuning. However, this experiment was meant to verify that a single molecule can be detected in very short integration times, so in this case the laser was scanned at a normal rate of about 1 GHz/s, and the avalanche photodiode was read out for only a short time at each frequency pixel. Clearly this system can not be used to resolve any dynamics in the molecular transition lines.

Fig. 5.4 shows fluorescence excitation spectra of a molecule, recorded with 1ms, 100μs and 10μs integration time per pixel on PD2 in the backward direction. The saturation parameter was calculated from the power broadened linewidth to be S=6, and the fluorescence countrate was roughly 1.6 10^6 per second. The dark counts and background only appear as single detection events from time to time in the lowest graph, and the spectrum recorded at 10 μs still holds enough information to derive linewidth, lineshape and intensity.

5.4 Discussion and outlook

The potential of single molecule detection via extinction was not considered after the first experiments showed its feasibility with the application of multiple modulation and lock-in techniques [2, 4]. Here we experimentally verified that, provided an efficient interaction of excitation light and emitter, extinction does not only provide valuable phase information, but shows superior signal-to-noise ratio when working in a shot noise limited regime and below saturation. Fig. 5.5 shows an example where a single molecule is detected under a detected power of just 550 photons per second. This corresponds to an incident power of 600 aW. This spectrum was recorded for four seconds per pixel, but it illustrates that extinction detection can be successful

in a power range where fluorescence would only yield about 1.5 photons in the same measurement time.

The sensitive detection of single molecules via extinction shown in this chapter demonstrates the strength of interferometric detection, especially when working with weak emitters. Extinction detection could become a way to detecting single rare-earth ions in solids. Another application of the efficient excitation and detection is the realization of free-space radiative energy transfer between two distant identical emitters like molecules. Both cases will be discussed more detailed in the outlook chapter of this thesis.

It is important to remark that the efficient excitation presented here also leads to an efficient collection, and fluorescence excitation might be feasible as well for the examples given above. Also, detectors with a lower dark count rate are available and would shift the detection limit for fluorescence excitation to a lower value. However, for such emitters that do not have a high radiative quantum yield, e.g. if quenching is present, extinction keeps its advantage [153].

6 Study of the resonance fluorescence of a single molecule

Section 1.3 introduces the phenomenon of resonance fluorescence, its coherent and incoherent components and their intensity dependence. Resonance fluorescence, the emission of a two-level system at the near-resonant excitation wavelength, has been studied extensively in gaseous systems [51]. Solid state systems like molecules, quantum dots and NV-centers in diamond are usually excited into a higher-lying electronic or vibrational state, and the emission filtered via long- or bandpass optics [154]. Resonant fluorescence is hard to observe in these systems because of spurious scattering of the excitation light from sample structures and impurities. Recently, the resonance fluorescence of quantum dots in waveguide structures was observed and its intensity correlation studied by Müller et al. [48, 72]. In those experiments, self-assembled quantum dots were grown between two Bragg reflectors. The excitation light is inserted into a wave-guide mode between the mirrors, and the resonance fluorescence is extracted perpendicular to the excitation through the top mirror. In this respect the experiments in [48, 72] resemble the first observations of resonance fluorescence in atomic beams, as explained e.g. in [61].

Here I will describe the study of both the coherent and incoherent components of the resonance fluorescence of a single DBATT molecule in *n*-tetradecane, over several orders of magnitude from the classical oscillator regime to the nonlinear Rabi oscillation regime. Extinction measurements give access to the coherent emission, whereas the efficient light-molecule interaction achieved in our setup makes the extraction of the incoherent component possible by polarization filtering.

6.1 Coherent resonance fluorescence

In the limit of weak resonant excitation and in the absence of dephasing, the resonance fluorescence of a two-level system is purely elastic and coherent [40, 42]. With increasing excitation intensity, this coherent component of the resonance fluorescence is predicted to evolve with the saturation parameter S according to the formula $S/(1+S)^2$, shown in Fig. 1.4. Here we want to experimentally determine the amount of coherent emission by a single molecule as a function of excitation power.

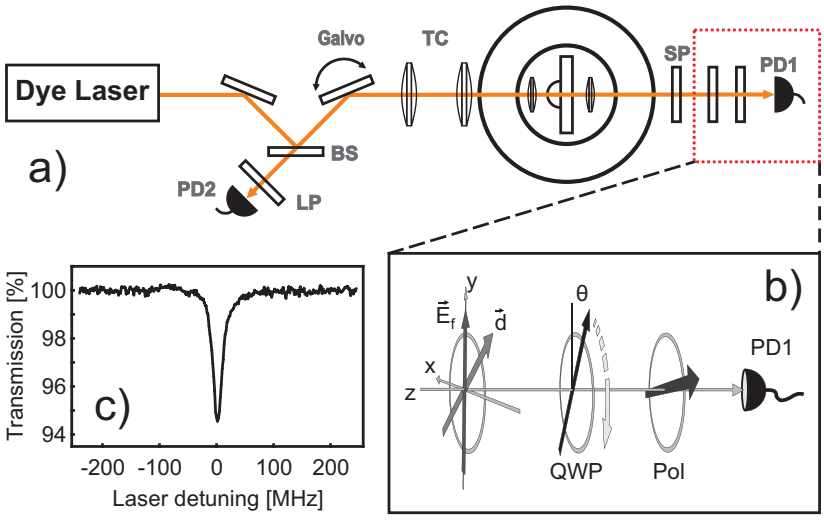

Figure 6.1: Setup to determine the coherent emission of a single molecule from the total detector signal. The combination of quarter wave plate (QWP) and linear polarizer (Pol) allows for a controlled introduction of a phase shift between molecular emission and excitation light. b) shows the angular orientations of the molecular dipole, QWP and Pol, when the excitation laser light polarization is set to zero degrees along the y-axis. c) shows a transmission spectrum of the studied molecule at low excitation power and without QWP and polarizer in place.

6.1.1 Experimental design

The extinction term in Eq. (2.8) contains the field of the molecule's coherent radiation, and therefore the intensity dependent coherent emission can be studied by recording extinction spectra at different excitation powers without changing the geometry of the illumination. However, in addition to the interference signal, a transmission spectrum also contains both the coherent and incoherent components of the resonance fluorescence term P_{21}, as well as parts of the phonon wing emission.

Here I will show that it is possible to separate the total detector signal into its individual components by influencing them in a controlled manner. We do this by introducing a variable phase shift between the molecular emission and the excitation field. This leads to an asymmetric shape of the extinction spectrum, which is then fitted as a sum of dispersive and absorptive Lorentzian functions with Eq. (4.1). Note that the dispersive component can only arise through interference between the coherent field and the excitation field, whereas the Lorentzian component contains a purely emissive fluorescence part from P_{21} and a destructive or constructive interference part from P_{intf}. From the knowledge of the applied phase shifts, we can then determine all three parameters C_{21}, C_{intf} and P_0 of Eq. (2.8) quantitatively and thus the absolute value of the coherent resonance fluorescence.

6.1.2 Setup

As illustrated by Fig. 6.1 b), for this experiment we have introduced a quarter waveplate (QWP) and a polarizer in the detection path of PD1 at the position marked by the dotted red box in Fig. 6.1 a). We set $\mathbf{E}_{\mathrm{inc}}$ at 45° with respect to the transition dipole moment of the molecule and at 80° with respect to the axis of the polarizer. After traversing the QWP, the amplitudes and phases of $\mathbf{E}_{\mathrm{inc}}$ and $\mathbf{E}_{\mathrm{m}}$ have evolved differently, thus changing the relative phase ϕ in Eq. (2.8) as well as the amplitudes of the excitation field, resonance fluorescence and extinction terms. To extract the absolute value of the coherent emission, the signal on PD1 was recorded for several different QWP positions at each incident power P_0. The polarization of the incident light, the molecular orientation ψ_{m} and the polarizer orientation ψ_{P} remained constant over the course of the experiment. The value Γ_{eff} for each power is determined from the signal on PD1, or independently from the simultaneously recorded fluorescence excitation spectra on PD2.

This experiment is very similar to the experiment explained in Sec. 4.4. However, we used a combination of QWP and polarizer in order to cause a stronger dispersive part of the spectrum which is necessary to determine C_{intf} with higher accuracy. Also, this way we avoided the setting where the polarizer is fully crossed with excitation or molecular emission polarization, and residual ellipticities can cause artefacts.

6.1.3 Determining the coherent part of the emission

The derivation of the detected powers of the incident light, resonance fluorescence and the interference term follows closely the polarizer experiment in Sec. 4.4. We start by giving the unit vectors of the excitation field, the molecular emission, both with small ellipticities, as well as the polarization vector and QWP Jones matrix

$$\hat{\mathbf{E}}_{\mathrm{inc}} = \mathcal{E}_{\mathrm{inc}} \begin{pmatrix} 1 \\ 0 \end{pmatrix} , \quad \hat{\mathbf{E}}_{\mathrm{m}} = \mathcal{E}_{\mathrm{m}} \begin{pmatrix} \cos\psi_{\mathrm{m}} \\ \sin\psi_{\mathrm{m}} \end{pmatrix}$$
$$\hat{\mathbf{P}} = \begin{pmatrix} \cos\psi_{\mathrm{p}} \\ \sin\psi_{\mathrm{p}} \end{pmatrix} , \quad \mathbf{Q_0} = \begin{pmatrix} 1 & 0 \\ 0 & i \end{pmatrix} .$$

The ellipticity matrix $\mathcal{E}$ was defined in Sec. 4.4. The plate rotated by an angle θ with respect of the y- axis is given by

$$\mathbf{Q} = \mathbf{T}(\theta)\mathbf{Q}_0\mathbf{T}^{\mathrm{T}}(\theta) = \begin{pmatrix} c^2 + is^2 & (1-i)cs \\ (1-i)cs & s^2 + ic^2 \end{pmatrix} \tag{6.1}$$

$$\mathbf{T}(\theta) = \begin{pmatrix} c & -s \\ s & c \end{pmatrix} , \quad c = \cos\theta , \quad s = \sin\theta . \tag{6.2}$$

An additional offset depends on the way the QWP is built into the rotation stage and is experimentally accessible. In this experiment, the values for ψ_{P} and ψ_{m} are fixed. In the presence of the QWP and polarizer, the contributions of Eq. (2.8) can

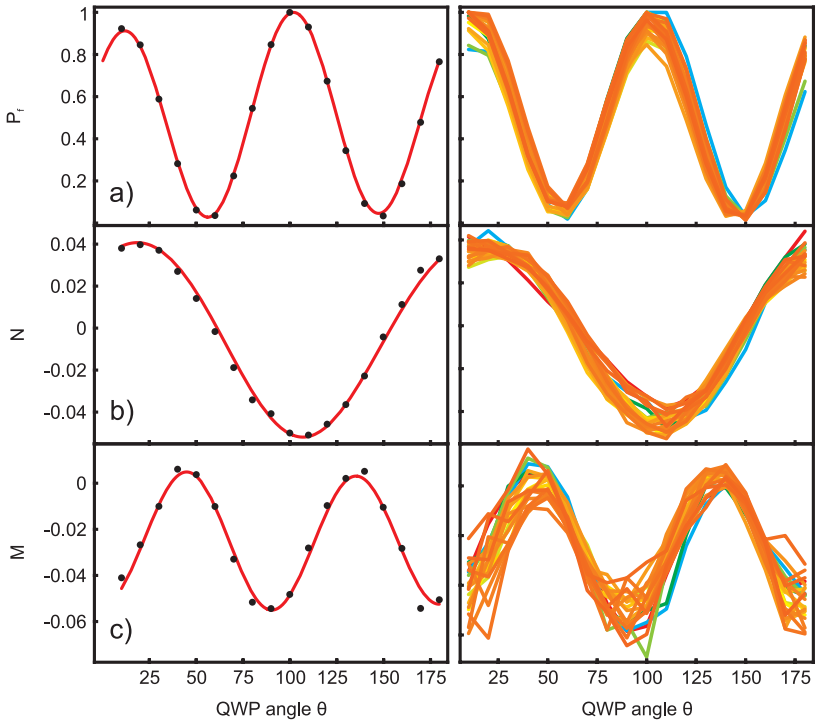

Figure 6.2: Dependence of P_{inc}, $\mathcal{M}$ and $\mathcal{N}$ from the QWP angle θ. The left side shows three examples for a given incident power, normalized by the maximum value of P_{inc} and the corresponding fits with Eq. (6.5). The right side shows that the respective curves for 25 different P_0 over 3 orders of magnitude all collapse on a "mastercurve" when divided by P_0. This demonstrates that the θ-dependence of all three parameters is independent on the excitation intensity.

be identified as

$$\begin{aligned}
P_{\mathrm{inc}} &= P_0|\hat{\mathbf{P}}\cdot\mathbf{Q}\hat{\mathbf{E}}_{\mathrm{inc}}|^2 = \frac{P_0}{4}\left(2+\cos(2\psi_{\mathrm{P}})+\cos(2\psi_{\mathrm{P}}-4\theta)\right)\ , \qquad P_0 = \varsigma|g|^2E_0^2 \\
P_{21} &= C_{21}|\hat{\mathbf{P}}\cdot\mathbf{Q}\hat{\mathbf{E}}_{\mathrm{m}}|^2\cos^2\psi_{\mathrm{m}}P_0\frac{\Gamma_2^2}{\Delta^2+\Gamma_{\mathrm{eff}}^2} \\
P_{\mathrm{intf}} &= -2C_{\mathrm{intf}}\cos\psi_{\mathrm{m}}P_0\Re\left\{\left(\hat{\mathbf{P}}\cdot\mathbf{Q}\hat{\mathbf{E}}_{\mathrm{inc}}\right)^*\left(\hat{\mathbf{P}}\cdot\mathbf{Q}\hat{\mathbf{E}}_{\mathrm{m}}\right)e^{i\phi}\left(\Delta-i\Gamma_2\right)\right\}\frac{\Gamma_2}{\Delta^2+\Gamma_{\mathrm{eff}}^2} \\
&= -2C_{\mathrm{intf}}\cos\psi_{\mathrm{m}}P_0|\hat{\mathbf{P}}\cdot\mathbf{Q}\hat{\mathbf{E}}_{\mathrm{inc}}||\hat{\mathbf{P}}\cdot\mathbf{Q}\hat{\mathbf{E}}_{\mathrm{m}}|\frac{\Gamma_2\left(\Delta\cos\Phi+\Gamma_2\sin\Phi\right)}{\Delta^2+\Gamma_{\mathrm{eff}}^2}\ , \qquad (6.3)
\end{aligned}$$

where P_0 is the excitation power and ϕ is the phase of the extinction signal, both without QWP and polarizer. The phase of the extinction signal after insertion of QWP and polarizer becomes $\Phi = \arg\left(\left(\hat{\mathbf{P}}\cdot\mathbf{Q}\hat{\mathbf{E}}_{\mathrm{inc}}\right)^*\left(\hat{\mathbf{P}}\cdot\mathbf{Q}\hat{\mathbf{E}}_{\mathrm{m}}\right)\mathrm{e}^{\mathrm{i}\phi}\right)$.

Fitting procedure

We write the detected signal analogously to Eq. (4.1) as the sum of purely Lorentzian and dispersive signals

$$P_{\text{total}} = P_{\text{inc}} + \frac{\Gamma_2(\mathcal{M}\Gamma_2 + \mathcal{N}\Delta)}{(\Delta^2 + \Gamma_{\text{eff}}^2)} \ . \tag{6.4}$$

Comparison with Eq. (6.3) yields

$$\begin{aligned} P_{\text{inc}} &= P_0 |\hat{\mathbf{P}} \cdot \mathbf{Q}\hat{\mathbf{E}}_{\text{inc}}|^2 \\ \mathcal{N} &= -2C_{\text{intf}} \cos\psi_{\text{m}} P_0 \Re\left\{ \left(\hat{\mathbf{P}} \cdot \mathbf{Q}\hat{\mathbf{E}}_{\text{inc}}\right) \left(\hat{\mathbf{P}} \cdot \mathbf{Q}\hat{\mathbf{E}}_{\text{m}}\right) e^{i\phi} \right\} \\ \mathcal{M} &= C_{21} \cos^2\psi_{\text{m}} P_0 \left|\hat{\mathbf{P}} \cdot \mathbf{Q}\hat{\mathbf{E}}_{\text{m}}\right|^2 \\ &\quad -2C_{\text{intf}} \cos\psi_{\text{m}} P_0 \Im\left\{ \left(\hat{\mathbf{P}} \cdot \mathbf{Q}\hat{\mathbf{E}}_{\text{inc}}\right) \left(\hat{\mathbf{P}} \cdot \mathbf{Q}\hat{\mathbf{E}}_{\text{m}}\right) e^{i\phi} \right\} \ . \end{aligned} \tag{6.5}$$

One can see that $\mathcal{M}$ and $\mathcal{N}$ differ in their dependence on the angle θ. For each of in total 25 excitation powers P_0, we scanned the laser frequency and fitted the recorded spectra with Eq. (6.4) for 18 different θ. The result of this fit is $P_{\text{inc}}(\theta)$, $\mathcal{M}(\theta)$ and $\mathcal{N}(\theta)$. The left side of Fig. 6.2 shows an example all three curves for a specific excitation power, normalized to the maximum value of $P_{\text{inc}}(\theta)$. Equation (6.5) states that all three curves are linearly dependent on P_0, and one important finding is that after division by the maximum of $P_{\text{inc}}(\theta)$, the experimental $P_{\text{inc}}(\theta)$, $\mathcal{M}(\theta)$ and $\mathcal{N}(\theta)$ curves do not depend on the excitation intensity anymore. This is shown in Fig. 6.2 for all values of P_0 between 5 pW and 10 nW, and verifies the theoretical treatment.

The two coefficients C_{21} and C_{intf} can be individually determined for each laser power by fitting Eq. (6.5) on the $\mathcal{M}(\theta)$ and $\mathcal{N}(\theta)$ curves. The left panel of Fig. 6.2 displays a sample of such a fit. The fixed parameters ψ_{P}, ψ_{m} and ϕ, as well as an offset of the QWP zero-position and small ellipticities in the molecular emission and excitation field introduced by $\mathcal{E}$ can be determined from a fit to the $P_{\text{inc}}(\theta)$, $\mathcal{M}(\theta)$ and $\mathcal{N}(\theta)$ "mastercurve" determined from a mean of all experimental curves in Fig. 6.2, using starting parameters like the experimentally set and verified molecular orientation and polarizer setting. The results are

$$\begin{aligned} C_{\text{intf}} &= 0.046 \pm 0.003 \\ C_{21} &= 0.007 \pm 0.002 \ . \end{aligned}$$

C_{21} is very small and the relative error in its determination is large. This could be improved by rejecting a larger portion of the excitation light with ψ_{P} closer to 90°. However, this can also lead to a larger error due to residual ellipticities in the excitation field. Since C_{21} is not needed for the calculation of P_{coh}, we did not further optimize the accuracy of its determination.

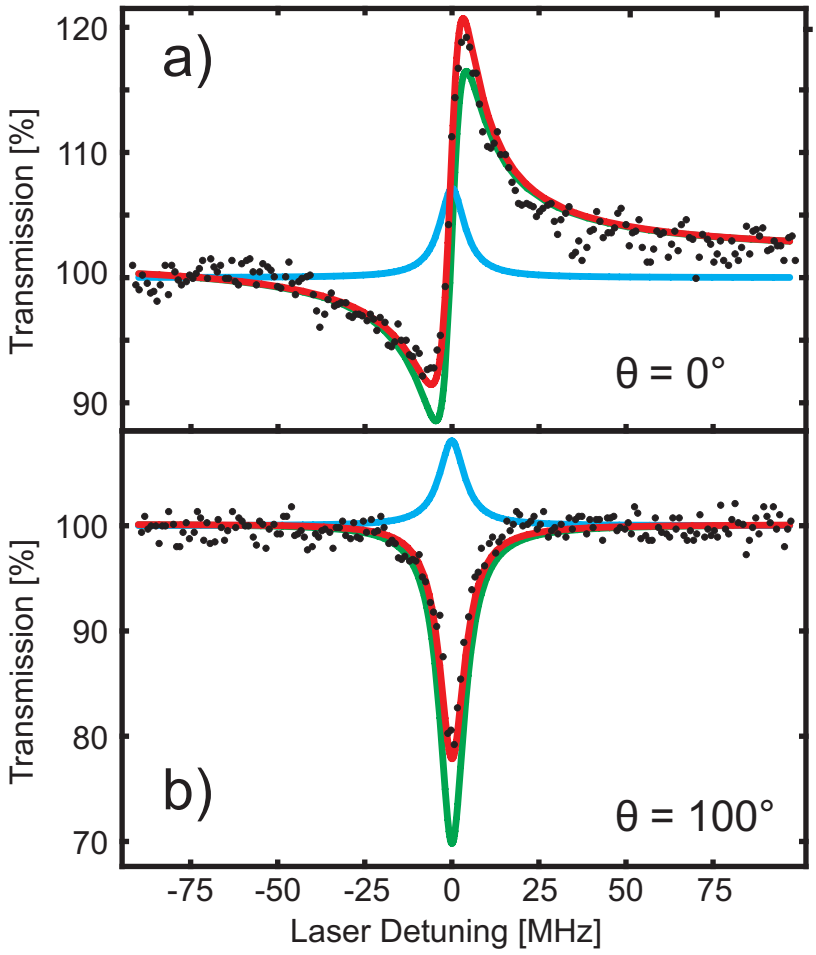

Figure 6.3: Decomposition of P_{det}, the total detected signals on PD1 for two different QWP positions θ according to the analysis explained in the text. The red curve is the fit to the experimental data, the green curve is the pure extinction term P_{intf}, and the blue curve the pure emission term P_{m}.

Decomposition of the total detected signal

The knowledge of C_{intf} and C_{21} lets us calculate the three components of the detected signal for a given QWP position and incident power. This is a simulated decomposition of the total signal which is compared with the experimental data for the specific QWP position. The symbols in Figs. 6.3 display two examples of such an analysis for an incident power of 150 pW. I have chosen two examples where the resonance fluorescence term after transversing he QWP and polarizer becomes comparable to the interference term. The blue and the green spectra show the molecular fluorescence intensity P_{21} and the interference components P_{intf}, respectively, calculated for the specific QWP and Pol positions using the determined C_{intf} and C_{21}. The red curve is the sum of the two calculated components. In case of Fig. 6.3 a), the addition of the P_{21}-term has resulted in a final asymmetric dispersive shape

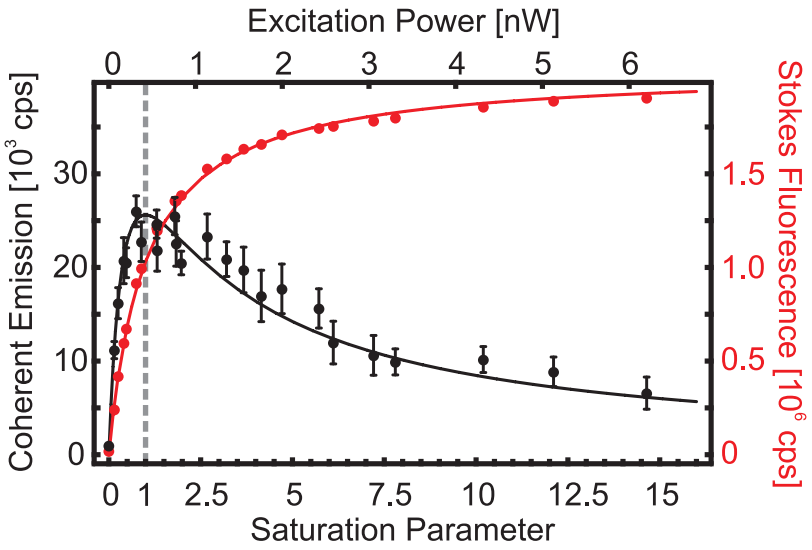

Figure 6.4: The solid black curve displays the theoretically predicted behaviour of the coherent part of the resonance fluorescence as a function of the laser excitation power, also expressed in terms of the saturation parameter S. The red and black symbols plot the experimentally measured Stokes shifted and coherent parts of the emission, respectively. The error bars were determined by propagating errors based on the confidence intervals of the fit parameters P_0 and C_{intf}.

whereas in Fig. 6.3 b), the peak of 8% associated with the P_{21}-term has reduced a 30% dip of the P_{intf}-term to yield a total observable dip of 22%. The agreement of the calculated red curve with the actual recorded data is very good.

Coherent emission

The absolute power of coherent emission can be calculated from the knowledge of C_{intf} and Eq. (2.9) for any polarizer and QWP position

$$P_{\mathrm{coh}} \;=\; P_0 C_{\mathrm{intf}}^2 |\hat{\mathbf{P}} \cdot \mathbf{Q}\hat{\mathbf{E}}_{\mathrm{m}}|^2 \cos^2 \psi_{\mathrm{m}} \frac{(\Delta^2 + \Gamma_2^2)\,\Gamma_2^2}{(\Delta^2 + \Gamma_{\mathrm{eff}}^2)^2} \;. \tag{6.6}$$

We measured the intensity dependence of the coherent resonance fluorescence by varying the excitation intensity between 5 pW and 10 nW. The black symbols in Fig. 6.4 show the power of the coherent emission of a single molecule under resonant excitation, extracted according to the procedure described above. We obtain an excellent agreement between the measured and the theoretical data with only a scaling parameter for the absolute power. The red dots in Fig. 6.4 show the conventional saturation curve obtained from the fluorescence excitation signal recorded simultaneously on PD2 as a direct measure of the excited state population, also in excellent agreement with the function $S/(1+S)$ displayed by the solid red

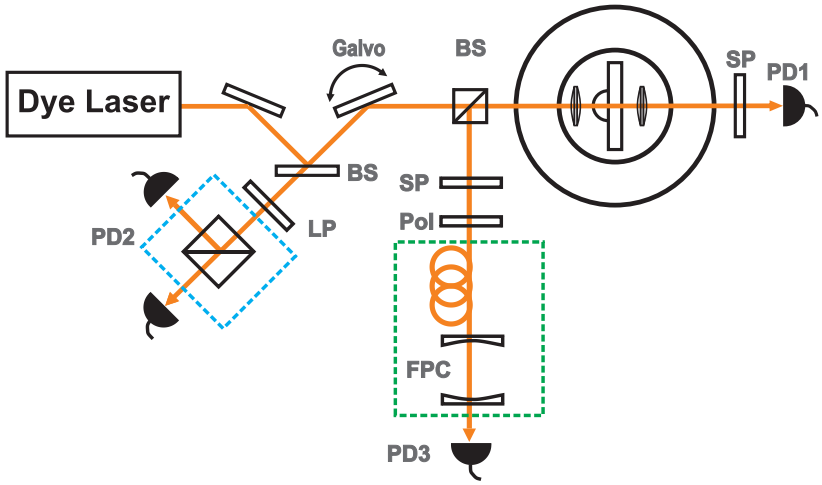

Figure 6.5: Setup for the measurement of the resonance fluorescence spectrum of a single molecule. In the backward direction a 50:50 beamsplitter directs part of the molecular emission through a linear (and crossed polarizer), a multimode optical fiber and a Fabry-Perot cavity (FPC) for spectral filtering, For details see the text.

curve. S was determined independently by analyzing the measured linewidths of fluorescence excitation spectra, where $S = 1$ corresponds to a power broadened FWHM linewidth of $\sqrt{2}\Gamma_1$.

6.2 Incoherent emission, measurement of the Mollow triplet

The data in Fig. 6.4 clearly show that the coherent resonance fluorescence diminishes under strong excitation. This means that the interference between the laser beam and the molecular emission is reduced, and the dip in the transmission spectra recorded on PD1 gradually disappears. In parallel to this process, the inelastic component of the resonance fluorescence is expected to increase and give rise to the Mollow triplet [49] as shown in Chap. 1. The Mollow triplet has been examined in various gaseous systems [51, 61], but its direct observation has turned out to be elusive in the solid state. An indirect observation of dresses states in strongly driven single quantum dots has been realized via the measurement of first-order autocorrelation functions of the quantum dots resonance fluorescence [72]. In a second experiment, the absorption of a weak probe pulse was monitored while a quantum dot was strongly driven with a resonant pump pulse, which lead to the observation of the so-called Mollow absorption triplet [74], which was previously also studied in gaseous systems [155].

6.2.1 Setup

To record the spectrum of resonance fluorescence, we used the detection path in reflection that leads to PD3 in Fig. 6.5. The molecular fluorescence was sent through a short-pass filter to cut out the Stokes shifted fluorescence, while transmitting light at λ_{21} and part of the broad phonon wing of the zero phonon line. In order to completely suppress any backreflected excitation light, we oriented the polarization direction of $\mathbf{E}_{\mathrm{inc}}$ at 45° to the molecular dipole. A linear polarizer in the detection path was at 90° to $\mathbf{E}_{\mathrm{inc}}$ and filtered out the background scattering of the laser light with a ratio of 300:1. The remaining light was coupled into a multimode optical fiber with a core diameter of 50 μm for convenience of handling, especially switching between different detection setups. Another advantage of the fiber coupling is that it additionally rejects part of the scattered laser light that is not well collimated. The output of the fiber was sent to a home-built Fabry-Perot cavity (FPC) with a free spectral range of 356 MHz and transmission of approximately 15%. As shown by the lowest spectrum in Fig. 6.7 a), an instrumental linewidth of about 14 MHz was measured when only reflected laser light was coupled to the resonator. Despite polarization filtering of the fluorescence, the background laser scattering was of the same order of magnitude as the molecular fluorescence at the large saturation parameters that we worked with in the final experiment. However, the transmitted laser light could be exploited for calibrating the frequency axis of each FPC scan, and correct for thermal drifts of the cavity length.

Fig. 6.6 shows the signal of all three detectors in the setup, recorded simultaneously at a moderate excitation power. PD1 records the extinction spectrum, in the example shown here the visibility is close to 7 %. PD2 is positioned behind an optical long-pass filter and records a fluorescence excitation scan or P_{23} as shown in b). Finally, PD3 detects the resonance fluorescence P_{21} behind a short-pass filter, but also some residual backscattered laser light and its interference with the coherent component of the resonance fluorescence. In the scan presented in Fig. 6.6 c) one can see a small asymmetry caused by this interference. Also in the QD resonance fluorescence experiments by Müller et al. [72], a slight asymmetry of the lineshape is visible, although the amount of excitation light leaking out of the waveguide mode should in principle be negligible. In our case the signal-to-background ratio on PD3 can reach values of up to 15:1.

6.2.2 Recording emission spectra

Experimental procedure

The FPC transmission could be scanned using piezo stacks that controlled its length, and this way a spectrum of the sum of molecular emission and residual backscattered laser light was recorded. To correct for eventual thermal drifts of the cavity, spectral jumps of the molecule or of the laser emission, the experiment was repeated several times with a relatively short integration time per pixel. Each time, a fluorescence excitation spectrum was measured on PD2 to locate the molecular resonance frequency, then the laser frequency was set to this value and the FPC

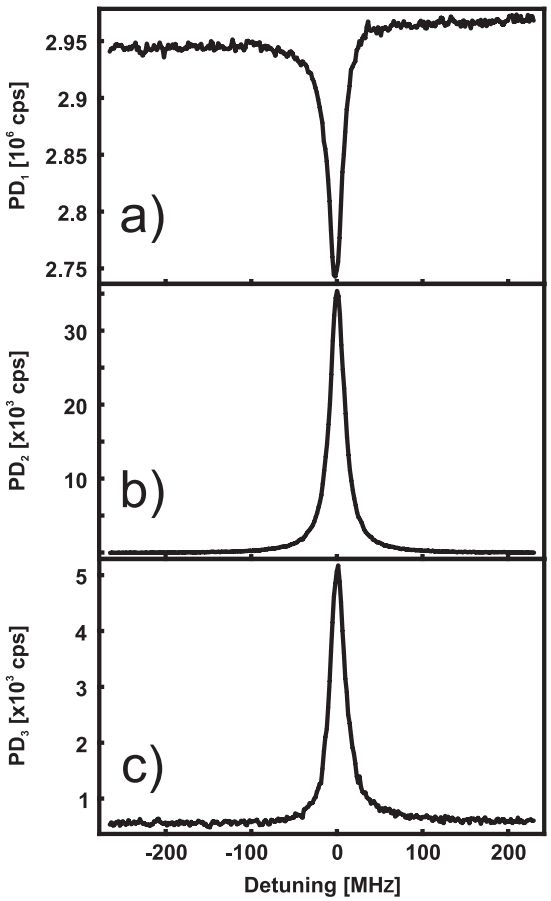

Figure 6.6: Recorded signals on all detectors in Fig. 6.5 as the laser frequency is swept over the molecular resonance. a) is PD1 which records an extinction spectrum, b) or PD2 records a typical fluorescence excitation spectrum behind an optical long-pass filter, and c) shows the signal on PD3 behind an optical short-pass filter and without the FPC in the beam path. The signal is mainly given by the resonance fluorescence of the molecule, and some interference with residual laser light.

frequency was scanned during 12 s. This procedure was repeated for a total acquisition time of 20-40 minutes per spectrum. Fig. 6.7 b)-h) show a series of emission spectra recorded while exciting a molecule on resonance. As the excitation intensity was raised from about 1 to 8 W/cm^2, side bands appeared in the molecular emission spectrum with increasing frequency separation.

Linewidth, dephasing

The linewidth of the fluorescence excitation spectra recorded for this molecule on PD2 behaves as expected even at saturation parameters of S=75. Figure 6.8 plots the squared measured fluorescence FWHM versus the squared Rabi frequency as

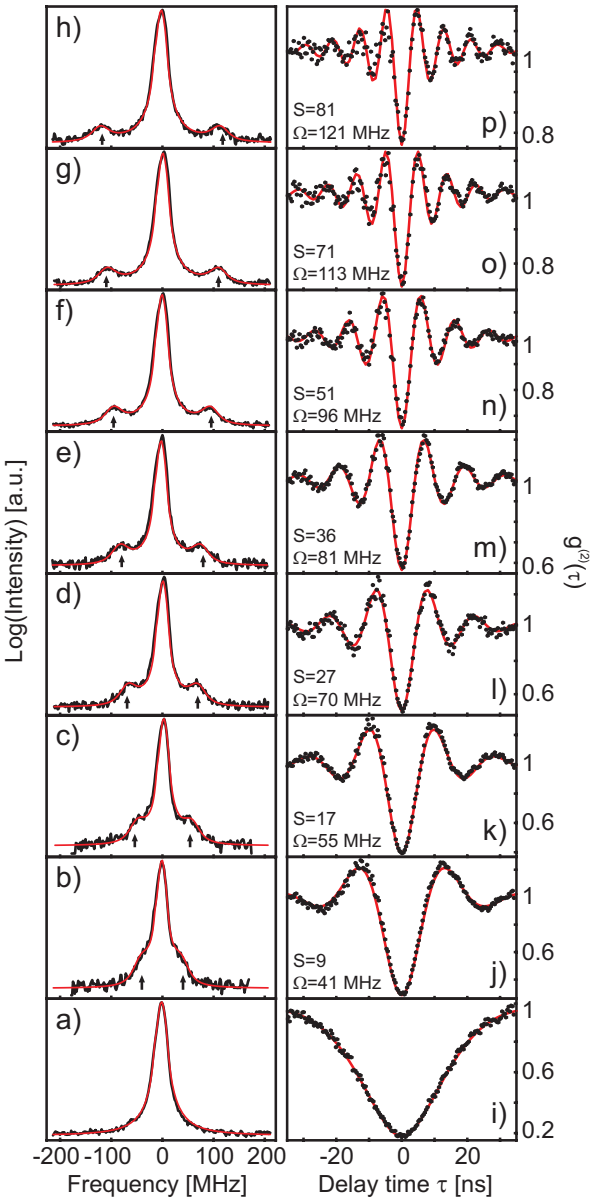

Figure 6.7: a) Transmission of the FPC under laser illumination. The red curve is a linear combination of Lorentzians as an approximation for the FPC filter function. b-h) Series of resonance fluorescence emission spectra (black) recorded by scanning the FPC for increasing excitation intensities. The red curves are the calculated spectra convolved with the FPC filter function of a). i) Second-order autocorrelation function of the single molecule under weak excitation, displaying photon antibunching. j-p) Series of autocorrelation functions recorded at the same time as the spectra shown in b-h). The Rabi frequency Ω extracted from the fit (red curves) to the $g^{(2)}(\tau)$ data is indicated in each figure together with the corresponding saturation parameter S, and as the black arrows in b-h)

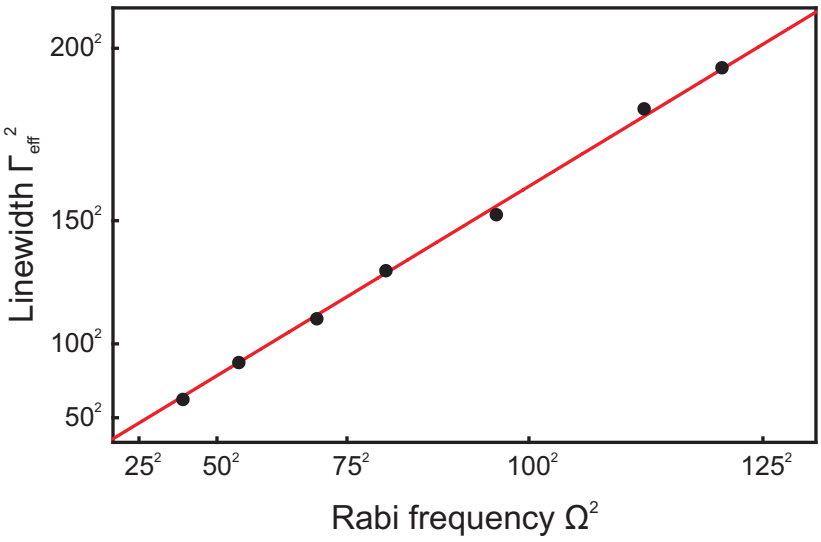

Figure 6.8: Squared fluorescence excitation linewidth versus squared Rabi frequency. These two values are extracted from the spectra on PD2 and the $g^{(2)}$ measurements, respectively. The linear dependence is in perfect agreement with Eq. (1.9) and verifies that even at high excitation intensities, the molecule is not broadened by additional light-induced dephasing processes. The figure is analog to Fig. 4.4, but for this specific molecule.

extracted from the g(2)-measurements explained below. $\Gamma_2/2\pi$ can be extrapolated to be 9.5 MHz which is in good agreement with the natural lifetime limited value of $\Gamma_1/2\pi$=16 MHz. For the linear fit, a triplet-correction parameter of K=1.14 was included.

Shape of the Mollow fluorescence triplet

The emission spectra in Fig. 6.7 b)-h) are plotted on a logarithmic scale to enlarge the visibility of the sidebands, since the central peak is overpowered by the narrow-band backscattered laser light at $S \gg 1$. The slight asymmetry of the spectrum is caused by the transmission function of the FPC, and also visible in Fig. 6.7 a). The sidebands can be independently fitted, approximately with a Lorentzian function, which gives a linewidth of 35-40 MHz. Recalling Sec. 1.3, the FWHM of the Mollow sidebands in the absence of dephasing is $3/2\Gamma_1 = 24$ MHz. For the molecule under study, $\Gamma_2^*/2\pi \simeq 1.5$ MHz and the sideband linewidth is expected to have a FWHM of $3\Gamma_2 = 28.5$ MHz. Convolution with the FPC filter function yields a linewidth of about 35 MHz, which is in good agreement with the measured value. During the cavity scans, the laser remained stationary on the molecular resonance frequency. Potential small frequency shifts of the laser may lead to a detuning from resonance, and correspondingly a larger separation of the sidebands from the central peak [62]. However, these frequency shifts are estimated to be below a natural linewidth, given

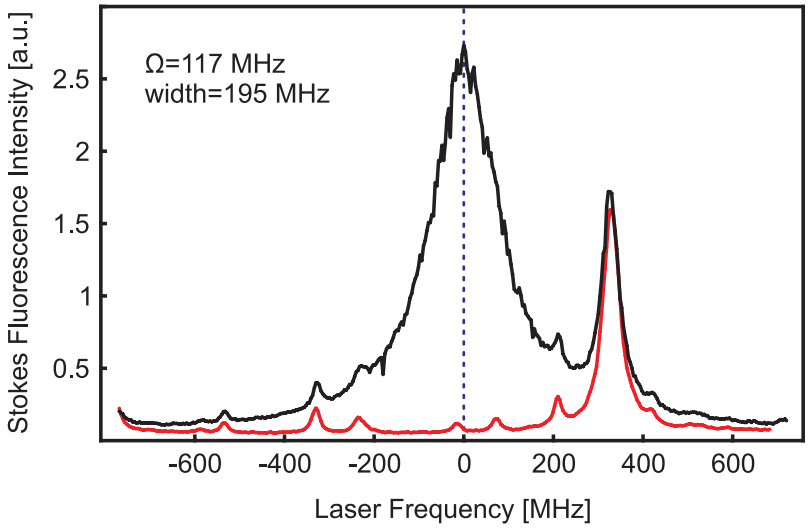

Figure 6.9: Signal on PD2 for two consecutive laser scans during the Mollow-triplet measurements at Ω=121 MHz. The molecule underwent a spectral jump after the first scan (black), revealing the background fluorescence due to neighboring molecules on the second scan (red). On resonance, this background fluorescence is negligible.

a constant fluorescence intensity trace measured on PD2. Such shifts should therefore not result in a washing-out of the triplet structure. Occasional spectral jumps of the molecule on the other hand resulted in cavity scan traces where the molecule suddenly switched off. These traces where used as a measure for the background fluorescence level, as shown in the next section.

6.2.3 Determination of the Rabi frequency

To obtain an independent measure of the Rabi frequency, we split the Stokes-shifted fluorescence on PD2 via a beam splitter onto two photodetectors as sketched in the blue dotted box in Fig. 6.5 c). By using the common Hanbury Brown-Twiss start-stop scheme [65], we recorded the intensity correlation function $g^{(2)}(\tau)$ [40] simultaneously to each measurement presented in Figs. 6.7b-h. The results are plotted in Fig. 6.7 j)-p). Figure 6.7 i) confirms that, as expected, we observed antibunching at low intensities. However, as the excitation was made stronger, $g^{(2)}(\tau)$ underwent Rabi oscillations [75].

The autocorrelation functions were fitted using Eq. (1.15). This way we determined the values of the damped Rabi frequencies Ω_Γ for each case. These values together with the corresponding saturation parameters S are indicated in Fig. 6.7 j)-p), and are marked with arrows in Fig. 6.7 b)-h).

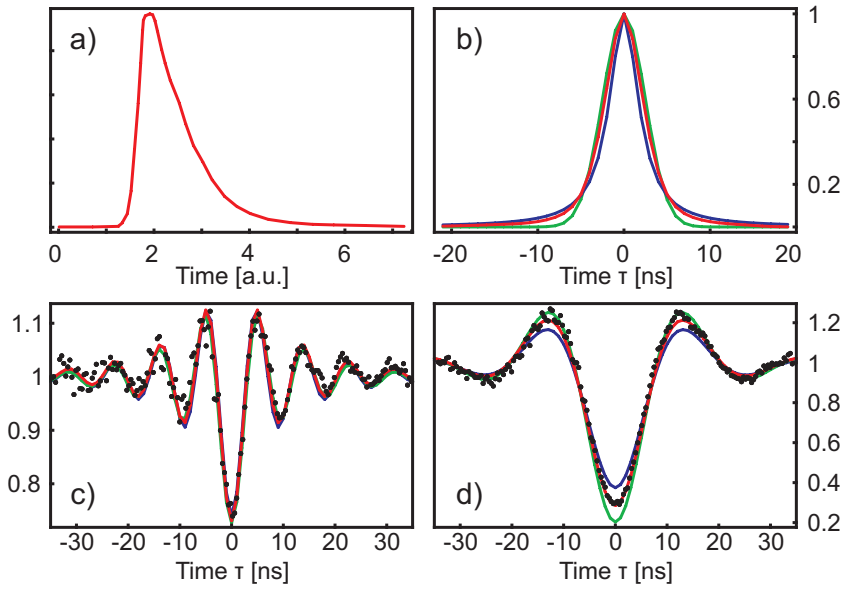

Figure 6.10: a) typical SPCM-AQR single detector response function as derived from [102]. b) two-detector response functions obtained after self-convolution of a Gaussian (blue), Lorentzian (green) and the mixed function from a) (red). These functions were used to simulate $g^{(2)}$ measurements with limited timing resolution. c) and d) $g^{(2)}$ measurements for Ω_Γ=121 and 41 MHz, together with a simulated $g^{(2)}$ function convoluted with the two-detector response curves shown in b). In c) all simulated curves fall together. For details see text.

$g^{(2)}$ background

One can see that $g^{(2)}(0)$ in Fig. 6.7 j)-p) increases with increasing saturation. One reason is the nonzero background that increases linearly with the excitation intensity. We have monitored the background counts during occasional spectral jumps of the molecule and assess the background to range between 2% and 5% of the molecular fluorescence. An example is plotted in Fig. 6.9 which shows two consecutive laser scans at high excitation intensity over the molecule under study, between which the molecule undergoes a spectral jump. Other molecules in spectral proximity are also excited during the laser frequency scan. However, the dotted line marks the position at which the laser frequency is kept constant during the FPC scan, and at this excitation frequency the fluorescence background due to other molecules is negligible.

Another reason for the high value of $g^{(2)}(0)$ is the spread in the interval between a click and the photon's true arrival time (transit time spread), a phenomenon that was described in Sec. 3.2. By using a ps laser, we have measured up to a total of 2.5 ns uncertainty in the photon detection response of each APD as a combination of an intrinsic transit time spread and an intensity dependent time shift of the output pulse.

To fit the measured $g^{(2)}(\tau)$ data we started with the theoretical expression from Eq. (1.15) and accounted for the background fluorescence determined from traces as shown in Fig. 6.9 according to [30]. The result was convolved with a two-detector response function derived from Gaussian-Lorentzian single detector response functions as shown in [102] and sketched in Fig. 6.10 a). A convolution with a pure Lorentzian or Gaussian function cannot fit all measured $g^{(2)}$-functions with a constant parameter set. This is demonstrated in Figs. 6.10 c) and d). The red curve is a fit with 3.3 ns FWHM Gaussian-Lorentzian response function as given in [102], the blue curve is a fit with a Lorentzian response function with 2.1 ns FWHM, and the green curve with a Gaussian and 4.1 ns FWHM. One can see that while the FWHM of the detector response functions are chosen to yield a satisfactory fit for high excitation powers, only the mixed Lorentzian-Gaussian fits the low excitation data with the same level of accuracy, with the same FWHM. We believe that a detector response function as shown in [102] and explained in Sec. 3.2 is a valid explanation for the increasing values of $g^{(2)}(0)$ for increasing excitation intensities.

6.2.4 Simulation of Mollow spectra

With the independently measured values of Ω_Γ, we calculated the theoretical spectra for the Mollow triplet for a two-level system at resonant excitation as given in Eq. (1.22). Since the single molecule under study was natural linewidth limited, we did not have to consider any dephasing. To obtain the theoretical spectra corresponding to our measurements, the independently measured laser background was added to the text-book spectrum and the result convolved with the FPC transmission spectrum shown in Fig. 6.7 a). The outcome is shown by the red curves in Fig. 6.7 b)-h), providing an excellent agreement between theory and experiment with only one scaling parameter for the absolute signal intensity.

6.3 Discussion and outlook

In this chapter the experimental observation of the resonance fluorescence of a single DBATT molecule in a solid host is presented. These measurements prove once more that single dye molecules at low temperatures can provide well behaved model systems to study quantum optics in the solid state. The samples show only minimal dephasing and high stability at strong driving fields. The measurement of the resonance fluorescence emission spectrum and the intensity correlation function on the Stokes shifted fluorescence shows manifestations of Rabi oscillations in two properties of the emitted light, spectrum and emission time, recorded simultaneously.

The solid immersion technique is a way to achieve a strong interaction between light and a single molecule. In the experiments shown here this situation was exploited to gain direct access to the resonant emission of the system, and polarization filtering is sufficient to separate the resonance fluorescence from spuriously scattered excitation light. Polarization optics can also be used to controllably influence amplitude and phase of the excitation and scattered fields, which provides a way to split the total detector signal into coherent and incoherent parts.

7 Nearfield extinction measurements

7.1 Nearfield excitation

Despite its limited applicability for strong focusing, Eq. (2.13) is often used to estimate the attenuation of a light beam of area A caused by an emitter with an extinction cross section σ_{ext}. The diffraction limit dictates a lower bound for A to be roughly $\lambda^2/4$, about twice smaller than the extinction cross section of an ideal two-level system. It would be desirable to confine the excitation light to an even smaller area than this limit, especially when working with non-ideal solid state systems. An arbitrary confinement can be achieved by restricting the light with an aperture.

As explained in Chap. 2, efficient interaction between a focused laser beam and a single quantum emitter requires a large mode overlap between the excitation and the scattered field at the detector. The optimal case, a dipolar excitation beam [83], can be constructed in far field optics with the aid of radial polarization states and ultra-high N.A. optics [91] for on-axis dipoles. An alternative are subwavelength apertures. It was shown that the far-field radiation pattern of a subwavelength conical aperture tip essentially resembles a combination of perpendicular magnetic and electric dipoles in the aperture plane [156, 157]. Furthermore, in analogy to a focused beam, the radiation from an aperture experiences a $\pi/2$ Gouy phase shift.

We pursued the above ideas by using a cryogenic scanning nearfield optical microscope (SNOM) [158, 159] to excite single DBATT molecules in a solid p-terphenyl matrix and study extinction in this geometry. These experiments were done chronologically before the far field SIL experiments, and have been analyzed in detail in [59, 71, 93]. The working principle of SNOM, the fiber production and sample preparation can be found in [71] and e.g. [160, 161, 162]. I will recapitulate the main results in this chapter, using the notation from Chap. 1 and 2. Similar studies of extinction from quantum dots and gold nanoparticles under fixed and scanning apertures are reported in [14, 163].

7.2 Experimental setup

Fig. 7.1 shows the schematics of the experiment. The excitation light is confined to the extend of an aperture at the end of a movable glass fiber tip. Molecules in a thin sample can be positioned in the nearfield under the tip and the excitation light as well as the molecular fluorescence is collected via a microscope objective.

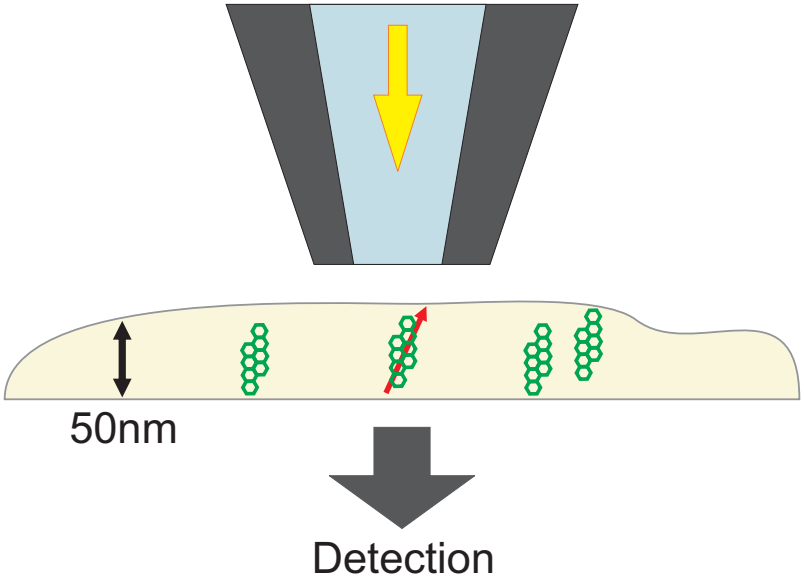

Figure 7.1: Schematics of the nearfield experiment. The red arrow denotes the orientation of the dipole transition moment of DBATT molecules in *p*-terphenyl.

Tip preparation and characterization

For a practical experimental realization of a movable aperture, a glass fiber is heated and pulled until it breaks, which results in a needle like tip. We evaporated 100-300 nm of Aluminum on the tip to ensure an opaque coating, which subsequently was removed in a controlled way using focused ion beam (FIB) milling [162]. Figure 7.2 b) shows the result of such a treatment, a round glass aperture of roughly 100nm diameter bounded in this case by a 300 nm Aluminum layer.

The light emerging from each tip was collimated by a microscope objective and imaged on a CCD camera for characterization, before a tip was used in the cryostat. We made sure to only use tips that showed a symmetric emission pattern and minimal leakage of light through the coating at the taper. In the optimal case, FIB milled apertures should exhibit only small change in transmission for different input polarizations [162], but most of the tips characterized by us showed a strongly prefered polarization axis, or emitted partly depolarized light. The ratio of power which is coupled into the SNOM-fiber to the power that is emitted by the aperture was between 10^5 to 10^6, depending on the aperture diameter.

Sample praparation and characterization

A thin sample increases the chance of finding a suitable molecule close to the surface and in the nearfield of the aperture. A method of producing thin crystalline films of *p*-terphenyl[1] on glass substrates via spincasting was developed in our group

[1]Which is a solid at room temperature.

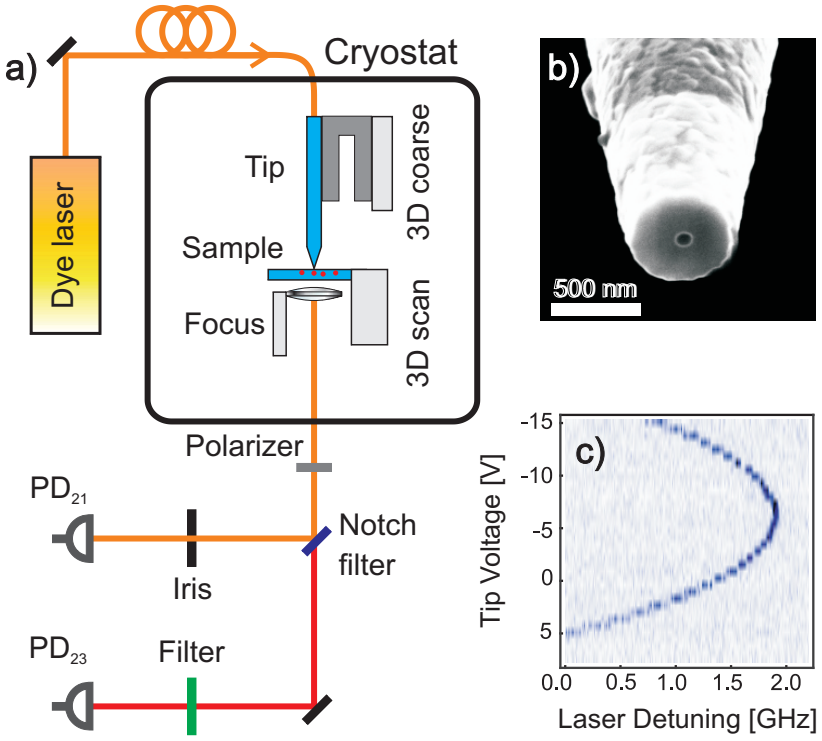

Figure 7.2: a) experimental setup for nearfield extinction measurements. b) scanning electron micrograph of a FIB treated aperture tip. c) Stark shift of a molecule against applied tip voltage. For details see the text.

[164]. The films have a thickness of 20-30 nm and dopant dye molecules exhibit extraordinary photostability at room temperature [164]. Annealing the samples for one hour at 60° C increased their thickness to 50-100 nm, but also enhanced the stability of dye molecules against spectral diffusion at cryogenic temperatures.

Unpolar dye molecules such as DBATT tend to "stand up" on the polar coverslip substrate, and studies have shown that most molecules are built in the matrix at the same orientation, similar to the case explained in [164]. We confirmed with back-focal plane imaging of single molecule emission patterns [136] at room temperature that the transition dipole moment of DBATT is oriented at 25 ± 5° to the optical axis, illustrated with a red arrow in Fig. 7.1. This is in contrast to the essentially randomly oriented dipole moments in a Shpol'skii system like *n*-tetradecane. Such a small angle from the optical axis is not optimal for achieving matching emission modes with the excitation light, which has to be taken into account for a comparison of results. At room temperature we determined the radiative lifetime to be 20 ± 3 ns and correspondingly the longitudinal decay rate $\Gamma_1 = 8 \pm 1$ MHz.

Optical and mechanical setup

The aperture tip was glued onto one arm of a quartz tuning fork, which was driven at its resonance frequency of roughly 33 kHz to mechanically oscillate at a very low amplitude of a few Å and used for shear force distance control [165, 166]. This technique uses the damping force experienced by a mechanical oscillator if it comes close to contact with a surface potential. The damping results in a change of amplitude and phase of the oscillation and can be used as a feedback signal for distance control. The tip and tuning fork were attached to a three axes piezo slider system [127] to coarse-position the tip close to the focus of a N.A.=0.8 microscope objective (`Olympus ACH60X`, 3mm working distance). The sample was positioned between tip and objective on a XYZ piezo scanner unit that could move up to 7 μm at T=1.4 K.

The setup is schematically shown in Fig. 7.2 a). The light from the tunable dye laser was coupled into the aperture fiber which was fed into the cryostat at the transfer system tube. To monitor and stabilize the excitation power, light emerging from a fiber bend just outside the cryostat was measured with a photodiode and the signal fed into a PID controller. We were able to stabilize the light intensity from the tip to about 0.3 % using this method. After traversing the sample and collimation objective, the excitation light and the fluorescence from a molecule under study were directed via an optical notch filter onto two APDs, PD_{21} and PD_{23}, which recorded the intensity at the excitation wavelength and the red shifted fluorescence from the molecule, respectively.

7.3 Nearfield extinction measurements

Tip influences

After a molecule was found by fluorescence excitation through the tip, the fluorescence signal on PD_{23} was maximized by scanning the sample in X and Y. Residual charges on the oxidized tip or in the sample always lead to a strong position-dependent Stark shift of the molecular resonance when it approached the tip. We could annul this shift by applying an appropriate voltage between the metallized tip and the cryostat background. Figure 7.2 c) shows the shift of the molecule's resonance as a function of the applied tip voltage for a fixed molecule position. At the apex of the voltage-shift parabola the position-dependent influence of the tip is minimized.

The proximity of a metallized object close to the molecule can result in nonradiative energy transfer, i.e. quenching of the emission, as well as shortening of the radiative lifetime [167, 168, 169, 170]. However, these effects are expected to be significant only at a distance of 30 nm and less [71]. In our experiment the limiting factor was the shearforce control which resulted in mechanical perturbations of the matrix and spectral instabilities of the molecule at distances below 50-100 nm. Figure 7.3 displays the shearforce error signal a) next to fluorescence excitation spectra of a single molecule b) as a function of tip-sample distance. In this example the shearforce signal already sets in below 150 nm, and simultaneously the molecule

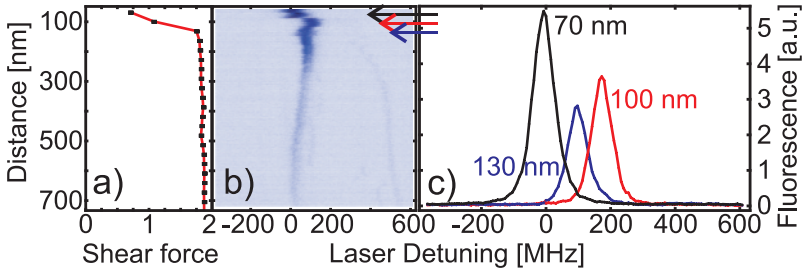

Figure 7.3: Shear-force distance control and the tip influence on the spectral stability of molecules. a) is the shear-force signal as the tip approaches the sample, b) shows fluorescence excitation spectra at the corresponding distances. The onset of a shear-force signal marks the position at which the molecular resonance becomes unstable. c) are three example scans from b) at the labeled distances.

exhibits spectral jumps and broadening. This is illustrated by three example scans at different distances in c). We chose to work at distances of 60-100 nm to avoid strong perturbations of the matrix.

Extinction

Fig. 7.4 a) shows a nearfield fluorescence excitation spectrum recorded on PD_{23}. The distance between the tip and the sample was 60 nm, and the FWHM of the line is 35 MHz, a factor of 4.4 larger than lifetime limited. In general, molecules in thin *p*-terphenyl films showed a larger amount of dephasing, compared to *n*-tetradecane. Figure 7.4 b) is the simultaneously recorded transmission spectrum on PD_{21}. A dip of 6 % was the largest effect seen for near-field excitation. The integration time was 200 ms per pixel, and the noise amounts to 0.3 %. The theoretical treatment in [59] is essentially equivalent to Eqs. (2.8), with the exception that in [59] the Franck-Condon factor α_{FC} was not considered in the reduced Rabi frequency. It is important to note that all near-field extinction measurements were conducted in the low excitation limit, $S \ll 1$, the main reason for this being the low aperture throughput.

In order to record this spectrum, two more optical elements were placed in the detection path, a linear polarizer and an iris that selected the central 1 mm of the beam. The iris was put in place to cut out uncollimated stray light and residual leakage from the out-of focus fiber taper. Its presence essentially limits the detection N.A. and might therefore increase the visibility of the extinction signal, but it also decreases the achievable SNR. A linear polarizer is oriented along the direction of the prefered molecular emission. As Fig. 7.5 demonstrates, the tip emission is highly linear polarized, however, with a 20° offset with respect to the main orientation of the molecular emission. Since both polarizations were fixed in this setup, the polarizer was used to cut out polarization components that do not interfere and result in an increased background.

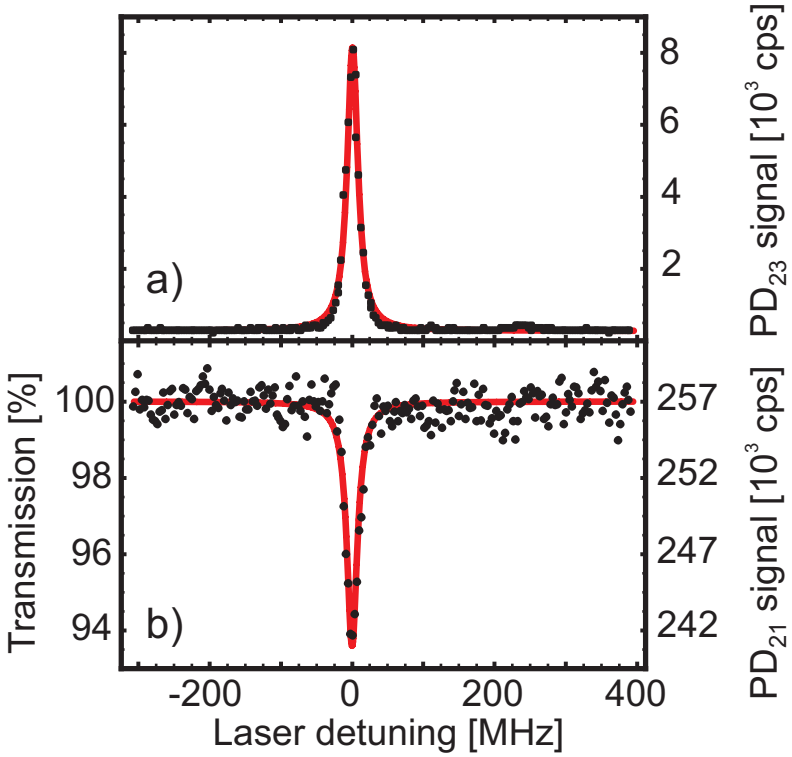

Figure 7.4: Simultaneously recorded fluorescence excitation and transmission spectrum of a single DBATT molecule under near-field excitation. The aperture size was 100 nm in this experiment.

7.4 Scanning coherent spectroscopy

The setup allowed for scanning the position of the molecule with respect to the tip. Not only the electric field at the molecule, but also the modal factors f and possibly g from Eq. (2.8) and with it the extinction spectrum are expected to change in such an experiment. An example is shown in Fig. 7.6, which shows fluorescence excitation (left) and extinction spectra (right) for three different distances z between tip and sample surface.

Fig. 7.7 shows another such experiment for a different DBATT molecule, and the results of a 3D finite difference time domain (FDTD) simulation of the geometry. For each tip-sample distance z, the fluorescence excitation spectrum and the extinction spectrum were fitted with Eqs. (2.8) and (2.10) and coefficients C_{intf}, ϕ and C_{23} as free parameters. Shown in Fig. 7.7 a) is the incident light intensity P_{inc} as the off-resonant detected power on PD_{21}, b) is the fluorescence signal P_{23}, c) and d) are visibility and phase of the extinction spectrum as defined in Eq. (4.4). The right side shows the results of a fit to the FDTD simulated spectra. These simulations were obtained by solving Maxwell's equations for a geometry close to the experimental situation, and integrating the field intensities over a reference sphere of 1.2 μm radius, bounded by the N.A. of the microscope objective. Details of the simulation

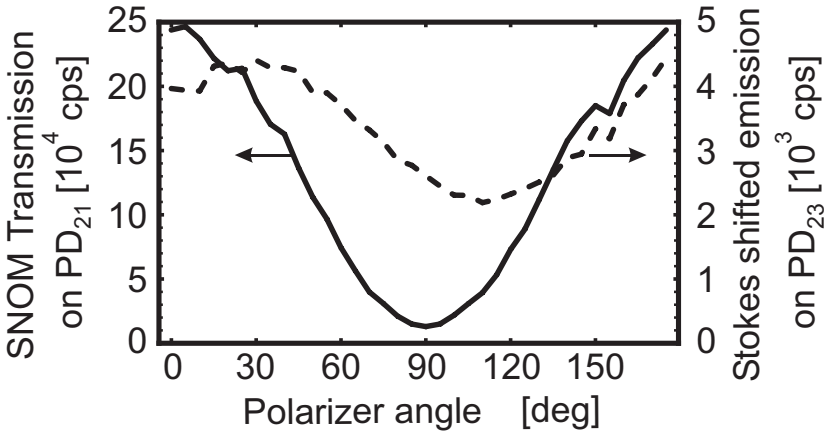

Figure 7.5: Polarization characteristics of excitation light from the tip (left axis) and the fluorescence from the molecule from Fig. 7.4 (right axis). The tip emission is linearly polarized, the molecular emission contains a large radially polarized component due to the orientation of the dipole transition moment.

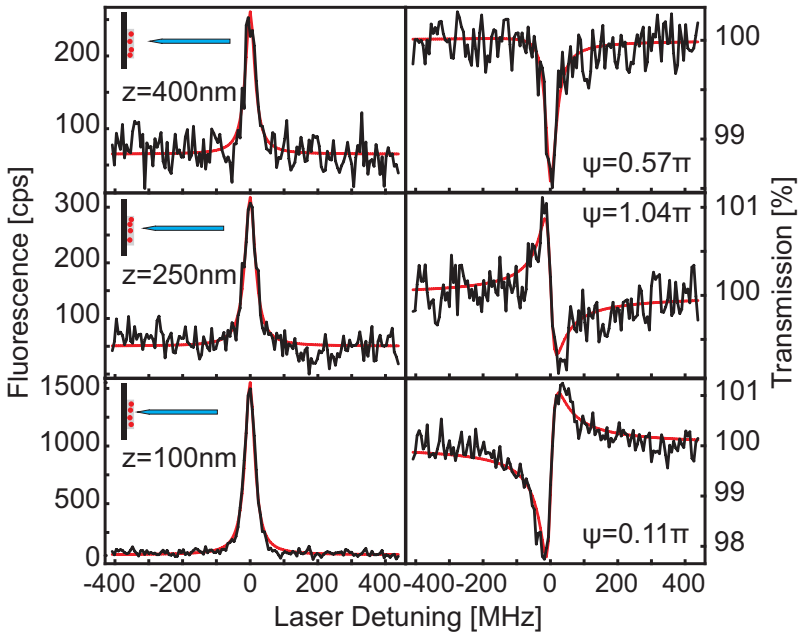

Figure 7.6: Examples of fluorescence excitation and extinction spectra for a molecule at three different tip-sample distances.

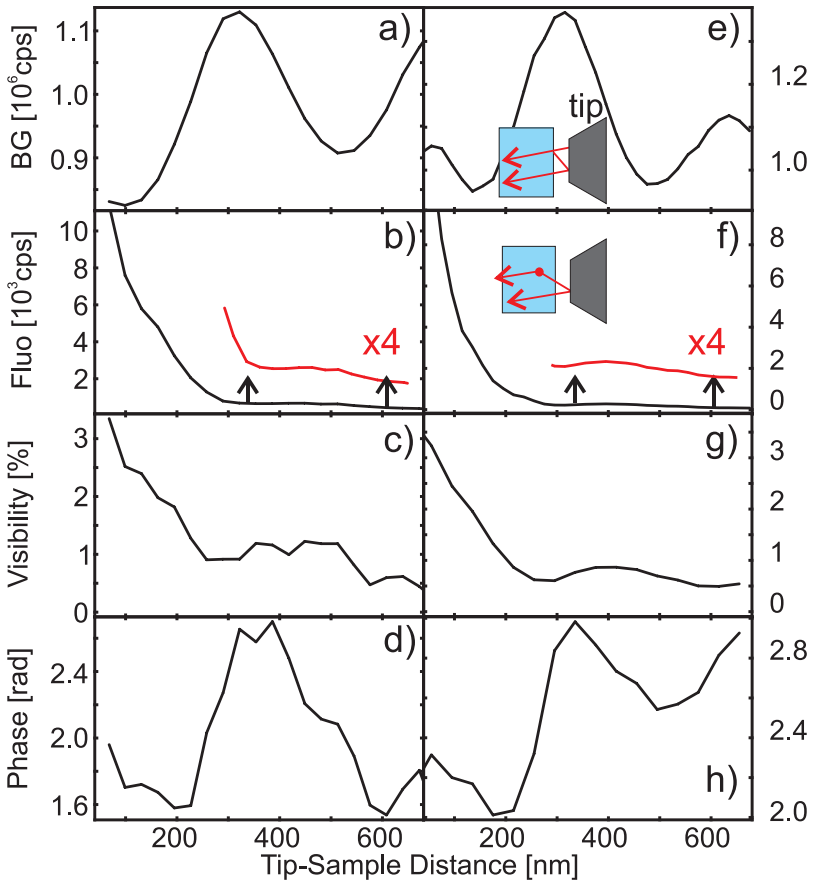

Figure 7.7: a)-d) experimental data and e)-h) results of FDTD simulations for incident and fluorescence powers, visibility and phase of extinction spectra as a function of tip-sample separation. The tip had a diameter of 200 nm in this experiment.

are given in [71]. The qualitative agreement between experiment and simulation is very good. In addition, the simulations give further insight into the origin of the obvious features in the distance dependent data.

The oscillations in P_{inc} from a) and e) are a result of interference of the laser light that directly propagates to the detector, and the light that is reflected between the sample surface and the tip apex. The position of minima and maxima agree with a Fabry-Perot cavity model. The modulation of the light emitted out of a SNOM tip as a function of its distance to the sample has been reported before in [161]. The fluorescence intensity shows a steep increase as the molecule is brought into the near-field of the tip. Small oscillations of P_{23}, visible in the tail of the curves (see zoom), are a result of a reflexion of the molecular *fluorescence* from the tip apex with π phase shift, and interference with the fluorescence that is directly propagated. The same Fabry-Perot argument as for P_{inc} predicts a minimum at around 300 nm which is approximately recovered in the data. However, the features are not as pronounced due to the emission pattern of the molecule close to the

sample surface, which favours the sample side. Also, the spectral breadth of the red shifted fluorescence, which covers about 50 nm as shown in Fig. 3.13, smears out the oscillations.

The shape of the extinction spectra is not straightforwardly explained. The modal factors $|f|$ and $|g|$ given in Eq. (2.8) *both* change as the tip-sample distance is lowered, as evident in Fig. 7.7 a) and b). The visibility as a function of distance is therefore a combination of the amplitude of both involved fields at the detector. The phase of the spectra at different tip-sample distances might be attributed to the Gouy phase evolution with distance from the aperture. However, this phase evolves the faster the more constricted a laser beam is [82]. A rough estimate can be the Rayleigh range of a Gaussian focus with waist w, which is $\frac{\pi w^2}{\lambda}$. An aperture of 200 nm diameter, as used for the presented experiment, would correspond to a Rayleigh length of about 50 nm, a distance that we did not probe with the molecule. Most of the phase evolution with distance turned out to be a result of reflections of excitation light and the molecular emission between tip apex and sample surface, and was reproduced qualitatively in the FDTD simulations shown in Fig. 7.7 h).

It should be noted that despite multiple reflections of the involved fields, a detector integrating over 4π has to see a linear proportionality between P_{23} and P_{ext}, as well as a purely absorptive shape of the extinction signal. This is not recovered in the limited detection solid angle of the presented experiment.

7.5 Discussion and outlook

Near-field extinction measurements of single molecules are technically limited in a number of ways. One shortcoming is that due to waveguiding cutoff, the tip transmission is only 10^{-6} to 10^{-5} which makes the interaction of a given light beam with the molecule highly inefficient. Coupling light in excess of a few μW into the near-field fiber can damage the thin Aluminum coating and destroy the tip. For these two reasons, experiments in the strong excitation regime are not feasible in this setup. Also, the fixed preferential polarization direction of our aperture tips made experiments like discussed in Sec. 6.1 impracticable.

On the other hand, excitation through subwavelength apertures has the potential to provide a close to perfect modal overlap and hence efficient excitation of a single emitter. We have demonstrated extinction spectra of single DBATT molecules with visibilities of up to 6 % shown in Fig. 7.4. A tentative extrapolation of the results to an ideal two-level system without dephasing but for an identical detection geometry would lead to a $1/\alpha \cdot 2\Gamma_2/\Gamma_1 \approx 20$ times larger extinction signal[2]. This is not in disagreement with energy conservation, as the resonance fluorescence term P_{21}, according to Eq. (2.11), would simultaneously increase by $(1/\alpha)^2 \cdot \frac{2\Gamma_2}{\Gamma_1} \approx 100$ times. Clearly this would not be in the low interaction limit anymore. In addition, the dipole moment is fixed at an unfavorable orientation in this sample. A different molecule/matrix system could increase the interaction efficiency further.

An added advantage, the possibility to apply strong local electrostatic fields and shift molecular resonances with respect to each other, makes studies of the coherent interaction of light with several resonant emitters a possibility.

[2]I approximated α as used in this thesis with the value we measured for DBATT in n-tetradecane

8 Conclusion & Outlook

8.1 Conclusion

This thesis describes experiments in which a freely propagating laser beam efficiently interacts with a single solid-state quantum system in a single pass geometry. The high excitation and detection efficiencies of this setup facilitated the direct observation of resonant interactions between a single dye molecule and a laser beam, and to study the molecule's resonance fluorescence over nine orders of magnitude.

In Chaps. 4 and 7 we studied extinction as an interference between the excitation and elastically scattered modes, and described methods to deliberately control this interference. Chap. 5 applied extinction spectroscopy to ultrasensitive detection of single molecules. The predictable but perhaps experimentally surprising result is that extinction measurements can surpass conventional fluorescence methods in terms of signal-to-noise ratio for the detection of weak emitters or at low excitation powers. In Chap. 6 we studied a basic topic in quantum optics, resonance fluorescence, and the dependence of its coherent and incoherent components on the excitation intensity. These experiments lead to one of the first direct studies of the resonance fluorescence of a solid-state emitter [72], as well as the observation of the Mollow fluorescence triplet.

8.2 Outlook

The experimental achievements shown here, and independent progress in quantum dot spectroscopy [17, 18], promote single emitter extinction measurements from a technologically complex and barely accessible challenge [1, 2, 14] to a practical tool for the study of coherent light-emitter interaction. The degree of efficiency that can be achieved in a solid-state single-pass setup might make these systems a real alternative to using high-finesse cavities [11, 171, 172].

Several interesting experiments are directly accessible with this setup. The interference of a classical coherent laser beam and the (first-order) coherent emission from a single quantum system manifests itself also in the intensity-intensity and also field-intensity correlation function [173]. Depending on the phase between the classical and quantum field, bunching or antibunching are expected [135]. Along this line, the coherent interaction between light and several identical emitters, which can be realized in single molecule samples via local Stark shifts [174], should result in changes in the extinction signal [175], but also the above correlation functions [176].

Additional pumping of the molecule into its excited state, e.g. via -possibly pulsed- 0-1 excitation explained in Chap. 1 could have a similar application. It leads to a reverse phase ϕ_f of the molecular emission and hence a change from destructive to constructive interference in the forward direction, similar to stimulated emission. The combination of 0-1 excitation and resonant probing therefore opens the possibility to influence the intensity, phase and photon statistics of the transmitted radiation dependent on the presence of the pump photons. Conditional (phase) gates are important building blocks for quantum information technologies [11, 177, 178].

Single emitter detection and spectroscopy with less than a picoWatt excitation power as demonstrated here is an interesting option for weak emitters. One example are rare earth ions in various laser crystals. Transitions within the inner lying 4f shell are protected from matrix influences, and such transitions typically have lifetimes in the tens of μs range [179]. This makes such ions promising candidates for quantum information systems, but also makes their optical detection and manipulation challenging. In these ions, transitions into long lived intermediate shelving states result in a large fraction of time in which the ion is in an off state. If numbers for Praseodymium Pr^{3+} [180] are inserted into the optical Bloch equations (1.23), one can estimate a stationary state excited state population of merely 3 %. This estimate includes additional depopulation of the long lived shelving states back into the excited state via optical pumping. On the other hand, the branching ratio α is very high in these systems. The high sensitivity of extinction measurements at low illumination light powers can help to detect such systems. Transitions into the shelving states[1] on the other hand occur at a rate of below 10 Hz, which is out of reach for direct detection.

A second example is single molecule excitation or even spectroscopy using ultra faint light sources such as a second single molecule. Several theoretical studies treat this scenario and implications for correlation measurements of emitted photons for ideal TLSs [181, 182]. As a first step, a single molecule excited via 0-1 transitions [22, 58] is a source of (spontaneously emitted) single photons. The emission into the narrow-band 0-0 ZPL can be as strong as $\alpha_{DW}\alpha_{FC}\Gamma_1\rho_{22}|_{S=1} \approx 10^7$ photons per second [22]. After collection and handling optics, a number in the range of $10^3 - 10^5$ photons per second will be available to excite a second molecule. Extinction detection can provide a way to verify a successful interaction at such a low count rate.

Such a photon transfer between two emitters has numerous applications in quantum networking [12]. An incoherent resonant energy transfer has been observed in waveguide or cavity systems [183, 184] over microscopic distances, but the demonstration of a coherent free-space implementation should be well within reach given the advances demonstrated in this work.

[1] The equivalent to Stokes shifted emission of a single molecule.

Bibliography

[1] D.J. Wineland, W.M. Itano, and J.C. Bergquist. Absorption spectroscopy at the limit: detection of a single atom. *Optics Letters*, 12:389–391, 1987.

[2] W.E. Moerner and L. Kador. Optical detection and spectroscopy of single molecules in a solid. *Physical Review Letters*, 62:2535–2538, 1989.

[3] M. Orrit and J. Bernard. Single pentacene molecules deteced by fluorescence excitation in a *p*-terphenyl crystal. *Physical Review Letters*, 65:2716–2719, 1990.

[4] L. Kador, T. Latychevskaia, A. Renn, and U.P. Wild. Absorption spectroscopy on single molecules in solids. *Journal of Chemical Physics*, 111:8755–8758, 1999.

[5] E. Betzig and R.J. Chichester. Single molecules observed by near-field scanning optical microscopy. *Science*, 262:1422–1425, 1993.

[6] T. Funatsu, Y. Harada, M. Tokunaga, K. Saito, and T. Yanagida. Imaging of single fluorescent molecules and individual atp turnovers by single myosin molecules in aqueous-solution. *Nature*, 374:555–559, 1995.

[7] S. Weiss. Fluorescence spectroscopy of single biomolecules. *Science*, 283:1676–1683, 1999.

[8] E. Betzig, G.H. Patterson, R. Sougrat, O.W. Lindwasser, S. Olenych, J.S. Bonifacio, M.W. Davidson, J. Lippincott-Schwartz, and H.F. Hess. Imaging intracellular fluorescent proteins at nanometer resolution. *Science*, 313:1642–1645, 2006.

[9] P. Tamarat, B. Lounis, J. Bernard, M. Orrit, S. Kummer, R. Kettner, S. Mais, and T. Basch. Pump-probe experiments with a single molecule: ac-stark effect and nonlinear optical response. *Physical Review Letters*, 75:1514 – 1517, 1995.

[10] C. Brunel, B. Lounis, P. Tamarat, and M. Orrit. Rabi resonances of a single molecule driven by rf and laser fields. *Physical Review Letters*, 81:2679–2682, 1998.

[11] Q.A. Turchette, C.J. Hood, W. Lange, H. Mabuchi, and H.J. Kimble. Measurement of conditional phase shifts for quantum logic. *Physical Review Letters*, 75:4710 – 4713, 1995.

[12] J.I. Cirac, P. Zoller, H.J. Kimble, and H. Mabuchi. Quantum state transfer and entanglement distribution among distant nodes in a quantum network. *Physical Review Letters*, 78, 1997.

[13] T. Wilk, S. Webster, A. Kuhn, and G. Rempe. Single-atom single-photon quantum interface. *Science*, 317:488–490, 2007.

[14] J.R. Guest, T.H. Stievater, X. Li, J. Cheng, D.G. Steel, D. Gammon, D.S. Katzer, D. Park, C. Ell, A. Thränhardt, G. Khitrova, and H.M. Gibbs. Measurement of optical absorption by a single quantum dot exciton. *Physical Review B*, 65:241310, 2002.

[15] M. Kroner, S. Rémi, A. Högele, S. Seidl, A.W. Holleitner, R.J. Warburton, B.D. Gerardot, P.M. Petroff, and K. Karrai. Resonant saturation laser spectroscopy of a self-assembled quantum dot. *Physica E*, in press, 2007.

[16] M. Atatüre, J. Dreiser, A. Badolato, and A. Imamoglu. Observation of faraday rotation from a single confined spin. *Nature Physics*, 3:101–105, 2007.

[17] B.D. Gerardot, S. Seidl, P.A. Dalgarno, R.J. Warburton, M. Kroner, K. Karrai, A. Badolato, and P.M. Petroff. Contrast in transmission spectroscopy of a single quantum dot. *Applied Physics Letters*, 90:221106, 2007.

[18] A.N. Vamivakas, M. Atatüre, J. Dreiser, S.T. Yilmaz, A. Badolato, A.K. Swan, B.B. Goldberg, A. Imamoglu, and M.S. Ünlü. Strong extinction of a far-field laser beam by a single quantum dot. *Nano Letters*, 7:2892 –2896, 2007.

[19] J. Friedrich and D. Haarer. Photochemical hole burning: A spectroscopic study of relaxation processes in polymers and glasses. *Angewandte Chemie International Edition in English*, 23:113–140, 1984.

[20] K.K. Rebane. *Impurity Spectra of Solids*. Plenum Press, 1970.

[21] W.E. Moerner and M. Orrit. Illuminating single molecules in condensed matter. *Science*, 283:1670–1676, 1999.

[22] R. Lettow, V. Ahtee, R. Pfab, A. Renn, E. Ikonen, S. Götzinger, and V. Sandoghdar. Realization of two fourier-limited solid-state single-photon sources. *Optics Express*, 15:15842–15847, 2007.

[23] W.P. Ambrose, T. Basché, and W.E. Moerner. Detection and spectroscopy of single pentacene molecules in a p-terphenyl crystal by means of fluorescence excitation. *Journal of Chemical Physics*, 95:7150–7163, 1991.

[24] T. Irngartinger, A. Renn, G. Zumofen, and U.P. Wild. Temperature dependence of single-molecule line widths: Terrylene in *n*-alkane matrices. *Journal of Luminescence*, 76–77:279–282, 1998.

[25] A.-M. Boiron, B. Lounis, and M. Orrit. Single molecules of dibenzanthanthrene in *n*-hexadecane. *Journal of Chemical Physics*, 105:3969–3974, 1996.

[26] K. Palewska, J. Lipinski, J. Sworakowski, J. Sepiol, H. Gygax, E.C. Meister, and U.P. Wild. Total luminescence spectroscopy of terrylene in low-temperature Shpol'skii matrixes. *Journal of Physical Chemistry*, 99:16835–16841, 1995.

[27] E.M.H.P. van Dijk, J. Hernando, J.-J. Garcia-Lopez, M. Crego-Calama, D.N. Reinhoudt, L. Kuipers, M.F. Garcia-Parajo, and N.F. van Hulst. Single-molecule pump-probe detection resolves ultrafast pathways in individual and coupled quantum systems. *Physical Review Letters*, 94:078302, 2005.

[28] W.E. Moerner. Examining nanoenvironments in solids on the scale of a single, isolated impurity molecule. *Science*, 265:46, 1994.

[29] C. Eggeling, J. Widengren, R. Rigler, and C.A.M. Seidel. Photobleaching of fluorescent dyes under conditions used for single-molecule detection: Evidence of two-step photolysis. *Analytical Chemistry*, 70:2651–2659, 1998.

[30] L. Fleury, J. M. Segura, G. Zumofen, B. Hecht, and U.P. Wild. Nonclassical photon statistics in single-molecule fluorescence at room temperature. *Physical Review Letters*, 84:1148–1151, 2000.

[31] T. Basché. Fluorescence intensity fluctuations of single atoms, molecules and nanoparticles. *Journal of Luminescence*, 76 & 77:263–269, 1998.

[32] T. Basché, S. Kummer, and C. Bräuchle. Direct spectroscopic observation of quantum jumps of a single molecule. *Nature*, 373:132–134, 1995.

[33] J. Bernard, L. Fleury, H. Talon, and M. Orrit. Photon bunching in the fluorescence from single molecules: A probe for intersystem crossing. *Journal of Chemical Physics*, 98:850–859, 1993.

[34] A. Bloeß, Y. Durand, M. Matsushita, R. Verberk, E.J.J. Groenen, and J. Schmidt. Microscopic structure in a shpol'skii system: A single-molecule study of dibenzanthanthrene in *n*-tetradecane. *Journal of Physical Chemistry A*, 105:3016–3021, 2001.

[35] J.L. Richards and S.A. Rice. Study of impurity-host coupling in Shpols'kii matrices. *Journal of Chemical Physics*, 54:2014–2023, 1971.

[36] M. Lamotte, A.M. Merle, J. Joussot-Dubien, and F. Dupuy. Multiplet structure of the emission bands of coronene and perylene in *n*-heptane single crystal. *Chemical Physics Letters*, 35:410–416, 1975.

[37] A. Bloeß, Y. Durand, M. Matsushita, J. Schmidt, and E.J.J. Groenen. A single-molecule study of the relation between resonance frequencey and the orientation of a guest molecule in a Shpol'skii system. *Chemical Physics Letters*, 344:55–60, 2001.

[38] A.-M. Boiron, F. Jelezko, Y. Durand, B. Lounis, and M. Orrit. Dibenzanthanthrene in *n*-hexadecane, dibenzoterrylene in naphthalene: Two new systems for single molecule spectroscopy. *Molecular Crystals and Liquid Crystals*, 291:41–44, 1996.

[39] C. Brunel, B. Lounis, P. Tamarat, and M. Orrit. Triggered source of single photons based on controlled single molecule fluorescence. *Physical Review Letters*, 83:2722–2725, 1999.

[40] R. Loudon. *The quantum theory of light*. Oxford Univerity Press, 3rd edition, 2000.

[41] F. Bloch. Nuclear induction. *Physical Review*, 70:460–474, 1946.

[42] C. Cohen-Tannoudji, J. Dupont-Roc, and G. Grynberg. *Atom-Photon Interactions: Basic Processes and Applications*. Wiley-Interscience, 1992.

[43] L. Allen and J.H. Eberly. *Optical Resonance and Two-Level Atoms*. Dover Publications, 1987.

[44] J.D. Jackson. *Classical Electrodynamics*. Wiley & Sons, 1998.

[45] D. Stoler. Photon antibunching and possible ways to observe it. *Physical Review Letters*, 33:1397–1400, 1974.

[46] H.J. Kimble and L. Mandel. Theory of resonance fluorescence. *Physical Review A*, 13:2123 – 2144, 1976.

[47] H.J. Carmichael and D.F. Walls. A quantum-mechanical master equation treatment of the dynamical stark effect. *Journal of Physics B*, 9:1199–1219, 1976.

[48] A. Müller, E.B. Flagg, P. Bianucci, D.G. Deppe, W. Ma, J. Zhang, G.J. Salamo, and C.K. Shih. Coherently driven non-classical light emission from a quantum dot. *ArXiv*, 0707.3808, 2007.

[49] B.R. Mollow. Power spectrum of light scattered by two-level systems. *Physical Review*, 188:1969 – 1975, 1969.

[50] J.D. Cresser, J. Hager, G. Leuchs, M. Rateike, and H. Walther. *Resonance Fluorescence of Atoms in Strong Monochromatic Laser Fields*, volume 27 of *Topics in Current Physics*, chapter 3, pages 21–59. Springer-Verlag, 1982. Dissipative Systems in Quantum Optics: Resonance Fluorescence, Optical Bistability, Superfluorescence.

[51] H. Walther. Resonance fluorescence of two-level atoms. *Advances in Atomic, Molecular, and Optical Physics*, 51:239–272, 2005.

[52] P.A. Apanasevich and S.Ja. Kilin. Photon bunching and antibunching in resonance fluorescence. *J.Phys.B*, 12:L83–L86, 1979.

[53] J. Dalibard and S. Reynaud. Correlation signals in resonance fluorescence: interpretation via photon scattering amplitudes. *J.Physique*, 44:1337–1343, 1983.

[54] G. Nienhuis. Spectral correlations in resonance fluorescence. *Phys.Rev.A*, 47:510–518, 1993.

[55] A. Aspect, G. Roger, S. Reynaud, J. Dalibard, and C. Cohen-Tannoudji. Time correlations between the two sidebands of the resonance fluorescence triplet. *Physical Review Letters*, 45:617–620, 1980.

[56] C.A. Schrama, G. Nienhuis, H.A. Dijkerman, C. Steijsiger, and H.G.M. Heideman. Intensity correlations between the components of the resonance fluorescence triplet. *Phys.Rev. A*, 45:8045–8055, 1992.

[57] B. Lounis, F. Jelezko, and M. Orrit. Single molecules driven by strong resonant fields: Hyper-raman and subharmonic resonances. *Physical Review Letters*, 78:3673–3676, 1997.

[58] A. Kiraz, M. Ehrl, C. Bräuchle, and A. Zumbusch. Low temperature single molecule spectroscopy using vibronic excitation and dispersed fluorescence detection. *Journal of Chemical Physics*, 118:10821–10824, 2003.

[59] I. Gerhardt, G. Wrigge, P. Bushev, G. Zumofen, R. Pfab, and V. Sandoghdar. Strong extinction of a laser beam by a single molecule. *Physical Review Letters*, 98:033601, 2007.

[60] F. Schuda, C.R. Stroud, and M. Hercher. Observation of the resonant stark effect at optical frequencies. *Journal of Physics B*, 7:L198–L202, 1974.

[61] F.Y. Wu, R.E. Grove, and S. Ezekiel. Investigation of the spectrum of resonance fluorescence induced by a monochromatic field. *Physical Review Letters*, 35:1426 – 1429, 1975.

[62] W. Hartig, W. Rasmussen, R. Schieder, and H. Walther. Study of the frequency distribution of the fluorescent light induced by monochromatic radiation. *Zeitschrift für Physik A*, 278:205–210, 1976.

[63] H.M. Gibbs and T.N.C. Venkatesan. Direct observation of fluorescence narrower than the natural linewidth. *Optics Communications*, 17:87–90, 1976.

[64] J.T. Höffges, H.W. Baldauf, W. Lange, and H. Walther. Heterodyne measurement of the resonance fluorescence of a single ion. *Journal of Modern Optics*, 44:1999–2010, 1997.

[65] R. Hanbury-Brown and R.Q. Twiss. A test of a new type of stellar interferometer on sirius. *Nature*, 178:1046–1048, 1956.

[66] H.J. Kimble, M. Dagenais, and L. Mandel. Photon antibunching in resonance fluorescence. *Physical Review Letters*, 39:691–695, 1977.

[67] T.H. Stievater, X. Li, D.G. Steel, D. Gammon, D.S. Katzer, D. Park, C. Piermarocchi, and L.J. Sham. Rabi oscillations of excitons in single quantum dots. *Physical Review Letters*, 87:133603, 2001.

[68] B. Alén, F. Bickel, K. Karrai, R.J. Warburton, and P.M. Petroff. Stark-shift modulation absorption spectroscopy of single quantum dots. *Applied Physics Letters*, 83:2235–2237, 2003.

[69] B. Alén, A. Högele, M. Kroner, S. Seidl, K. Karrai, R.J. Warburton, A. Badolato, G. Medeiros-Ribeiro, and P.M. Petroff. Absorptive and dispersive optical responses of excitons in a single quantum dot. *Applied Physics Letters*, 89:123124, 2006.

[70] T. Plakhotnik and V. Palm. Interferometric signatures of single molecules. *Physical Review Letters*, 87:183602, 2001.

[71] I. Gerhardt, G. Wrigge, M. Agio, P. Bushev, G. Zumofen, and V. Sandoghdar. Scanning near-field optical coherent spectroscopy of single molecules at 1.4 K. *Optics Letters*, 32:1420–1422, 2007.

[72] A. Müller, E.B. Flagg, P. Bianucci, X. Wang, D. Deppe, W. Ma, J. Zhang, G.J. Salamo, M. Xiao, and C.K. Shih. Resonance fluorescence from a coherently driven semiconductor quantum dot in a cavity. *Physical Review Letters*, 99:187402, 2007.

[73] A. Müller. *Resonance Fluorescence and Cavity Quantum Electrodynamics with Quantum Dots*. PhD thesis, University of Texas at Austin, 05 2007.

[74] X. Xu, B. Sun, P.R. Berman, D.G. Steel, A.S. Bracker, D. Gammon, and L.J. Sham. Coherent optical spectroscopy of a strongly driven quantum dot. *Science*, 317:929–932, 2007.

[75] T. Basché, W.E. Moerner, M. Orrit, and H. Talon. Photon antibunching in the fluorescence of a single dye molecule trapped in a solid. *Physical Review Letters*, 69:1516–1519, 1992.

[76] R. Brouri, A. Beveratos, J.-P. Poizat, and P. Grangier. Photon antibunching in the fluorescence of individual color centers in diamond. *Optics Letters*, 25:1294–1296, 2000.

[77] P. Michler, A. Imamoglu, M.D. Mason, P.J. Carson, G.F. Strouse, and S.K. Buratto. Quantum correlation among photons from a single quantum dot at room temperature. *Nature*, 406:968–970, 2000.

[78] H.C. van de Hulst. On the attenuation of plane waves by obstacles of arbitrary size and form. *Physica*, 15:740–746, 1949.

[79] C.F. Bohren and D.R. Huffmann. *Absorption and Scattering of Light by Small Particles*. Wiley-Interscience, 1998.

[80] C.F. Bohren. How can a particle absorb more than the light incident on it. *American Journal of Physics*, 51:323–327, 1983.

[81] H. Paul and R. Fischer. Light absorption by a dipole. *Soviet Physics Uspekhi*, 26:923–926, 1983.

[82] S. Feng and H.G. Winful. Physical origin of the gouy phase shift. *Optics Letters*, 26, 2001.

[83] G. Zumofen, N.M. Mojarad, V. Sandoghdar, and M. Agio. Perfect reflection of light by an oscillating dipole. *ArXiv*, 0805.3231v2, 2008.

[84] S.J. van Enk and H.J. Kimble. Strongly focused light beams interacting with single atoms in free space. *Physical Review A*, 63:023809, 2001.

[85] S.J. van Enk. Atoms, dipole waves, and strongly focused light beams. *Physical Review A*, 69:043813, 2004.

[86] N.M. Mojarad, V. Sandoghdar, and M. Agio. Plasmon spectra of nanospheres under a tightly focused beam. *to appear: Journal of the Optical Society of America B*, 2008.

[87] C.J.R. Sheppard and P. Török. Electromagnetic field in the focal region of an electric dipole wave. *Optik*, 104:175–177, 1997.

[88] R.G. Newton. *Scattering Theory of Waves and Particles*. Courier Dover Publications, 2002.

[89] K. Karrai and R.J. Warburton. Optical transmission and reflection spectroscopy of single quantum dots. *Superlattices and Microstructures*, 33:311–337, 2005.

[90] N. Lindlein, R. Maiwald, H. Konermann, M. Sondermann, U. Peschel, and G. Leuchs. A new 4 pi geometry optimized for focusing on an atom with a dipole-like radiation pattern. *Laser Physics*, 17:927–934, 2007.

[91] R. Dorn, S. Quabis, and G. Leuchs. Sharper focus for a radially polarized light beam. *Physical Review Letters*, 91:233901, 2003.

[92] G. Alber. Photon wave packets and spontaneous decay in a cavity. *Physical Review A*, 46, 1992.

[93] I. Gerhardt. *Scattering & Absorption of Light by a Single Molecule under a Subwavelength Aperture*. PhD thesis, ETH Zürich, 2006.

[94] B. Hillerich and E. Weidel. Polarization noise in single mode fibres and its reduction by depolarizers. *Optical and Quantum Electronics*, 15:281–287, 1983.

[95] M. Gehrtz, G.C. Bjorklund, and E.A. Whittaker. Quantum-limited laser frequency-modulation spectroscopy. *Journal of the Optical Society of America B*, 2:1510, 1985.

[96] P.G. Kwiat, A.M. Steinberg, R.Y. Chiao, P.H. Eberhard, and M.D. Petroff. High-efficiency single photon detectors. *Physical Review A*, 48:867–870, 1993.

[97] Li-Qiang Li and L.M. Davis. Single photon avalanche diode for single molecule detection. *Review of Scientific Instruments*, 64:1524–1529, 1993.

[98] A. Spinelli, L.M. Davis, and H. Dautet. Actively quenched single-photon avalanche diode for high repitition rate time-gated photon counting. *Review of Scientific Instruments*, 67:55–61, 1996.

[99] I. Rech, I. Labanca, M. Ghioni, and S. Cova. Modified single photon counting modules for optimal timing performance. *Review of Scientific Instruments*, 77, 2006.

[100] R.G.W. Brown, K.D. Ridley, and J.G. Rarity. Characterization of silicon avalanche photodiodes for photon correlation measurements. 1: Passive quenching. *Applied Optics*, 25:4122–4126, 1986.

[101] R.G.W. Brown, R. Jones, J.G. Rarity, and K.D. Ridley. Characterization of silicon avalanche photodiodes for photon correlation measurements. 2: Active quenching. *Applied Optics*, 26:2383–2389, 1987.

[102] S. Felekyan, R. Kühnemuth, V. Kudryavtsev, C. Sandhagen, W. Becker, and C.A.M. Seidel. Full correlation from picoseconds to seconds by time-resolved and time-correlated single photon detection. *Review of Scientific Instruments*, 76:083104, 2005.

[103] G. Ripamonti and S. Cova. Carrier diffusion effects in the time-response of a fast photodiode. *Solid-State Electronics*, 28:925–931, 1985.

[104] Perkin-Elmer. *SPCM-AQR Single Photon Counting Module*. Perkin Elmer.

[105] C. Kurtsiefer, P. Zarda, S. Mayer, and H. Weinfurter. The breakdown flash of silicon avalanche photodiodes–back door for eavesdropper attacks? *Journal of Modern Optics*, 48:2039 – 2047, 2001.

[106] C.G. Coates. A sensitive detector for ultralow-light imaging. *American Laboratory*, 36:13–19, 2004.

[107] LambdaResearchCorporation. *OSLO Optics Reference*. Lambda Research Corporation, 80 Taylor Street P.O. Box 1400 Littleton, MA 01480, 6.1 edition.

[108] W.B. King. Dependence of the strehl ratio on the magnitude of the variance of the wave aberration. *Journal of the Optical Society of America*, 58:655–661, 1968.

[109] S.M. Mansfield and G.S. Kino. Solid immersion microscope. *Applied Physics Letters*, 57:2615–2616, 1990.

[110] S.M. Mansfield. *Solid Immersion Microscopy*. PhD thesis, Stanford, 1992.

[111] J. Guerra. Photon tunneling microscopy. *Applied Optics*, 29:3741–3752, 1990.

[112] Q. Wu, G.D. Feke, R.D. Grober, and L.P. Ghislain. Realization of numerical aperture 2.0 using a gallium phosphide solid immersion lens. *Applied Physics Letters*, 75:4064, 1999.

[113] W.L. Barnes, G. Björk, J.M. Gerard, P. Jonsson, J.A.E. Wasey, P.T. Worthing, and V. Zwiller. Solid-state single photon sources: light collection strategies. *European Physical Journal D*, 18:197–210, 2002.

[114] K. Karrai, X. Lorenz, and L. Novotny. Enhanced reflectivity contrast in confocal solid immersion lens microscopy. *Applied Physics Letters*, 77:3459, 2000.

[115] B.D. Terris, H.J. Mamin, D. Rugar, W.R. Studenmund, and G.S. Kino. Near-field optical data storage using a solid immersion lens. *Applied Physics Letters*, 65:388–390, 1994.

[116] M. Yoshita, K. Koyama, Y. Hayamizu, M. Baba, and H. Akiyama. Improved high collection efficiency in fluorescence microscopy with a weierstrass-sphere solid immersion lens. *Japanese Journal of Applied Physics*, 41:L858–L860, 2002.

[117] A.T. Collins. The use of the weierstrass sphere geometry in luminescence spectroscopy. *Journal of Physics D*, 10, 1977.

[118] M. Baba, T. Sasaki, M. Yoshita, and H. Akiyama. Aberrations and allowances for errors in a hemisphere solid immersion lens for submicron-resolution photoluminescence microscopy. *Journal of Applied Physics*, 85:6923–6925, 1999.

[119] M. Yoshita, T. Sasaki, M. Baba, and H. Akiyama. Application of solid immersion lens to high-spatial resolution photoluminescence imaging of gaas quantum wells at low temperatures. *Applied Physics Letters*, 73:635, 1998.

[120] S. M. Mansfield, W.R. Studenmund, G.S. Kino, and K. Osato. High-numerical-aperture lens system for optical storage. *Optics Letters*, 18:305, 1993.

[121] I. Ichimura, S. Hayashi, and G.S. Kino. High-density optical recording using a solid immersion lens. *Applied Optics*, 36:4339, 1997.

[122] L. Novotny, R.D. Grober, and K. Karrai. Reflected image of a strongly focused spot. *Optics Letters*, 26:789–791, 2001.

[123] D.R. Lide, editor. *CRC handbook of chemistry and physics*. Taylor & Francis, 87th edition, 2006.

[124] L. Fleury, A. Gruber, A. Dräbenstedt, J. Wrachtrup, and C. von Borczyskowski. Low-temperature confocal microscopy on individual molecules near a surface. *Journal of Physical Chemistry B*, 101:7933–7638, 1997.

[125] Y. Durand, A. Bloeß, J. Köhler, E.J.J. Groenen, and J. Schmidt. Spectral diffusion of individual pentacene, terrylene, and dibenzanthanthrene molecules in *n*-tetradecane. *Journal of Chemical Physics*, 114:6843–6850, 2001.

[126] B. Eiermann. Spektroskopische Untersuchnung von einzelnen Terrylen Molekülen in Mikrokristallen. Master's thesis, Universität Konstanz, 05 1999.

[127] J. Michaelis. *Mikroskopie mit einem einzelnen Molekül als Lichtquelle*. PhD thesis, University of Konstanz, 6 2000.

[128] C. Schmitt. Modifikation der spektralen Eigenschaften eines einzelnen Moleküls vor einer Oberfläche. Master's thesis, Uni Konstanz, 1 2001.

[129] C. Hettich. *Coherent Optical Dipole Coupling of Two Individual Molecules at Nanometre Separation*. PhD thesis, University of Konstanz, 10 2002.

[130] Y.Durand, A. Bloeß, J. Köhler, E.J.J. Groenen, and J. Schmidt. Spectral diffusion of individual pentacene, terrylene, and dibenzanthanthrene molecules in *n*-tetradecane. *Journal of Chemical Physics*, 114:6843–6850, 2001.

[131] T. Plakhotnik, W.E. Moerner, V. Palm, and U.P. Wild. Single molecule spectroscopy: maximum emission rate and saturation intensity. *Optics Communications*, 114:83–88, 1995.

[132] K. Koyama, M. Yoshita, M. Baba, T. Suemoto, and H. Akiyama. High collection efficiency in fluorescence microscopy with a solid immersion lens. *Applied Physics Letters*, 75:1667–1669, 1999.

[133] G. Gouesbet, B. Maheu, and G. Grehan. Light scattering from a sphere arbitrarily located in a gaussian beam, using a bromwich formulation. *Journal of the Optical Society of America A*, 5:1427–1443, 1988.

[134] V. Jacobsen, P. Stoller, C. Brunner, V. Vogel, and V. Sandoghdar. Interferometric optical detection and tracking of very small gold nanoparticles at a water-glass interface. *Optics Express*, 14:405–414, 2005.

[135] S.J. van Enk and H.J. Kimble. Single atom in free space as a quantum aperture. *Physical Review A*, 61:051802, 2000.

[136] M.A. Lieb, J.M. Zavislan, and L. Novotny. Single-molecule orientations determined by direct emission pattern imaging. *Journal of the Optical Society of America B*, 21:1210–1215, 2004.

[137] A. Alu and N. Engheta. Enhanced directivity from subwavelength infrared/optical nano-antennas loaded with plasmonic materials or metamaterials. *IEEE Trans. Antennas and Propagation*, 55:3027–, 2007.

[138] J. Hwang, M.M. Fejer, and W.E. Moerner. Scanning interferometric microscopy for the detection of ultrasmall phase shifts in condensed matter. *Physical Review A*, 73:021802, 2006.

[139] C. Sönnichsen, S. Geier, N.E. Hecker, G. von Plessen, J. Feldmann, H. Ditlbacker, B. Lamprecht, J.R. Krenn, F.R. Aussenegg, V.Z-H. Chan, J.P. Spatz, and M. Möller. Spectroscopy of single metallic nanoparticles using total internal reflection microscopy. *Applied Physics Letters*, 77:2949–2951, 2000.

[140] A. Arbouet, D. Christofilos, N. Del Fatti, F. Valle, J. R. Huntzinger, L. Arnaud, P. Billaud, and M. Broyer. Direct measurement of the single-metal-cluster optical absorption. *Physical Review Letters*, 93:127401, 2004.

[141] K. Lindfors, T. Kalkbrenner, P. Stoller, and V. Sandoghdar. Detection and spectroscopy of gold nanoparticle using supercontinuum white light confocal microscopy. *Physical Review Letters*, 93:037401–1, 2004.

[142] H.A. Haus. *Electromagnetic Noise and Quantum Optical Measurements*. Springer-Verlag, 2000.

[143] H.P. Yuen and V.W.S. Chan. Noise in homodyne and heterodyne detection. *Optics Letters*, 8:177–, 1983.

[144] P. Stoller, V. Jacobsen, and V. Sandoghdar. Measurement of the complex dielectric constant of a single gold nanoparticle. *Optics Letters*, 31:2474, 2006.

[145] M.A. van Dijk, M. Lippitz, D. Stolwijk, and M. Orrit. A common-path interferometer for time-resolved and shot-noise-limited detection of single nanoparticles. *Optics Express*, 15:2273–2287, 2007.

[146] T. Plakhotnik. Absorption and coherent emission of single molecules. *Journal of Luminescence*, 98:57–62, 2002.

[147] F.V. Ignatovich and L. Novotny. Real-time and background-free detection of nanoscale particles. *Physical Review Letters*, 96:013901, 2006.

[148] T. Plakhotnik. Seeing small. *Journal of Luminescence*, pages 1–17, 2007.

[149] W.E. Moerner. Fundamentals of single-molecule spectroscopy in solids. *Journal of Luminescence*, 60–61:997–1002, 1994.

[150] T. Plakhotnik and D. Walser. Time resolved single molecule spectroscopy. *Physical Review Letters*, 80:4064–4067, 1998.

[151] M. Lippitz, M.A. van Dijk, and M. Orrit. Third-harmonic generation from single gold nanoparticles. *Nano Letters*, 5:799–802, 2005.

[152] J.Y.P. Butter, B. Hecht, B.R. Crenshaw, and C. Weder. Absorption and fluorescence of single molecules. *Journal of Chemical Physics*, 125:154710, 2006.

[153] P. Kukura, M. Celebrano, A. Renn, and V. Sandoghdar. Imaging a single quantum dot when it is dark. *Nano Letters*, ASAP Article, 2008.

[154] B. Lounis and M. Orrit. Single-photon sources. *Reports on Progress in Physics*, 68:1129–1179, 2005.

[155] F.Y. Wu, S. Ezekiel, M. Ducloy, and B.R. Mollow. Observation of amplification in a strongly driven two-level atomic system at optical frequencies. *Physical Review Letters*, 38:1077–1080, 1977.

[156] C. Obermüller and K. Karrai. Far field characterization of diffracting circular apertures. *Applied Physics Letters*, 67:3408, 1995.

[157] C. Obermüller, K. Karrai, G. Kolb, and G. Abstreiter. Transmitted radiation through a subwavelength-sized tapered optical fiber tip. *Ultramicroscopy*, 61:171–177, 1995.

[158] U. Dürig, D.W. Pohl, and F. Rohner. Near-field optical-scanning microscopy. *Journal of Applied Physics*, 59, 1986.

[159] E. Betzig, J.K. Trautman, T.D. Harris, J.S. Weiner, and R.L. Kostelak. Breaking the diffraction barrier: Optical microscopy of a nanometric scale. *Science*, 251:1468–1470, 1991.

[160] R.C. Dunn. Near-field scanning optical microscopy. *Chemical Reviews*, 99:2891–2927, 1999.

[161] B. Hecht, H. Bielefeldt, Y. Inouye, D.W. Pohl, and L. Novotny. Facts and artifacts in near-field optical microscopy. *Journal of Applied Physics*, 81:2492–2498, 1997.

[162] J.A. Veerman, A.M. Otter, L. Kuipers, and N.F. van Hulst. High definition aperture probes for near-field optical microscopy fabricated by focused ion beam milling. *Applied Physics Letters*, 72:3115–3117, 1998.

[163] A.A. Mikhailovsky, M.A. Petruska, M.I. Stockman, and V.I. Klimov. Broadband near-field interference spectroscopy of metal nanoparticles using a femtosecond white-light continuum. *Optics Letters*, 28:1686, 2003.

[164] R.J. Pfab, J. Zimmermann, C. Hettich, I. Gerhardt, A. Renn, and V. Sandoghdar. Aligned terrylene molecules in a spin-coated ultrathin crystalline film of *p*-terphenyl. *Chemical Physics Letters*, 387:490, 2004.

[165] E. Betzig, P.L. Finn, and J.S. Weiner. Combined shear force and near-field scanning optical microscopy. *Applied Physics Letters*, 60:2484–2486, 1992.

[166] K. Karrai and R.D. Grober. Piezo-electric tuning fork tip-sample distance control for near field optical microscopes. *Ultramicroscopy*, 61:197–205, 1995.

[167] W.P. Ambrose, P.M. Goodwin, J.C. Martin, and R.A. Keller. Alterations of single molecule fluorescence lifetimes in near-field optical microscopy. *Science*, 265:364–367, 1994.

[168] R.X. Bian, R.C. Dunn, X.S. Xie, and P.T. Leung. Single molecule emission characteristics in near-field microscopy. *Physical Review Letters*, 75:4772 – 4775, 1995.

[169] B.C. Buchler, T. Kalkbrenner, C. Hettich, and V. Sandoghdar. Measuring the quantum efficiency of single radiating dipoles using a scanning mirror. *Physical Review Letters*, 95:063003, 2005.

[170] S. Kühn, U. Hkanson, L. Rogobete, and V. Sandoghdar. Enhancement of single-molecule fluorescence using a gold nanoparticle as an optical nanoantenna. *Physical Review Letters*, 97:017402, 2006.

[171] A.D. Boozer, A. Boca, R. Miller, T.E. Northup, and H.J. Kimble. Reversible state transfer between light and a single trapped atom. *Physical Review Letters*, 98:193601, 2007.

[172] D. Englund, A. Faraon, B. Zhang, Y. Yamamoto, and J. Vuckovic. Generation and transfer of single photons on a photonic chip. *Optics Express*, 15:5550–5558, 2007.

[173] G.T. Foster, L.A. Orozco, H.M. Castro-Beltran, and H.J. Carmichael. Quantum state reduction and conditional time evolution of wave-particle correlations in cavity qed. *Physical Review Letters*, 85:3149–3152, 2000.

[174] C. Hettich, C. Schmitt, J. Zitzmann, S. Kühn, I. Gerhardt, and V. Sandoghdar. Nanometer resolution and coherent optical dipole coupling of two individual molecules. *Science*, 298:385, 2002.

[175] U. Eichmann, J.C. Bergquist, J.J. Bollinger, J.M. Gilligan, W.M. Itano, D.J. Wineland, and M.G. Raizen. Young's interference experiment with light scattered from two atoms. *Physical Review Letters*, 70:2359–2362, 1993.

[176] M. Hennrich, A. Kuhn, and G. Rempe. Transition from antibunching to bunching in cavity qed. *Physical Review Letters*, 94:053604, 2005.

[177] P. Domokos, P. Horak, and H. Ritsch. Quantum description of light-pulse scattering on a single atom in waveguides. *Physical Review A*, 65:033832, 2002.

[178] K. Resch, J.S. Lundeen, and A.M. Steinberg. Conditional-phase switch at the single-photon level. *Physical Review Letters*, 89:037904, 2002.

[179] R.M. Macfarlane and R.M. Shelby. *Spectroscopy of solids containing rare earth ions*, volume 21 of *Modern Problems in condensed matter sciences*, chapter 3, pages 51–184. North Holland, 1987.

[180] B.E. Bowlby and B. Di Bartolo. Applications of the Judd-Ofelt theory to the praseodymium ion in laser solids. *Journal of Luminescence*, 100:131–139, 2002.

[181] C.W. Gardiner. Driving a quantum system with the output field from another driven quantum system. *Physical Review Letters*, 70:2269–2272, 1993.

[182] P. Kochan and H.J. Carmichael. Photon-statistics dependence of single-atom absorption. *Physical Review A*, 50:1700 – 1709, 1994.

[183] P. Andrew and W.L. Barnes. Energy transfer across a metal film mediated by surface plasmon polaritons. *Science*, 306:1002–1005, 2004.

[184] S. Götzinger, L.S. Menezes, A. Mazzei, S. Kühn, V. Sandoghdar, and O. Benson. Controlled photon transfer between two individual nanoemitters via shared high-q modes of a microsphere resonator. *Nano Letters*, 6:1151–1154, 2006.

List of Figures

Credits

Ich möchte Vahid danken, dass er mir die Chance gegeben hat, in einer grossartigen Arbeitsgruppe an einem aktuellen und herausfordernden Projekt arbeiten zu können. Seine Ideen haben mich immer begeistert und seine Motivationskünste dazu geführt, dass ich niemals den Spass oder das Ziel vor Augen verloren habe.

Ich hatte das grosse Glück, mit dem "Tausendsassa" Ilja zusammen an diesem Projekt zu arbeiten. Wir waren ein perfektes Team und in zahllosen Nächten, die wir auf das erlösende Muhen des Scanprogrammes gewartet, sind die Diskussionsthemen nie ausgegangen.

Gert war unentbehrlich, um unsere experimentelle Begeisterung in wissenschaftliche Form zu bringen. Ich möchte ihm danken, dass er mit so viel Geduld und Sorgfalt Klarheit in die Datenfluten gebracht hat, und jederzeit zum Gedankenaustausch bereit war.

Mit Jaesuk ist viel Humor in unser Team gekommen. Wir hatten viel Spass beim Experimentieren zu Pimsleurs Sprachkursen und Schlagermusik. Dazu weiss er auf jede Frage das passende Paper hervorzuzaubern. Auch Martin hat das neue Thema mit Begeisterung angepackt. Ich bin gespannt, wie sich die Experimente weiter entwickeln.

Weiterhin möchte ich Alois als stete Quelle nützlicher Tips und Apparate, Rob und Pavel für die Unterstützung in den Tagen der Nahfeldexperimente danken. Mario hat mit Simulationen Licht in die Wechselwirkungen zwischen Sample und Spitze gebracht. Mit den Kollegen Andi, Lobert, Stephan und Lutz habe ich im Labor leider zu wenig Zeit, ausserhalb aber umso mehr verbracht. Alle Mitglieder der Nano-Optik Gruppe haben meine Zeit an der ETH positiv geprägt. Ich habe mich dort immer wohl gefühlt und werde die kollegiale Atmosphäre vermissen.

Ich danke Bruno und Peter für den mechanischen und elektronischen Support am Anfang der Zeit, und David und Markus gegen Ende, v.a. für das Verständnis, dass wir unseren Bedarf an Spezialanfertigungen nie früher erahnen konnten.

Auch meinen Freunden und Mitbewohnern, die das Leben ausserhalb des Labors mit zahlreichen Essen, Feiern und Projekten bereichert haben.

Pam für ihren Rückhalt, während sie ihre eigene Arbeit geschrieben hat.

Und ich danke meinen Eltern und meiner Schwester für ihre Unterstützung über all die Jahre.

Curriculum Vitae

Gert C. Wrigge

Date of birth: 24. May 1974
Place of birth: Stade, Germany
Citizenship: German

Rötelstrasse 63
8037 Zürich
Switzerland

phone: +41 44 633 4964
fax: +41 44 633 1316
wrigge@phys.ethz.ch

Education and Degrees

06/2003–03/2008	ETH Zürich, Switzerland *PhD Research in Nano Optics*
01/2002–05/2003	ETH Zürich, Switzerland *Research assistant*
10/1998–04/2001 March 2001	University of Freiburg, Germany *Diplom*
08/1997–09/1998 June 1998	Wayne State University, Detroit, USA *Master of Arts in physics*
10/1994–06/1997 October 1996	University of Freiburg, Germany *Vordiplom*

Awards

T.Rumble Graduate Fellowship
Wayne State University, Detroit, USA

Publications related to PhD work

- I. Gerhardt, G. Wrigge, G. Zumofen, J. Hwang, A. Renn, V. Sandoghdar, *Coherent State Preparation and Observation of Rabi Oscillations in a Single Molecule*, submitted
- G. Wrigge, J. Hwang, I. Gerhardt, G. Zumofen, V. Sandoghdar, *Exploring the limits of single emitter detection in fluorescence and extinction*, submitted
- G. Wrigge, I. Gerhardt, J. Hwang, G. Zumofen, V. Sandoghdar, *Efficient coupling of photons to a single molecule and the observation of its resonance fluorescence*, Nature Physics **4** (2008), 60
- I. Gerhardt, G. Wrigge, M. Agio, P. Bushev, G. Zumofen, V. Sandoghdar, *Scanning near-field optical coherent spectroscopy of single molecules at 1.4 K*, Opt. Lett. **32** (2007), 1420
- I. Gerhardt, G. Wrigge, P. Bushev, G. Zumofen, M. Agio, R. Pfab, V. Sandoghdar, *Strong extinction of a laser beam by a single molecule*, Phys. Rev. Lett. **98** (2007), 033601
- V. Sandoghdar, E. Klotzsch, V. Jacobsen, A. Renn, U. Hakanson, M. Agio, I. Gerhardt, J. Seelig, G. Wrigge, *Optical Detection of Very Small Nonfluorescent Nanoparticles*, Chimia **60** (2006), 761

Presentations related to PhD work

- *Ultrasensitive coherent detection of single quantum emitters*, Kolloquium Physikalische Chemie, ETH Zürich 2007
- *Strong light extinction by a single molecule*, talk, CLEO/QELS, Baltimore 2007
- *Strong light extinction by a single molecule*, talk, DPG Tagung, Düsseldorf 2007
- *Strong light extinction by a single molecule*, invited talk, NanoMeta Conference, Seefeld 2007
- *Near-field imaging of single molecule scattering at T=1.4K*, talk, NFO-9, Lausanne 2006
- *Scattering and Absorption of light by a single emitter under a subwavelength aperture*, poster, HBSM, Aussois 2006
- *Scattering and Absorption of light by a single emitter under a subwavelength aperture*, poster, 357. Heraeus Seminar, Bad Honnef 2005